MAGNETISM IN CRYSTALLINE RARE-EARTH COMPOUNDS

by

R. D. Johnson

Submitted in conformity with the requirements
for the degree of Ph. D.
Department of Physics
Durham University

Contents

Declaration

The material contained within this thesis has not previously been submitted for a degree at the University of Durham or any other university. The research reported within this thesis has been conducted by the author unless indicated otherwise.

Copyright Notice

List of Publications

1. *Determination of magnetic order of the rare-earth ions in multiferroic $TbMn_2O_5$.*
   R. D. Johnson, S. R. Bland, C. Mazzoli, T. A. W. Beale, C-H. Du, C. Detlefs, S. B. Wilkins and P. D. Hatton.
   Phys. Rev. B **78** 104407 (2008)

2. *Probing ion-specific magnetism in multiferroics.*
   R. D. Johnson, S. R. Bland, C. Mazzoli, T. A. W. Beale, C-H. Du, C. Detlefs, S. B. Wilkins and P. D. Hatton.
   ESRF Highlights 86 (2008)

3. *Magnetic structure determination using polarised resonant x-ray scattering.*
   P. D. Hatton, R. D. Johnson, S. R. Bland, C. Mazzoli, T. A. W. Beale, C-H. Du, C. Detlefs and S. B. Wilkins.
   Journal of Magnetism and Magnetic Materials **321** 810 (2009)

4. *Determining crystal field distortions of YVO_3 through x-ray scattering.*
   T. A. W. Beale, R. D. Johnson, S. R. Bland, P. D. Hatton, L. Bouchenoire, D. Prabhakaran and A. T. Boothroyd.
   Solid State Phenomena **152** 147 (2009)

5. *Thermally induced rotation of $3d$ orbital stripes in $Pr(Sr_{0.1}Ca_{0.9})_2Mn_2O_7$.*
   T. A. W. Beale, S. R. Bland, R. D. Johnson, P. D. Hatton, J. C. Cezar, S. S. Dhesi, M. v. Zimmermann, D. Prabhakaran and A. T. Boothroyd.
   Phys. Rev. B **79** 054433 (2009)

6. *Observed and calculated energy spectra of Bragg-forbidden reflections in YVO_3.*
   R. D. Johnson, T. A. W. Beale, Y. Joly, S. R. Bland, P. D. Hatton, C. Mazzoli, L. Bouchenoire, D. Prabhakaran and A. T. Boothroyd.
   J. Phys.: Conf. Ser. **200** 012073 (2010)

7. *Soft x-ray diffraction from lattice constrained orbital order in $Pr(Sr_{0.1}Ca_{0.9})_2Mn_2O_7$.*
   T. A. W. Beale, S. R. Bland, R. D. Johnson, P. D. Hatton, J. C. Cezar, S. S. Dhesi, D. Prabhakaran and A. T. Boothroyd.
   J. Phys.: Conf. Ser. **211** 012007 (2010)

8. *Resonant x-ray scattering from the $4p$ quadrupole moment in YVO_3*
   T.A.W. Beale, R.D. Johnson, Y. Joly, S.R. Bland, P.D. Hatton, L. Bouchenoire, C. Mazzoli, D. Prabhakaran and A.T. Boothroyd
   Phys. Rev. B **82**, 024105 (2010)

9. *Antiferromagnetically spin polarized oxygen observed in magneto-electric $TbMn_2O_5$*
   T. A. W. Beale, S .B. Wilkins, R. D. Johnson, S. R. Bland, Y. Joly, T. R. Forrest, D. F. McMorrow, F. Yakhou, D. Prabhakaran, A.T. Boothroyd, and P.D. Hatton
   Phys. Rev. Lett. **105**, 087203 (2010)

10. *Magnetic structures of the anisotropic intermetallic compounds Er_2CoGa_8 and Tm_2CoGa_8.*
    R. D. Johnson, T. Frawley, P. Manuel, D. Khalyavin, C. Adriano, C. Giles, P. G. Pagliuso, L. C. Chapon and P. D. Hatton
    Phys. Rev. B **82**, 104407 (2010)

11. *Symmetry and charge order in Fe_2OBO_3 studied through polarized resonant x-ray diffraction*
    S. R. Bland, M. Angst, S. Adiga, V. Scagnoli, R. D. Johnson, J. Herrero-Martín and P. D. Hatton.
    Phys. Rev. B **82**, 115110 (2010)

12. *Magnetically induced electric polarization reversal in multiferroic TbMn2O5: Terbium spin reorientation studied by resonant x-ray diffraction*
    R. D. Johnson, C. Mazzoli, S. R. Bland, C-H. Du and P. D. Hatton
    (accepted PRB)

13. *An x-ray diffraction study of the temperature-induced structural phase transitions in $SmVO_3$*
    R. D. Johnson, I. R. Evans, S. R. Bland, D. G. Free, T. A. W. Beale, P. D. Hatton, L. Bouchenoire, D. Prabhakaran and A. T. Boothroyd
    (submitted to Phys. Rev. B)

14. *Direct evidence of coupling between magneto-striction and electric polarization in multiferroic $TmMn_2O_5$*
    R. D. Johnson, P. Thompson, S. R. Bland, L. Bouchenoire, H. Kimura, Y. Noda and P. D. Hatton
    (submitted to Phys. Rev. Lett.)

Abstract

Magnetism in crystalline rare-earth compounds

R. D. Johnson

In this thesis we investigate the magnetism of a selection of crystalline materials that display fascinating macroscopic properties, largely due to the complex behaviour of rare-earth ions. The technique of choice is diffraction; shown to provide the most lucid of results in this field of research. Neutron powder diffraction, a well established tool for determining magnetic structures, has been employed in order to determine two magnetic structures of the intermetallic R_2CoGa_8 series. This was the first such study of these materials, which are of great interest as the magnetic exchange interactions of the rare-earth ions compete with the crystal electric field, giving rise to a wealth of magnetic properties tuneable by the choice of rare-earth ion. We then move on to study two of the most extreme multiferroic materials, $TbMn_2O_5$ and $TmMn_2O_5$. We have developed a new technique for determining electronic state specific magnetic structures through resonant x-ray diffraction, which we have successfully employed in an investigation of the terbium magnetic sub-lattice in $TbMn_2O_5$. The outstanding question in many multiferroics regards the exact microscopic mechanisms at play. Due to the huge potential in technology, this has been the subject of intense debate over that past decade. We have shown, through *ab-initio* computation and the simultaneous measurement of electric polarisation and magneto-striction, that the exchange-striction model is dominant in the main ferroelectric phase of $TbMn_2O_5$ and $TmMn_2O_5$. Through ion specific resonant x-ray diffraction measurements, we have clarified the behaviour of the terbium sublattice upon the magnetic field induced electric polarisation reversal in $TbMn_2O_5$. Furthermore, we have made the discovery of additional incommensurate magnetic diffraction signals, believed to be indicative of the response of magnetic domains to applied magnetic fields.

Acknowledgements

The contents of this thesis represents several years work that has stemmed from collaboration with institutions and facilities across the world. It has only been possible through the support of many people whom I individually thank here. In case I have missed anyone, I am very sorry.

First I thank my research group at Durham University. My supervisor, Prof. Peter Hatton, has provided continual advice throughout my Ph. D. His trusting guidance and steadfast support has allowed me to successfully pursue the areas of research that interest me the most, and I thank him greatly for this. Dr. Stewart Bland has been my fellow Ph. D. student, and has provided endless experimental support, advice, and wisdom. So too has Dr. Thomas Beale, from whom I have learnt the most about the resonant x-ray diffraction experimental technique.

Also at Durham University, I wish to thank John Dobson, our group technician, Dr. Ian Terry for the use of the MPMS magnetometer, and Prof. Damian Hampshire and Mark Raine for the use of the PPMS. David Pattinson has kindly helped precisely cut a number of single crystal samples, and Rob Treharne evaporated the gold for use as electrical contacts in the sample preparation in Chapter 5. A crystallographic study of vanadium oxides not presented within this thesis was performed in collaboration with Dr. Ivana Evans and David Free, of the Department of Chemistry, and I thank them for all their advice and experimental assistance.

The majority of the data presented in this thesis was measured at the European Synchrotron Radiation Facility (ESRF), Grenoble, France, on beam lines ID20 and BM28 (XMaS). I have worked closely with Dr. Claudio Mazzoli, the ID20 beam line scientist, on the study presented in Chapters 3 and 6. His help and advice on experiment has been exceptional. Furthermore, he has provided invaluable assistance in the subsequent data analysis. I also thank Dr. Javier Herrero-Martin and Dr. Valerio Scagnoli, also staff at ID20. The experiment presented in Chapter 5

was conducted on BM28, and I thank the beam line staff, namely Dr. Laurence Bouchenoire, Dr. Peter Normile, Dr. Simon Brown, Dr. Oier Bikondoa, and Paul Thompson, for their support. In particular I thank Paul, for the development of the *in-situ* electric field measurements. Dr. Carston Detlefs, also at the ESRF, has offered enlightening discussions throughout my Ph. D.

The neutron powder diffraction data presented in Chapter 2 was measured on the WISH instrument at ISIS, the UK neutron spallation source. I thank the WISH instrument staff, Dr. Pascal Manuel, Dr. Dmitry Khalyavin and Dr. Laurent Chapon for experimental support and advice throughout the data analysis. I also thank Laurent for invaluable discussions regarding the multiferroic $R\mathrm{Mn_2O_5}$ series.

The calculations in Chapter 4 were performed using the FDMNES code authored by Dr. Yves Joly of the Centre National de la Recherche Scientifique, France. I am extremely grateful for the kind support he has offered me, without which the calculations would not have been successful. I also thank Dr. Stuart Wilkins of the Brookhaven National Laboratory, USA, who has given me advice throughout the analysis presented in Chapter 3 and 4. Also, I have learnt from Stuart some of the more intricate details of resonant x-ray diffraction

For the provision of extremely high quality samples I thank Dr. Carlos Giles and Cris Adriano of the Universidade Estadual de Campinas, Sao Paulo, Brazil ($R_2\mathrm{CoGa_8}$), Dr. Chao-Hung Du, of Tamkang University, Taiwan ($\mathrm{TbMn_2O_5}$), and Dr. Hirouki Kimura and Prof. Yukio Noda of the Institute of Multidisciplinary Research for Advanced Materials, Tohoku University, Japan ($\mathrm{TmMn_2O_5}$).

Finally, I thank Prof. Andrew Boothroyd and Dr. D. Prabhakaran from the University of Oxford, and Prof. Steve Collins and Dr. Alessandro Bombardi of the DIAMOND light source, UK, for their part in collaborative work not included in this thesis.

To my parents, Peter and Jean, for their tireless support of my education.

Chapter 1

Introduction

1.1 Outline

Many physical properties of solid-state compounds originate in long-range electronic orders. Such materials are termed strongly correlated electron systems, in which the electrons of the periodic array of ions order according to exchange interactions [1, 2]. Through the study of such materials, experimental evidence from bulk magnetisation and transport measurements and electron, x-ray or neutron diffraction has often given rise to new physical interpretations of the quantum electronic behaviour in the solid state. Furthermore, many routes to new science and technology have become available through this field of research [3–5].

A classic example of long-range electronic order is the charge order present within $La_{2-x}Sr_xNiO_4$, where $x \simeq \frac{1}{3}$ [6, 7]. Charge order is the periodic modulation of charge away from the expected average valency of a given ion species that are located at crystallographically equivalent positions. At low temperatures NiO_2 layers form a quasi-2D charge stripe state that is commensurate with the lattice. The stripe order is strongly dependent upon the hole concentration, and hence the stripe carrier density. Upon warming the stripe state melts and a 'stripe glass'

forms consisting of short-range charge correlations. On further heating the charge becomes disordered. The closely related material $La_{0.5}Sr_{1.5}MnO_4$ is an example of a compound that exhibits orbital order [8–10], *i.e.* unlike $La_{2-x}Sr_xNiO_4$, the charge order within the sample is accompanied by a long-range, preferential occupation of particular electron orbitals. In $La_{0.5}Sr_{1.5}MnO_4$ the manganese ions are coordinated within oxygen octahedra. Upon cooling below 240 K, the charge and orbital order occur simultaneously. The manganese ions adopt either 3+ or 4+ valency and arrange in a checkerboard pattern in the *ab*-plane (charge order). A large cooperative Jahn-Teller effect (a distortion that lowers the electrostatic potential energy) was evident in the $Mn^{3+}O_6$ octahedra. This gave rise to unequal Mn-O bond lengths and hence the preferential occupation of the $d_{x^2-z^2}$ and $d_{y^2-z^2}$ orbitals for the single e_g electron. These orbitals were found to be occupied in alternate stripes across the *ab*-plane (orbital order) [8–10].

In this thesis we focus on studying magnetic long-range correlations in a selection of novel crystalline materials. Magnetic order within strongly correlated electron systems is often found to be far more complex that the classic textbook description of ferromagnetism, ferrimagnetism or antiferromagnetism. Magnetic order can be found to be commensurate or incommensurate with the lattice. In the incommensurate case it is often convenient to think of the magnetic order as a spin density wave (SDW) propagating through the crystal [11]. A SDW occurs where all the moments point in the same direction, but the magnitudes of the local moments vary with a sinusoidal periodicity through the crystal. Even in apparently simple collinear antiferromagnets, the competition of magnetic exchange interactions in all three dimensions can result in a number of different orders, often labelled A-type, C-type, G-type *etc.* [12], depicted in figure 1.1. Furthermore, 3D systems can adopt quasi-2D or -1D magnetic structures [13, 14]. Some magnetic systems are even more complex due to the coexistence of a number of different magnetic sub-

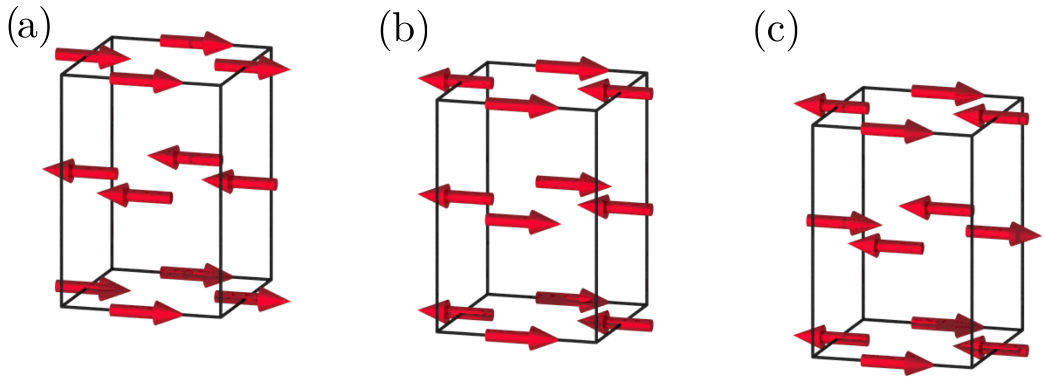

Figure 1.1: (a) A-type, (b) C-type, and (c) G-type examples of collinear antiferromagnetic structures.

lattices, often assigned to different ionic species within compounds of more than one magnetic element [15, 16].

An archetypal material with a complex long-range antiferromagnetic order is holmium. Rare-earth magnetism is particularly interesting, owing in part to the localised nature of the $4f$ electrons and the often strong interaction with the crystal electric field that lifts the energetic degeneracy of the ground state J multiplet (the good quantum number used to describe the rare-earth ion) [17]. Single crystal neutron diffraction experiments [18] showed that below the Néel temperature (at 133 K) the holmium spins adopt a helical structure, shown in figure 1.2(a), that propagates along the *c*-axis. The holmium moments lie in the *ab*-plane with a rotation of approximately 50° every stacking layer. On further cooling a conical structure develops, shown in figure 1.2(b), where a net moment along the *c*-axis develops. At 4.2 K, the conical structure becomes a distorted helical one where the moments favourably align along the easy *b*-axis. Also, the rotation per layer has reduced to 30°. Importantly, the first resonant enhancement of a magnetic x-ray diffraction signal at an absorption edge was observed in holmium in 1988 [19]. Magnetic resonant x-ray diffraction has developed dramatically since this discovery, giving rise to the

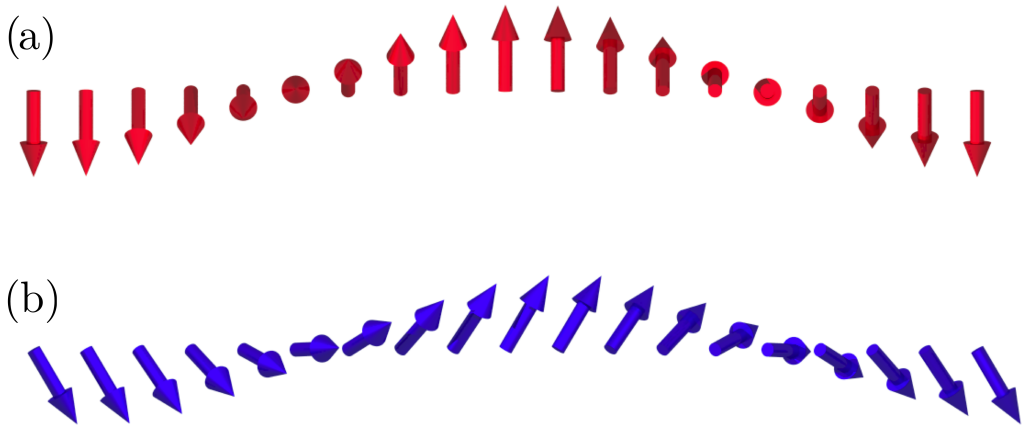

Figure 1.2: (a) A helical antiferromagnetic structure where the spins rotate in a plane perpendicular to the propagation vector. (b) A conical antiferromagnetic structure, which is similar to the helical structure in (a) but also involves a canting, and hence a net moment, in the direction of propagation.

cutting edge theoretical and experimental techniques employed within this thesis.

Diffraction experiments provide some of the most lucid results in the study of strongly correlated magnetic structures and as such form the basis of all the experimental work presented in the following chapters. Both neutron and x-ray diffraction techniques have advantages and disadvantages when investigating crystal structures and magnetism. X-rays interact solely with the electron density and so the scattering amplitude is strongly dependent upon the number of electrons, Z. As such, the properties of light elements such as hydrogen, carbon and oxygen are often not easily quantified by x-ray scattering techniques, particularly when in the presence of heavier elements. The same is true of the neutron magnetic scattering amplitude, which also involves a coupling with the ionic electron density. On the other hand, x-rays are ideal in the study of the heavy rare-earth elements with large Z and often large magnetic moments. The neutron nuclear scattering factor, however, is independent of Z; following no particular trend across the elements. Neutron scattering

is therefore ideally suited to crystallographic studies of, for example, hydrocarbons. A further issue with the Z dependence of the x-ray and neutron magnetic scattering amplitudes is that the diffraction intensity suffers from a form factor decrease at high $\mathbf{Q}$, whereas neutron diffraction from nuclei does not.

There are some materials that are not suited to neutron diffraction experiments; those with elements of high neutron absorption or incoherent scattering, for example samarium, cadmium and gadolinium. The incoherent scattering is a phenomena unique to neutrons that occurs due to fluctuations in the sample. There are two types. First, isotopic incoherent scattering occurs when there is a random distribution of isotopes in the sample. Second, spin incoherence occurs due to the possibility of two spin states of the neutron-nucleus system; $I + \frac{1}{2}$ and I - $\frac{1}{2}$, where I is the nucleus spin. In diffraction experiments we only usefully measure the coherent scattering. The incoherent scattering appears in the diffraction pattern as background.

Compared to the resonant x-ray cross section (section 1.3.3), the magnetic interaction between the neutron and electron spins is very strong. This often makes neutron diffraction the tool of choice for investigating magnetic structures. However, synchrotron x-ray sources have a flux many orders of magnitude greater than that of neutron sources. Also, the interaction of the neutron with matter is weak, and so many don't scatter at all. This imposes often unachievable constraints on the minimum sample size. To gain sufficient diffracted intensity, single crystal neutron diffraction experiments require samples with dimensions of at least several millimetres. Synchrotron x-ray beams may be as small as 20 μm $\times$ 20 μm yet still maintain enormous flux; the sample then does not need to be much larger. This often makes x-ray scattering experiments favourable. Furthermore, in complex systems with a number of magnetic sub-lattices, the elemental specificity of resonant x-ray diffraction, described in section 1.3.3, can prove to be extremely advantageous.

In Chapter 2 we present a study of two ternary intermetallic compounds, Er_2CoGa_8

and Tm_2CoGa_8, two members of the newly synthesised, iso-structural R_2CoGa_8 (R = rare earth ion) series [20, 21]. As described later in greater detail, intermetallic compounds exhibit a number of microscopic electronic properties that compete, resulting in a diverse range of macroscopic phenomena. In the highly anisotropic R_2CoGa_8 series the magnetic behaviour is strongly influenced by the competition of the RKKY exchange interaction with the crystal electric field [22]. To better understand the electronic properties of this series, we have solved the magnetic structures of Er_2CoGa_8 and Tm_2CoGa_8; the only members of the series with magnetic easy-axis in the *ab*-plane [20]. The technique of choice was neutron powder diffraction. Although the cobalt ions have a relatively large incoherent cross section and absorption coefficient, the rare-earth magnetic moments were predicted to be large, potentially giving rise to strong magnetic reflections. Also, suitably large powder samples were available. The neutron powder diffraction technique and associated computational software is well established in the solution of magnetic structures.

We then present a thorough magnetic resonant x-ray diffraction study of the microscopic magnetic properties of two magneto-electric, multiferroic compounds, $TbMn_2O_5$ and $TmMn_2O_5$; members of the RMn_2O_5 series [23]. Resonant x-ray diffraction is ideally suited to such studies as the magnetic structures are extremely complex. Element specificity makes it possible to disentangle the coexisting magnetic sub-lattices, the interactions of which lead to the macroscopic properties observed. Magneto-electric multiferroic materials are those in which long-range magnetic and electric degrees of freedom are closely coupled. The exact microscopic mechanisms underlying the observed phenomena are to date uncertain, and so studies of these materials have formed the basis of a timely and exciting area of solid-state research. Furthermore, multiferroic materials show great potential as key components in future technologies, for example in the development of magneto-electric sensors, or in novel data storage media that could incorporate both magnetically and

electrically stored bits. This topic is discussed in detail in section 3.1. In Chapter 3 we present the development of a new methodology for determining ion-specific magnetic moment directions through magnetic resonant x-ray scattering, using the rare-earth ions in $TbMn_2O_5$ as an example. The magneto-electric coupling in both compounds was then investigated: in Chapter 4 *ab-initio* calculations of magnetic resonant x-ray diffraction data at the oxygen *K*-edge of $TbMn_2O_5$ reveal the nature of antiferromagnetic oxygen spin polarisation, and in Chapter 5, we provide direct evidence of the exchange-striction mechanism of magneto-electric coupling in $TmMn_2O_5$; as predicted in the commensurate phases of the RMn_2O_5 series. Finally the magnetic response of $TbMn_2O_5$ to high applied magnetic fields has been investigated, presented in Chapter 6.

In the following sections of this introductory chapter we first discuss magnetic exchange interactions. The competition of these interactions results in the long-range, strongly correlated magnetic structures studied within this thesis, and as such are key to interpreting the respective physical properties. We then outline the theory of diffraction, and present the equations that describe the scattering processes of both neutrons and x-rays from crystal and magnetic structures. This forms the basis for the data analysis and interpretation presented throughout the following experimental chapters. Finally in this chapter we outline two computational techniques, the Rietveld refinement of neutron powder diffraction patterns by the FULLPROF package [24], and the simulation and fitting of resonant x-ray diffraction energy spectra by FDMNES [25].

1.2 Magnetic exchange in crystalline materials

Magnetic ions within crystalline materials communicate and align via exchange interactions. These are primarily direct exchange [26], super exchange [1, 27], double exchange [28, 29], Ruderman-Kittel-Kasuya-Yosida (RKKY) exchange [30–32]

and antisymmetric Dzyaloshinsky-Moriya (DM) exchange [33–35]. Magnetic exchange is simply a quantum mechanical electrostatic interaction. For a given system of electrons it is necessary that the total wave-function is antisymmetric. Considering a pair of electrons, this constrains the system to two possible states. One with a symmetric spatial state and an antisymmetric singlet spin state ($S = 0$), and another with an antisymmetric spatial state and a symmetric triplet spin state ($S = 1$). The energetic difference between singlet and triplet states can be parameterised by $\mathbf{S_1} \cdot \mathbf{S_2}$, giving rise to the Heisenberg model with the Hamiltonian given by

$$\mathcal{H}_{exch} = -\sum_{ij} \mathcal{J}_{ij} \mathbf{S_i} \cdot \mathbf{S_j} \tag{1.1}$$

where $\mathcal{J}_{ij}$ is the exchange constant (or exchange integral). For $\mathcal{J} > 0$ the triplet $S = 1$ state is favoured, whereas for $\mathcal{J} < 0$ the singlet $S = 0$ is favoured [36, 37].

This has interesting consequences in crystalline materials. The covalency between nearest neighbour magnetic ions may be mediated through bonding (spatially symmetric) or antibonding (spatially antisymmetric). The bonding orbital has lower kinetic energy than the antibonding orbital, and so a spatially symmetric, $S = 0$ state is preferred. Such an interaction, known as direct exchange, requires sufficient overlap between electron orbitals. As such it is often insignificant in systems composed of rare-earth or transition metal elements where the respective f and d electron orbitals are local compared to inter-atomic spacings. Magnetic interactions in crystals are usually mediated through indirect exchange as follows.

In ionic materials, super exchange can result in the interaction of two next-nearest-neighbour magnetic ions, mediated by an intermediate non-magnetic ion. This is often the case in transition metal oxides with transition metal - oxygen - transition metal (TM-O-TM) coordinations. There is a direct overlap of TM-O orbitals, across which electrons may become delocalised, hence lowering the kinetic energy of the system. The delocalising of electrons can only occur if the TM ions

order antiferromagnetically [37]. This scheme is highly dependent upon the orbital overlap, and as such is dependent upon the TM-O-TM bond angle considering the anisotropy of the TM d and O $2p$ states.

Similar to super exchange, double exchange also occurs via a non-magnetic intermediate ion. In systems where the magnetic ions can adopt mixed valence states, for example Mn^{3+} and Mn^{4+} in $TbMn_2O_5$ [38], there exists an energetically favourable hopping of an e_g electron from Mn^{3+} to Mn^{4+}. It is necessary to maintain a high spin state (and satisfy Hund's rules) of both magnetic ions. Therefore, as no spin-flip occurs upon electron hopping, the magnetic ions must be ferromagnetically ordered to achieve this low energy state.

So far we have only considered indirect exchange in ionic compounds. In metals, magnetic exchange may be mediated by the conduction electrons. A localised moment spin polarises conduction electrons which in turn couple to other localised moments at some distance, r, away. First developed to explain unusual features in nuclear spin resonance data of silver metal due to the coupling of nuclear magnetic moments, this exchange interaction is known as the RKKY interaction, named after its founders Ruderman, Kittel, Kasuya and Yosida [30–32]. The magnetic susceptibility due to the RKKY interaction can be written as [37]:

$$\chi(r) = \frac{2k_{\mathrm{F}}^3 \chi_{\mathrm{P}}}{\pi} F(2k_{\mathrm{F}} r) \tag{1.2}$$

where k_{F} is the fermi wave vector, χ_{P} is the Pauli susceptibility, $r = |\mathbf{r}|$ is the distance from the moment in question, and

$$F(x) = \frac{-x\cos x + \sin x}{x^4} \tag{1.3}$$

As $F(x)$ is an oscillatory function, the RKKY interaction can result in an antiferromagnetic or ferromagnetic interaction that depends upon and diminishes with r.

Finally, we describe the antisymmetric Dzyaloshinsky-Moriya (DM) exchange interaction. Instead of the interaction being mediated by an oxygen ion, as in super and double exchange, the excited state of the DM exchange originates in the spin-orbit coupling. The exchange Hamiltonian is written as

$$\mathcal{H}_{\mathrm{DM}} = \mathbf{D} \cdot \mathbf{S_1} \times \mathbf{S_2} \tag{1.4}$$

where **D** is a polar vector that either points towards the neighbouring spin or perpendicular to it, depending upon the symmetry of the crystal field. Importantly, one requires a lack of inversion symmetry between the two magnetic ions for **D** to be non-zero [37]. This exchange will tend to align neighbouring spins perpendicular to each other in a plane that is perpendicular to **D** such that a negative exchange energy is realised. This often results in the canting of antiferromagnetic structures, and is of particular importance in the *R*MnO_3 series discussed later in this thesis, in which the DM interaction is believed to be crucial to the microscopic mechanism of the magneto-electric coupling [39, 40].

1.3 Diffraction

As explained in section 1.1, diffraction techniques may be employed to investigate the microscopic electronic behaviour of strongly correlated electron systems. In this section we describe, in general, diffraction from a periodic array of scattering centres (atoms). We then explain the scattering processes involved, and hence derive the scattering amplitudes and differential cross sections for the interaction of both neutrons and x-rays with atoms. Specifically, in this thesis we interpret the results of both neutron and x-ray diffraction from magnetic structures in order to obtain information regarding the magnetic behaviour of the system. The relatively simple case of neutron magnetic scattering is described in the following section.

The complex case of magnetic resonant x-ray diffraction is described in detail in section 1.3.3. For clarity, in the following we describe diffraction from a crystal in the context of x-rays, however all formula presented below are equally valid for neutron diffraction.

The atomic positions within a crystal are described by the sum of two vectors; $\mathbf{R_n} + \mathbf{r}_j$. $\mathbf{R_n}$ are the lattice vectors that describe the periodic repeat of the unit cell in the crystal lattice, and $\mathbf{r}_j$ are the unit cell vectors that describe the position of atoms within the unit cell (the basis). As x-rays do not necessarily scatter in the same direction as the incident beam, we define an associated momentum transfer, written as:

$$\hbar\mathbf{Q} = \hbar\mathbf{k} - \hbar\mathbf{k}' \tag{1.5}$$

where **k** and **k'** are the incident and scattered wavevectors, respectively, and **Q** is the scattering vector. As shown later in this section, **Q** is used universally to describe any given scattering process. The condition for scattered x-rays to add in phase, and hence result in a diffraction maxima, is dependent only upon the repeat of the crystal lattice (the atomic basis determines the relative intensities of the diffraction peaks) and may be written as

$$\mathbf{Q} \cdot \mathbf{R_n} = 2\pi \times \text{integer} \tag{1.6}$$

In general $\mathbf{R_n} = n_1\mathbf{a}_1 + n_2\mathbf{a}_2 + n_3\mathbf{a}_3$, where n_1, n_2 and n_3 are integers and $\mathbf{a}_1$, $\mathbf{a}_2$ and $\mathbf{a}_3$ are basis vectors of the lattice. A unique solution to equation 1.6 can be found by considering the reciprocal lattice. The reciprocal space vector related to $\mathbf{R_n}$ may be written as

$$\mathbf{G} = h\mathbf{a}_1^* + k\mathbf{a}_2^* + l\mathbf{a}_3^* \tag{1.7}$$

where *h, k* and *l* are integers commonly known as Miller indices, and

$$\mathbf{a}_1^* = 2\pi \frac{\mathbf{a}_2 \times \mathbf{a}_3}{\mathbf{a}_1 \cdot (\mathbf{a}_2 \times \mathbf{a}_3)},\ \mathbf{a}_2^* = 2\pi \frac{\mathbf{a}_3 \times \mathbf{a}_1}{\mathbf{a}_1 \cdot (\mathbf{a}_2 \times \mathbf{a}_3)},\ \mathbf{a}_3^* = 2\pi \frac{\mathbf{a}_1 \times \mathbf{a}_2}{\mathbf{a}_1 \cdot (\mathbf{a}_2 \times \mathbf{a}_3)}$$

The key result is that the product of the reciprocal and real space vectors also satisfies the condition of equation 1.6. Hence, we require:

$$\mathbf{Q} = \mathbf{G} \tag{1.8}$$

i.e. for constructive interference to occur (resulting in a diffraction peak) the scattering vector must coincide with a point in reciprocal space. This is the Laué condition, which is elegantly described by the Ewald sphere construction [41]. This is equivalent to Bragg's law which, derived by considering the scattering from atomic planes within real space, is given by:

$$n\lambda = 2d\sin(\theta) \tag{1.9}$$

where n is an integer, λ is the x-ray wavelength, d is the atomic plane spacing and θ is half the angle between incident and scattered x-rays, labelled 2θ.

To describe the diffraction in total, a structure factor is defined as the product of two factors, one in $\mathbf{R_n}$ (lattice), and the other in $\mathbf{r}_j$ (basis); both incorporating their respective phase factors.

$$F^{cryst}(\mathbf{Q}) = \overbrace{\sum_j f_j \mathrm{e}^{i\mathbf{Q}\cdot\mathbf{r}_j}}^{\text{Unit cell}} \times \overbrace{\sum_n \mathrm{e}^{i\mathbf{Q}\cdot\mathbf{R_n}}}^{\text{Lattice}} \tag{1.10}$$

The scattered intensity is then proportional to $|F^{cryst}|^2$. The first, unit cell term describes systematic absences in the diffraction pattern due to atomic positions, and the lattice term imposes the diffraction condition for the crystal. Indeed, the lattice

term is simply the Laué condition. f_j describes the scattering amplitude of the respective atom, j. For neutrons, this term is the scattering length b, and for x-rays it is the atomic scattering factor $f(\mathbf{Q}, \hbar\omega)$, both of which are defined in sections 1.3.1 and 1.3.2, respectively.

So far we have only considered diffraction from a crystal structure. Through the neutron magnetic scattering factor and the magnetic resonant x-ray scattering amplitude, both described in detail in the following sections, it is possible to measure diffraction peaks that originate in the long-range, periodic magnetic structures outlined in section 1.1. A magnetic structure, whether collinear or cycloidal, has an associated propagation vector, $\mathbf{q_{Mag}}$, equivalent to $\mathbf{Q}$ in section 1.3. The magnetic diffraction peaks are observed as superlattice satellites of the crystallographic Bragg reflections, *i.e.* at positions $\mathbf{Q} = \mathbf{Q_{Bragg}} + \mathbf{q_{Mag}}$. When indexed in the crystal unit cell, $\mathbf{q_{Mag}}$ of a ferromagnetic structure will have integer components (*h, k, l*), resulting in scattered intensity coincident with Bragg positions. A commensurate antiferromagnet will have rational components (*e.g.* $\mathbf{q_{Mag}} = (0.5, 0, 0)$), depending upon the repeat of the magnetic structure with respect to the crystal unit cell. This results in additional magnetic reflections, compared to the structural diffraction pattern. Incommensurate magnetic structures have an irrational period with respect to the crystal cell, and so *h, k,* and *l* are also irrational. One can think of the magnetic structure as forming a superlattice cell comprising of a number of crystal unit cells, in which the relative magnetic reflections would be indexed with integer *h, k,* and *l*, and as such are magnetic Bragg peaks.

1.3.1 Neutron scattering cross section

Neutrons interact with both the nuclei and the unpaired electrons of an atom within a crystal. The interaction between the neutron and nuclei acts via the short range strong force, and is used to solve crystal structures. The neutron scattering from

electrons occurs via a magnetic dipole interaction, and is therefore used to solve magnetic structures. In the following section we give both the nuclear and magnetic scattering amplitudes, and discuss their properties in the context of analysing powder diffraction data.

Neutrons diffract from crystalline materials due to their wavelike behaviour, as given by the de Broglie relationship; $\lambda = h/mv$. Typically, thermal neutrons used in diffraction experiments have energies of approximately 25 meV. This corresponds to a wavelength of 1.8 Å, comparable to the d-spacing of crystalline materials, and similar to that of x-rays.

We only consider the elastic scattering process, relevant in the determination of crystal and magnetic structures as in Chapter 2. In the interaction of the neutron with a nucleus, the atomic scattering length is given as [42]

$$f(\mathbf{Q}) = \frac{m}{2\pi\hbar^2}\int_V V(\mathbf{r})\mathrm{e}^{i\mathbf{Q}\cdot\mathbf{r}}dV \tag{1.11}$$

where $\mathbf{Q}$ is the momentum transfer vector defined in section 1.3, $\mathbf{r}$ is the nucleus radius and m is the neutron mass, and $V(\mathbf{r})$ is the scattering potential of the nucleus. A number of further approximations may be made. It can be assumed that $V(\mathbf{r})$ is zero outside a radius, r_0 and some constant value, a, inside r_o. This allows for a definite integral to be calculated. Also, the neutron wavelength is much larger than the nucleus radius. The scattering can therefore be considered as point like, and $r_0\mathbf{Q} \ll 1$. The atomic scattering length is therefore constant for a given atom and is labelled b:

$$f = \frac{m}{2\pi\hbar^2}a\left(\frac{4}{3}\pi r_0^3\right) = b \tag{1.12}$$

For some elements the neutron scattering length is found to be negative. This simply relates to a π phase shift upon scattering.

Experimentally we must consider the number of scattered neutrons measured

by the detector that has a given solid angle, $\Delta\Omega$. As such we define the differential cross section as the number of neutrons scattered per second into $\Delta\Omega$, divided by the incident beam flux multiplied by $\Delta\Omega$. The nuclear scattering differential cross section, analogous to that defined for x-rays in section 1.3.2, is given as

$$\frac{d\sigma}{d\Omega} = b^2 \tag{1.13}$$

The neutron scattering process measured in powder diffraction structure refinements is described by the elastic coherent differential cross section given as

$$\left(\frac{d\sigma}{d\Omega}\right)_{coh} = N\frac{(2\pi)^3}{v_0}\sum_{\mathbf{G}}\delta(\mathbf{G}-\mathbf{Q})|F_{nuc}(\mathbf{Q})|^2 \tag{1.14}$$

where N is the total number of unit cells and v_0 is the volume of the unit cell. The delta function in equation 1.14 encompasses the Laué condition, as described in section 1.3, where

$$F_{nuc}(\mathbf{Q}) = \sum_j b_j \mathrm{e}^{i\mathbf{Q}\cdot\mathbf{r}_j} \tag{1.15}$$

In time of flight (TOF) neutron diffraction, it is often convenient to consider Bragg's law (equation 1.9), as opposed to the Laué condition. The angle, 2θ, is fixed, and the diffraction peaks are measured as a function of TOF, and therefore wavelength. For greater data collection, and hence improved counting statistics, large detector arrays are employed to measure neutrons scattered over a range of 2θ values, binned to give a histogram as a function of energy. In powder diffraction, the detector arrays measure the Debye-Scherrer cones, which are then integrated and evaluated as a function of energy, giving the TOF powder diffraction patterns as presented in Chapter 2. The TOF peaks have a complex lineshape as a consequence of the formation of the neutron pulse. A rapid build up of neutron flux in the moderator results in a sharp leading edge to the peak profile. By comparison, the

trailing edge has a gradual decay. This lineshape is then convolved with a Gaussian function originating in the instrument resolution. The resolution function is given as

$$\frac{\Delta d}{d} = \left[\left(\frac{\Delta t}{t}^2 \right) + \left(\frac{\Delta L}{L}^2 \right) + (\Delta\theta \cot\theta)^2 \right]^{\frac{1}{2}} \tag{1.16}$$

where d is the sample d-spacing, t is the TOF, L is the flight path from moderator to detector and θ is half the scattering angle. The first and second terms originate in uncertainties in the moderator source and the flight path length. The third term is the angular dispersion that originates in the finite widths of the moderator, sample and detector. This allows a small range of wavelengths to satisfy Bragg's law for a given reflection and is prominent at low angles (large $\cot\theta$).

We now describe the magnetic scattering amplitude. In this thesis we present only the key results for an unpolarised neutron beam, a thorough derivation of the magnetic interaction can be found in references 43 and 44. As described in section 1.3, once the crystal structure is known, the magnetic structure is defined by the propagation vector $\mathbf{q_{Mag}}$, the moment sizes and the moment directions. Magnetic structure solutions by neutron diffraction are possible as the magnetic structure factor is dependent upon all three defining parameters as follows.

In the case of the interaction between neutron and nuclei, it was assumed that the scattering was point like due to the extreme difference in length scales of the neutron wavelength and the nuclei radius. For the magnetic interaction with electrons, a point-like approximation is no longer valid and a $\mathbf{Q}$-dependent atomic form factor must be introduced. This is also the case for x-ray diffraction, as described later (equation 1.23). The magnetic structure factor is then written as

$$F_{mag}(\mathbf{Q}) = \sum_j \mathbf{N}_j p_j \mathrm{e}^{i\mathbf{Q}\cdot\mathbf{r}_j} \tag{1.17}$$

where $\mathbf{N}$ is the magnetic interaction vector defined as

$$\mathbf{N} = \hat{\mu} - (\hat{\mathbf{Q}} \cdot \hat{\mu})\hat{\mathbf{Q}} \tag{1.18}$$

where $\hat{\mu}$ is a unit vector in the direction of the magnetisation, and $\hat{\mathbf{Q}}$ is also a unit vector. Note that the form of the magnetic interaction vector requires a component of the magnetisation to be perpendicular to the scattering vector to get a non-zero scattered intensity. The magnetic scattering length is labelled p and is defined as

$$p = \frac{e^2\gamma}{mc^2} f(\mathbf{Q}) S |\mathbf{N}| \tag{1.19}$$

where γ is the magnetic moment of the neutron in μ_{B}, m is the electron mass, $f(\mathbf{Q})$ is the atomic form factor and S is the magnitude of the spin vector [45]. The nuclear and magnetic form factors contribute to the scattered intensity by adding in quadrature.

1.3.2 X-ray scattering cross section

In the following section we explain the interaction of x-ray radiation with electrons within solids. We mostly follow the theoretical framework of J. Als-Nielson and D. McMorrow [46]. Two assumptions are made. Firstly, we only consider elastic scattering; as was the case for the neutron scattering length. In the classical approach this is justified, but in the complete quantum mechanical description energy may be transferred from the x-ray photon to an electron. However, in this thesis we only measure elastically scattered x-rays. Secondly, when describing the scattering from a bulk single crystal we assume that no multiple scattering events occur; the kinematical approximation. This is a good approximation, as it can be assumed that the scattering is weak. To properly describe the interaction between the x-ray and electron one requires dynamical theory [47] which severely complicates data

analysis.

The classical interpretation of the scattering of an x-ray beam by an electron involves the acceleration of the electron by the incident x-ray's electromagnetic field. In turn, the now oscillating electron acts as a dipole antenna, emitting an x-ray (the scattered beam) with the same wavelength. The effectiveness of this scattering process is described by the Thomson scattering length, which is given as

$$r_0 = \left(\frac{e^2}{4\pi\epsilon_0 m c^2} \right) = 2.82 \times 10^{-5} \text{Å} \tag{1.20}$$

The scattering length r_0 (also known as the classical electron radius) is equivalent to the scattering length in neutron scattering, b, described in section 1.3.1. The differential cross section, analogous to that defined for neutron scattering in section 1.3.1, is defined as

$$\frac{d\sigma}{d\Omega} = r_0^2 P \tag{1.21}$$

where P is a polarisation factor.

Synchrotron radiation is polarised in the plane of the orbit of the stored relativistic electrons, *i.e.* horizontal with respect to the laboratory. This has important consequences for the scattering cross section. When scattering perpendicular to the incident beam polarisation (vertical), the full acceleration of the scattering electron is always observed, and P = 1. When scattering in the plane of the incident beam polarisation (horizontal) there is an angular dependence of the cross section. In the extreme limit, the cross section is zero when scattering at 90° to the incident beam as no component of the scattering electron's acceleration is projected in this direction. In this scenario, $P = \cos^2(2\theta)$, where 2θ is the angle between the detector and the incident x-ray beam. This angular dependence is exploited in the use of polarisation analyser crystals, as described in section 1.3.4.

When scattering from an atom, we must consider a distribution of charge. As

such, a phase difference dependent upon the scattering geometry will occur between x-rays scattered by different volume elements of the charge distribution, separated by a distance, $\mathbf{r}$. This phase difference, when projected onto the incident and scattered wavevectors, is

$$\Delta\phi(\mathbf{r}) = (\mathbf{k} - \mathbf{k}') \cdot \mathbf{r} = \mathbf{Q} \cdot \mathbf{r} \tag{1.22}$$

Any given volume element, $d\mathbf{r}$, will contribute $-r_0\rho(\mathbf{r})d\mathbf{r}$ to the atomic scattering length, where $\rho(\mathbf{r})$ is the electron number density. By multiplying by the phase factor and integrating over the charge distrbution, this gives the total atomic scattering length as

$$-r_0 f^0(\mathbf{Q}) = -r_0 \int \rho(\mathbf{r}) \mathrm{e}^{i\mathbf{Q}\cdot\mathbf{r}} d\mathbf{r} \tag{1.23}$$

where $f^0(\mathbf{Q})$ is the atomic form factor. We note that the atomic scattering length is essentially a Fourier transform of the charge distribution from which the x-rays scatter. At $\mathbf{Q} = 0$, all volume elements scatter in phase, and the atomic form factor is equal to the number of electrons, *Z*. As $\mathbf{Q}$ increases, the phase difference increases, and the atomic form factor diminishes to zero as $\mathbf{Q}$ approaches infinity.

So far we have assumed that the electron is unconstrained. In reality, the electrons are bound to atomic nuclei and constrained to quantised energy levels. This dampens the electronic oscillations and hence reduces the form factor. In general, the form factor should be written as

$$f(\mathbf{Q}, \hbar\omega) = f^0(\mathbf{Q}) + f'(\hbar\omega) + if''(\hbar\omega) \tag{1.24}$$

where $f'(\hbar\omega)$ denotes the reduction of the oscillations and hence the scattering length, and $if''(\hbar\omega)$ describes the phase lag between the driving field and the electron oscillation. This latter term is related to the dissipation of energy in the system and as such is closely coupled to the absorption. The behaviour of the $f'(\hbar\omega)$ and $f''(\hbar\omega)$ terms, known as the anomalous terms, is clearly energy dependent. They

become large at energies relating to the scattering atom's x-ray absorption edges, and result in the atom-specific resonant enhancement exploited in this thesis. The resonant process is described in detail in the following section.

1.3.3 Magnetic resonant x-ray diffraction

In the following section we present the theory that describes the resonant scattering process. We mainly follow the work of Hannon, Trammell, Blume and Gibbs [48] and Hill and McMorrow [49]. However additional information, particularly the treatment of the Hamiltonian, may be found in references 50, 51 and 52.

In the resonant process we gain sensitivity to a specific electronic state of a given ion by exciting an electric multipole transition from a core hole up to an unoccupied orbital; the state in question. This is a virtual transition, resulting in a scattered x-ray with the same energy as that incident; *i.e.* an elastic scattering event. The resonant transitions occur near or at x-ray absorption edges and are labelled accordingly (K, L_{II}, L_{III} etc.). This is illustrated in figure 1.3. We concentrate on two multipole transitions, the electric dipole (E1-E1) and the electric quadrupole (E2-E2). The scattered intensity due to higher order or magnetic transitions is extremely weak by comparison and so can be ignored. Selection rules determine that the E1-E1 transition is only permitted for $\Delta l \pm 1$, and the E2-E2 transititon for $\Delta l = 0$ or ± 2. As such, at the L-edges of rare-earth ions the E1-E1 transition corresponds to an excitation between the core $2p$ to the delocalised, unoccupied $5d$ states, and the E2-E2 transition occurs between the $2p$ and $4f$ states. Despite being known as magnetic resonant x-ray diffraction, the origin of the scattering process is purely electronic. One is in fact sensitive to contrasts in the electronic density of states of the scattering ion sites due to the spin occupation ($4f$) or spin polarisation ($5d$). In contrast to Thomson scattering, described in section 1.3.2, the resonant process has a complex polarisation dependence, shown in the following mathematics. Changes

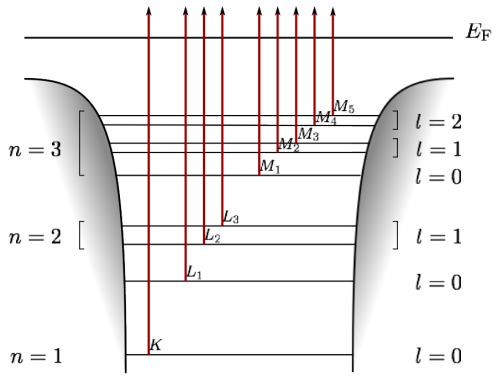

Figure 1.3: Diagram showing the core electron excitations giving rise to x-ray absorption edges, labelled K, L and M, and hence the resonant enhancement of the anomalous terms.

in the x-ray polarisation upon the resonant scattering encodes information about the state of the magnetic ion. This phenomena is exploited in Chapter 3.

As given in section 1.3.2, the atomic form factor is:

$$f(\mathbf{Q}, \hbar\omega) = f^0(\mathbf{Q}) + f'(\hbar\omega) + if''(\hbar\omega) + f^{mag} \tag{1.25}$$

For completeness we include f^{mag}, the non-resonant magnetic scattering term, however it is not significant in the measurements made in this thesis. The resonant scattering process originates in the dispersive and absorptive terms $f'(\hbar\omega) + if''(\hbar\omega)$ which we shall label f^{RXS}. For an electric 2^L-pole resonance, f^{RXS} takes the form

$$f^{RXS} = \frac{4\pi}{|k|} f_D \sum_{M=-L}^{L} \left[\epsilon'^* \cdot \mathbf{Y}^{(e)}_{LM}(\hat{\mathbf{k}}') \mathbf{Y}^{(e)*}_{LM}(\hat{\mathbf{k}}) \cdot \epsilon\right] F^{(e)}_{LM}(\omega) \tag{1.26}$$

where $\mathbf{Y}^{(e)*}_{LM}(\hat{\mathbf{k}})$ are vector spherical harmonics and f_D is the Debye-Waller factor [48]. The strength of the resonance is determined by the transition probability

which, originating in Fermi's Golden Rule, is given by

$$F^{(e)}_{LM}(\omega) = \sum_{\alpha,\eta}\left[\frac{p_\alpha p_\alpha(\eta)\Gamma_x/\Gamma(\eta)}{x(\alpha,\eta)-i}\right] \tag{1.27}$$

where $|\alpha)$ and $|\eta)$ are the initial ground state and the excited state, respectively. p_α is the probability for the various initial states $|\alpha)$ and $p_\alpha(\eta)$ is the probability that the level to which the electron is excited is unoccupied in $|\alpha)$. In the denominator, $x(\alpha,\eta) = [E_\eta - E_\alpha - \hbar\omega]/[\Gamma(\eta)/2]$, which gives the deviation from the resonance in units of the total half width.

$$\Gamma_x = 8\pi e^2|k|\left[\frac{L+1}{L}\right]\left|(\alpha|\sum_i j_L(kr_i)Y_{LM}(\hat{\mathbf{r}}_\mathbf{i})|\eta)\right|^2 \tag{1.28}$$

which when summed over all M gives the partial width for the excited state decay; *i.e.* $|\eta) \rightarrow |\alpha)$. The total width is given by $\Gamma(\eta)$ which takes into account all other de-excitations, such as Auger emission.

The formulation of equation 1.26, and hence also those that follow, is based on the assumption that the system is isotropic where only the electron spin breaks the symmetry. In the case of magnetically frustrated multiferroics, such as $TbMn_2O_5$, this assumption is an over-simplification. However the scattering amplitude in the form presented here has been successfully employed, in particular, to the closely related compound $TbMnO_3$ [53].

The polarisation dependence is determined by the vector spherical harmonics in equation 1.26. These are evaluated for the E1-E1 process and f^{RXS} is rewritten as:

$$f^{RXS}_{E1-E1} = (\epsilon'\cdot\epsilon)F^{(0)}_{E1} - i(\epsilon'\times\epsilon)\cdot\hat{\mathbf{z}}_j F^{(1)}_{E1} + (\epsilon'\cdot\hat{\mathbf{z}}_j)(\epsilon\cdot\hat{\mathbf{z}}_j)F^{(2)}_{E1} \tag{1.29}$$

where ϵ' and ϵ are the scattered and incident x-ray polarisation vectors, respectively, defined in section 1.3.4, $\hat{\mathbf{z}}$ is a unit vector in the direction of the magnetic moment,

and $F_{E1}^{(0)}$, $F_{E1}^{(1)}$ and $F_{E1}^{(2)}$ are defined in reference 49. The three terms of the above equation each give different responses to the polarisation state of the x-ray. The first term is independent of moment direction, and so is isotropic. The second term depends linearly on the moment direction, and gives rise to first harmonic magnetic satellites of Bragg reflections (from the Thomson cross section) via an anisotropic scattering process. The final term, quadratic in $\hat{\mathbf{z}}_j$, gives second harmonic satellites, but only in the case of spiral magnetic structures [48]. In this thesis we are concerned with investigating approximately collinear magnetic structures, and as such we are only interested in the second term of equation 1.29. We note that, when scattering at the $L_{\rm III}$-edge of rare-earth ions, $F_{E1}^{(1)}$ is directly proportional to the net number of spin up electrons in the 5*d* band, and inversely proportional to the broadening of the 5*d* band due to exchange splitting induced by the 4*f* moment [48].

The expansion of the spherical harmonics describing the polarisation dependence of the E2-E2 scattering amplitude contains thirteen terms up to fourth order. Here, we present only those relevant to the magnetic scattering observed in this thesis; that is those up to first order describing the first harmonic satellites. f_{E2-E2}^{RXS} is then written as follows:

$$f_{E2-E2}^{RXS} = (\hat{\mathbf{k}}' \cdot \hat{\mathbf{k}})(\epsilon' \cdot \epsilon)F_{E2}^{(0)} - i[(\hat{\mathbf{k}}' \cdot \hat{\mathbf{k}})(\hat{\epsilon}' \times \hat{\epsilon}) \cdot \hat{\mathbf{z}} + (\hat{\mathbf{k}}' \times \hat{\mathbf{k}})(\hat{\epsilon}' \cdot \hat{\epsilon}) \cdot \hat{\mathbf{z}}]F_{E2}^{(1)} \quad (1.30)$$

Equations 1.29 and 1.30 have been reformulated by Hill and McMorrow [49] such that the individual terms are described in cartesian coordinates, dependent upon the orthogonal magnetic moment components and the Bragg angle, θ. This is particularly useful when considering which components of the magnetic moment contribute to the scattering amplitude for a particular experimental geometry. The E1-E1 scattering amplitude is written as follows:

$$
\begin{aligned}
f^{RXS}_{E1-E1} &= F^{(0)}_{E1}\begin{pmatrix} 1 & 0 \\ 0 & \cos 2\theta \end{pmatrix} - iF^{(1)}_{E1}\begin{pmatrix} 0 & z_1\cos\theta + z_3\sin\theta \\ z_3\sin\theta - z_1\cos\theta & -z_2\sin 2\theta \end{pmatrix} \\
&+ F^{(2)}_{E1}\begin{pmatrix} z_2^2 & -z_2(z_1\sin\theta - z_3\cos\theta) \\ z_2(z_1\sin\theta + z_3\cos\theta) & -\cos^2\theta(z_1^2\tan^2\theta + z_3^2) \end{pmatrix}
\end{aligned} \tag{1.31}
$$

where the basis of the arrays are the four possible polarisation states;

$$
\begin{pmatrix} \sigma - \sigma' & \sigma - \pi' \\ \pi - \sigma' & \pi - \pi' \end{pmatrix}
$$

The polarisation channels, σ and π, are shown in figure 1.7 and the basis states are explicitly defined as $\epsilon_\sigma = \mathbf{u_2}$ and $\epsilon_\pi = -\sin\theta\mathbf{u_1} - \cos\theta\mathbf{u_3}$.

Some important physical consequences are now apparent. The first term does not allow any rotation of polarisation, *i.e.* $\epsilon' = \epsilon$. Also, as is the case for Thomson scattering, the π scattering has a $\cos 2\theta$ drop off. The second term does allow a rotation of the polarisation upon scattering. Furthermore, the polarisation state into which the x-rays scatter is dependent upon the direction of the magnetic moment. The fact that $\sigma - \sigma'$ scattering is forbidden at magnetic satellites provides a useful test to differentiate between charge scatter (all $\sigma - \sigma'$) and magnetic diffraction.

The E2-E2 scattering amplitude written in this form is far more extensive and of less use in describing any frequently observed physical effects. As such we refer the reader to reference 49.

1.3.4 Resonant x-ray scattering experimental geometry

To apply the above theory to the analysis of experimental results it is important to clearly define the experimental geometry and its relationship to the theoretical coor-

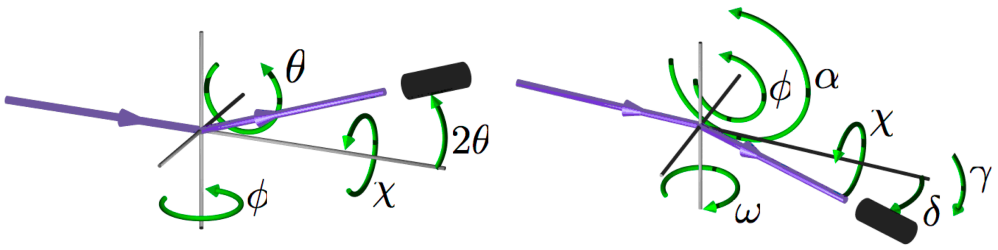

(a) 4-circle (b) 6-circle

Figure 1.4: Experimental diffractometer geometries drawn in the laboratory reference frame. The x-ray beam is drawn in purple, entering horizontally from the left. The detector position is illustrated by the black cylinder. The 4-circle geometry is shown with a vertical scattering plane, and the 6-circle with a horizontal scattering plane, as used in the experimental chapters of this thesis.

dinate systems. The diffraction condition is met by precisely orientating the single crystal sample with respect to the incident beam, such that the scattered intensity is detected at a given 2θ angle. This is achieved by using high precision diffractometers. The sample is mounted on a motorised goniometer, often with different sample environment capabilities such as temperature control, and high applied magnetic and electric fields. The detector is independently positioned in the scattering plane. Two diffractometer geometries have been employed in the resonant x-ray diffraction (RXD) experiments presented in this thesis; these are 4-circle [54] and 6-circle [55]. Both geometries may be used in vertical and horizontal scattering. Figure 1.4 illustrates the two geometries with the 4-circle shown in vertical scattering and the 6-circle in horizontal scattering, for greater relevance later in this thesis.

The rotations shown in figure 1.4 are coupled in the following order. In 4-circle geometry the sample is mounted on a xyz translation stage on top of the ϕ rotation, then the χ rotation, and finally the θ rotation. The 2θ circle rotates independently, defining the scattering plane. In 6-circle geometry, the same sample motions are

found (θ is equivalent to ω when α = 0). The main difference lies in the coupling of the detector motions, δ and γ.

In addition to the above experimental setups, a post-scatter polarisation analyser may be employed in order to determine the polarisation of the scattered beam. Figure 1.5(a) illustrates the use of a polarisation analyser crystal. By convention, the polarisation of an x-ray beam perpendicular or parallel to the scattering plane is labelled with a σ or π, respectively, as shown in the figure. Primes refer to the scattered beam. In general, the polarisation is written in terms of Poincaré-Stokes parameters that are defined as

$$\mathrm{P1} = (I_{\sigma'} - I_{\pi'})/I_0 \tag{1.32a}$$

$$\mathrm{P2} = (I_{+45^{\circ}{}'} - I_{-45^{\circ}{}'})/I_0 \tag{1.32b}$$

$$\mathrm{P3} = (I_{\circlearrowright'} - I_{\circlearrowleft'})/I_0 \tag{1.32c}$$

where I_0 is the total scattered intensity, $I_{\sigma'}$ and $I_{\pi'}$ are the scattered intensities of the linear polarisation components perpendicular and parallel to the scattering plane, $I_{+45^{\circ}{}'}$ and $I_{-45^{\circ}{}'}$ are the intensities of the linear polarisation components midway between σ' and π', and $I_{\circlearrowright'}$ and $I_{\circlearrowleft'}$ are the intensities of right- and left-handed circularly polarised light. These self-normalising parameters vary from +1 to -1, where P1 describes the degree of σ or π linearly polarised light, P2, the degree of $\pm 45^{\circ}$ linearly polarised light, and P3, the degree of right or left handed circularly polarised light [56].

The polarisation analyser is used to determine the linear components, P1 and P2, of the scattered beam. The analyser crystal is selected and cut such that the beam Bragg diffracts with minimum absorption close to Brewster's angle of 45°; hence, only scattering x-rays with incident polarisation perpendicular to the analyser scattering plane. Therefore by rotating the analyser crystal about the scattered beam by

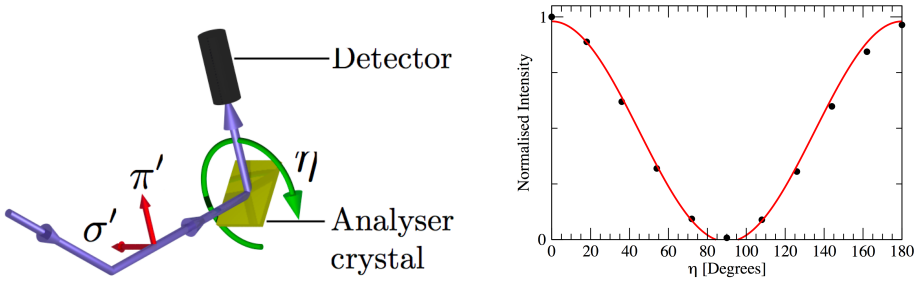

(a) Polarisation analyser (b) Poincaré-Stokes curve

Figure 1.5: (a) The polarisation analyser experimental setup. σ' and π' denote the polarisation of the scattered beam with respect to the scattering plane. The analyser crystal is rotated about the scattered beam by the angle η. (b) The result of polarisation analysis of the direct, σ-polarised beam. The data points, shown in black, were measured using a pyrolytic graphite analyser crystal scattering at the (004) Bragg reflection, with incident x-ray energy of 5.484 keV. The red line is the Poincaré-Stokes fit.

an angle η, a polarisation selective measurement can be made. The Poincaré-Stokes parameters were determined by fitting the integrated intensity of the analyser rocking curve as a function of η to the following equation [57]

$$I = \frac{I_0}{2}[1 + \mathrm{P1}\cos 2\eta + \mathrm{P2}\sin 2\eta], \tag{1.33}$$

where $\eta = 0^\circ$ and $\eta = 90^\circ$ correspond to polarisation perpendicular, ϵ'_σ, and parallel, ϵ'_π to the scattering plane, respectively. An example of this fitting is shown for the direct σ-polarised beam in figure 1.5(b).

It is also possible to manipulate the polarisation of the incident light. This is done by use of a diamond phase plate, shown in figure 1.6. Dynamical theory shows that birefringence occurs in perfect crystals when scattering at, or near, a Bragg reflection. Experimentally, the polarisation ellipticity and handedness induced by the birefringence is determined by the thickness of the crystal and the deviance from the Bragg angle [58, 59]. The efficiency of the phase plate is therefore limited

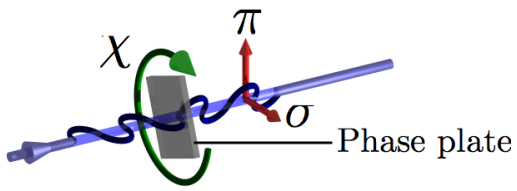

Figure 1.6: The phase plate experimental setup in the incident beam. Again, the polarisation with respect to the scattering plane is denoted by σ and π. The phase plate is rotated on the χ circle to select the desired linear polarisation.

by the beam divergence. Far from the Bragg condition the incident polarisation is unrotated. As the Bragg condition is approached, a phase difference between σ and π channels relative to the crystal is induced and elliptically polarised light is produced. At a particular deviation a π phase difference is induced and the phase plate behaves as a half wave plate. By maintaining this deviation from the Bragg condition and rotating on a χ-circle about the beam, any orientation of linearly polarised light can be selected [60].

In this thesis we analyse the resonant x-ray diffraction (RXD) data with reference to a cartesian coordinate system as defined by Blume and Gibbs [50], shown in figure 1.7.

1.4 Computational simulation

In Chapter 2, we present neutron powder diffraction data of Er_2CoGa_8 and Tm_2CoGa_8 intermetallics, measured with the aim of determining the respective rare-earth magnetic structures by fitting the diffraction data with the possible, symmetry allowed theoretical models. This was achieved through Rietveld analysis [61] by employing the FULLPROF software package [24]. In Chapter 4, we have investigated the antiferromagnetic spin polarisation of oxygen ions in $TbMn_2O_5$ through fitting oxygen *K*-edge resonant x-ray diffraction energy spectra. To do so, the *ab-initio* FDMNES

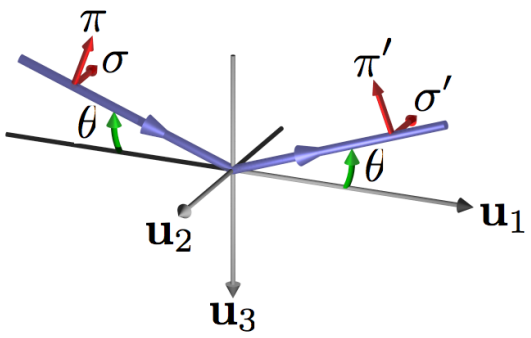

Figure 1.7: The coordinate system, defined by Blume and Gibbs [50], used in the following analysis of RXD data.

package [25] was employed. Both computational methods for simulating the respective diffraction data are described in the following sections.

1.4.1 Rietveld Analysis

In single crystal neutron diffraction structural refinements, a large number of Bragg reflections are measured and individually resolved. The complication with powder diffraction structural refinements is that a number of Bragg reflections will overlay and contribute to a single peak in the diffraction pattern. This problem has been successfully resolved in the Rietveld method [61]. This computational fitting procedure is based upon the least squares refinement of parameters that describe a user defined model. These parameters split into four main groups, those of the crystal structure, the diffraction peak profile, the diffraction optics and the instrumental factors. All parameters must be refined for a successful fit to the data, however in some cases constraints may be included [62]. Powder diffraction is a flexible technique, where data may be measured using both x-rays and neutrons as a function of energy (TOF), d-spacing, 2θ and $\mathbf{Q}$. Rietveld analysis can be employed in all of these formats.

The least squares residual, S, which is to be minimised, is defined as

$$S_y = \sum_i w_i (y_i - y_{ci})^2 \tag{1.34}$$

where y_i is the observed intensity at the ith step of the diffraction pattern, y_{ci} is the calculated intensity at the ith step and $w_i = \frac{1}{y_i}$. The calculated intensity, y_{ci} is determined using the following equation (given for the case of a powder pattern measured as a function of 2θ)

$$y_{ci} = s \sum_K L_K |F_K|^2 \phi(2\theta_i - 2\theta_K) P_K A + y_{bi} \tag{1.35}$$

where s is the scale factor, K denotes a given Bragg reflection, L_K contains the Lorentz, polarisation and multiplicity factors, ϕ is the reflection profile function, P_K is the preferential orientation function, A is an absorption factor, F_K is the structure factor of the Kth Bragg reflection and y_{bi} is the background intensity [62].

The least squares refinement is performed by finding the partial derivatives of y_{ci} as a function of each free parameter. This is a non-linear calculation and must be solved through an iterative procedure. As such, to avoid a divergent solution or a local minima, one requires a good initial guess for the model. Rietveld analysis is therefore not a structure solution algorithm, only a structural refinement procedure.

It is possible to model and fit a number of different phases, simultaneously. In this way impurities or instrumental anomalies may be included. Also, in the case of magnetic materials, a phase may be added to account for the additional reflections from the magnetic structure factor (equation 1.17), and hence solve the magnetic structure.

The Rietveld refinement uses a number of R values to give an indication of how reliable the fit of the model is to the data once S has been minimised. The most useful value is R_{Bragg}, as it only reflects how well Bragg peaks of the simulation

and model fit. As such any other contamination or misfits are excluded. R_{Bragg} is given as

$$R_{Bragg} = \frac{\sum |I_K(\text{obs}) - I_K(\text{calc})|}{\sum I_K(\text{obs})} \tag{1.36}$$

where I_K is the intensity of the Kth Bragg reflection.

It is clearly essential to have an estimation of the error (standard deviation) of the fitted parameter values. This is calculated using:

$$\sigma_j = \left[M_{jj}^{-1} \frac{\sum w_i (y_i(o) - y_i(c))^2}{N - P + C} \right]^{\frac{1}{2}} \tag{1.37}$$

where j denotes the parameter in question, M_{jj}^{-1} is the diagonal element of the inverse normal matrix of the least squares procedure, N is the number of y_i's used, P is the number of free parameters and C is the number of constraints.

Amongst a number of software packages that implement Rietveld analysis, we employ the FULLPROF package [24] to analyse the neutron powder diffraction data presented in Chapter 2.

1.4.2 FDMNES calculations

The FDMNES code (Finite Difference Method Near Edge Spectroscopy) [25], primarily written to calculate x-ray absorption near edge spectra (XANES), can also be used to calculate resonant x-ray diffraction (RXD) spectra [63–66]. As described in the previous section, in RXD we essentially measure the transition probability of a virtual excitation and relaxation between a core initial state and some final state. The initial state is relatively easy to evaluate, as the integral can be performed within the atomic radius. The transition matrix is also simple to calculate. The difficulty in these calculations lies in the evaluation of the final states [25].

The final states are calculated using density functional theory (DFT) and the local density approximation (LDA+U), where the electrostatic potential is deter-

mined through a choice of two methods. The first, used in the calculations in this thesis, considers a cluster of atoms surrounding the absorbing atom within the crystal lattice. As such multiple scattering theory is employed, where one calculates the interaction with backscattered x-rays from neighbouring atoms. The electrostatic potential is described by the muffin tin approximation. In this approximation the potential is spherically averaged in the proximity of the atoms, and volume averaged (constant) in the interstitial regions. Although this is clearly a harsh approximation, it works well for systems with high atomic density and high symmetry [25]. The second method, the finite difference method, avoids the approximations of multiple scattering theory and the muffin tin approximation, but is computationally very expensive. This would have been prohibitive in the calculation presented in Chapter 4.

The calculation is multi-atomic and mono-electronic. Only a single excitation of any given electron is considered. It is therefore only successful in predicting resonant transitions into delocalised states. For example the oxygen 2p states (K-edge), transition metal 4p states (K-edge) or the rare-earth 5d states (L_{II} and L_{III} edges). To calculate the transition into localised states one must consider the interaction with the core hole, and hence employ a multi-electronic calculation.

Furthermore, as the resonant terms in the form factor are anisotropic (tensorial) there is a geometric dependence on the scattered intensity when considering the polarisation of the incident and scattered x-rays and the anisotropy of the electronic environment within the sample. This is explained in the previous section. FDMNES can be used to successfully predict this phenomena.

In running the code, the main input parameters for the DFT calculation are the crystal (and magnetic) structure and the RXD reflections to be simulated, with their respective incident and scattered x-ray polarisations and azimuth angle. In addition, one sets the cluster radius, energy range and the excitation, *i.e.* E1-E1, E2-E2 etc.

It is also possible to output the self-absorption, useful for correcting the calculation to compare with experimental data. At this stage of the calculation, it is possible to retrieve the density of states of the absorbing atoms, and all the backscattering atoms within the cluster. Once the energy dependent scattering amplitudes are evaluated, the code performs a convolution with an arctangent function to simulate the broadening associated with the electronic transition. One can modify the parameters describing this broadening, such as the core and excited state lifetimes. The Fermi energy is also set, which essentially defines a lower energy cut-off, as the transition probability is zero when the final states are occupied.

Finally, the code also enables not only the simulation of spectra, but the possibility to fit a vast number of input parameters to a selection of measured energy spectra simultaneously.

1.5 Summary

In summary, we have explained how diffraction techniques provide a lucid probe of long-range electronic correlations in the solid state; phenomena that may give rise to fascinating new physics and technology. In this thesis we report diffraction studies of novel strongly correlated electron systems in which rare-earth magnetism plays a key role in the microscopic electronic behaviour, namely intermetallics Er_2CoGa_8 and Tm_2CoGa_8, and multiferroic compounds $TbMn_2O_5$ and $TmMn_2O_5$. Both x-ray and neutron diffraction processes have been described in detail, making clear the advantages and disadvantages of the two techniques, and providing the background theory necessary for the analysis and interpretation of the experimental results presented in the following chapters. We have also outlined two computational methods used within the thesis. One used for solving magnetic structures from neutron powder diffraction data, and the other for calculating resonant x-ray diffraction energy spectra. We have focused in particular on resonant x-ray diffraction, extensively

employed in this thesis to unravel complex magnetic systems with a number of different magnetic sub-lattices by exploiting the technique's inherent elemental and electronic state specificity.

Chapter 2

Magnetic structure determination of R_2CoGa_8 intermetallics

2.1 Intermetallics

Intermetallics are compounds of two or more metallic elements that form a single, solid phase with a crystal structure different to that of their constituents. This definition therefore excludes other alloys such as metal mixtures and interstitial compounds. These materials are particularly interesting in the study of magnetism. Developed in the 1970's, rare-earth intermetallic magnets, such as $SmCo_5$, were found to develop magnetic fields in excess of 1 T, far greater than any transition metal alloy permanent magnet. Current research has tended to focus on the more complex ternary compounds, RTX (with a variety of compositions), where in general R = rare-earth, T = transition metal, and X is another metal or semimetal. This is due to the discovery of some extreme macroscopic phenomena.

In 1979, $CeCu_2Si_2$ was found to undergo a transition into a superconducting ground state below $\sim$1 K that did not comply with the conventional Bardeen-Cooper-Schrieffer (BCS) theory of superconductivity [67]. This stimulated research, which

remains cutting edge today, into what have been termed unconventional superconductors. These include some of the high T_C materials, for example $YBa_2Cu_3O_{6.9}$ [68], which have been hugely influential in developing technologies. In the years since, there has been intense focus on the synthesis of other ternary rare-earth intermetallic compounds. This has lead to the growth of a group of materials that exhibit a diverse range of fascinating physical properties, for example heavy fermion behaviour in Ce_2RhIn_8 [69, 70], Kondo ground states in Ce_2CoIn_8 [71], quantum criticality in $YbRh_2Si_2$ and $CePd_2Si_2$ [72], and pressure induced superconductivity in $CeRhSi_3$ [73] and $CeIrSi_3$ [74].

It is surprising to find such a diverse range of macroscopic properties across a group of materials that often have similar crystallographic, and bulk magnetisation and transport properties. This is likely to be due to the competition of electronic interactions such as antiferromagnetism, Kondo effects and the crystal electric field (CEF) [71, 75, 76]. Microscopic probes such as x-ray and neutron diffraction can therefore provide a successful route to explaining the physical behaviour of these intermetallic materials. In this thesis we have studied the newly synthesised isostructural R_2CoGa_8 series (R = rare-earth), in particular the erbium and thulium based members, Er_2CoGa_8 and Tm_2CoGa_8.

2.2 The R_2CoGa_8 series

The R_2CoGa_8 series is limited to R = Gd - Lu and Y due to an instability in the crystallisation of the lighter rare-earth compounds [20, 21, 77]. The series is isostructural, adopting at room temperature the tetragonal space group $P4/mmm$. The crystal structure can be thought of as a stacking of RGa_3 units (which adopt the $AuCu_3$ type structure [78]) between $CoGa_2$ layers in the direction of the four-fold tetragonal axis. Figure 2.1 shows the crystal structure of the R_2CoGa_8 series [20] and that of the RGa_3 units for clarity.

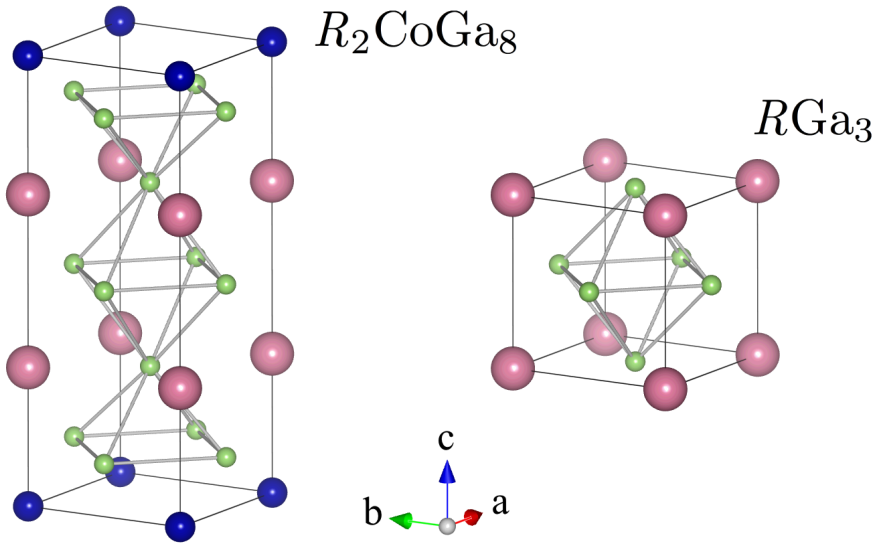

Figure 2.1: The crystal structures of tetragonal R_2CoGa_8 and cubic RGa_3. In both cases a single unit cell is shown, denoted by the black lines. The rare-earth, cobalt and gallium ions are shown as pink, blue and green spheres of decreasing size, respectively.

By comparing RGa_3 to R_2CoGa_8, the similar a lattice parameter and the requirement of heavier rare-earth mass for stable crystallisation suggests that the RGa_3 units are key building blocks in the formation of the ternary compound [20]. An analogous argument is also made for R_2CoIn_8 [20, 71] and Ce_2RhIn_8 [69]. Indeed, in Ce_2RhIn_8 this is supported by the common rare-earth magnetic structures of Ce_2RhIn_8 and $CeIn_3$ [69]. The effective layering of the ternary compounds along the c-axis is of importance when considering the dimensionality of the magnetic structure, as discussed later in this chapter.

A thorough survey of magnetisation, thermal, and transport properties of the R_2CoGa_8 compounds was published by Joshi *et al.* [20, 21]. Of particular interest is the dependence of the magnetic anisotropy upon the rare-earth ion radii. This splits the series into four groups. These are the diamagnetic compounds with R = Y and Lu, isotropic Gd_2CoGa_8 (as for Gd^{3+} $L = 0$), R = Tb, Dy and Ho compounds with a

magnetisation easy axis parallel to the *c*-axis and finally *R* = Er and Tm compounds, which have a magnetisation easy axis perpendicular to the *c*-axis.

In this study we focus on the latter erbium and thulium members. Magnetometry data are presented in figure 2.2. The two compounds were found to antiferromagnetically order at T_N = 3 and 2 K, respectively [20], as shown by the magnetic susceptibility data in figures 2.2(a) and 2.2(b). Clearly, all data sets showed that the magnetisation easy axis lies perpendicular to the *c*-axis for these two compounds. The polycrystalline average paramagnetic Curie temperatures given in reference 20, all of which are negative, become closer to zero on increasing rare-earth weight across the series. There is therefore a weakening of the antiferromagnetic exchange interaction dependent upon the rare-earth ion, with Tm_2CoGa_8 having the weakest. This is further evident in the magnetometry. The antiferromagnetic transition was only observable in Tm_2CoGa_8 in small applied fields (50 Oe) [20]. The transition was not seen in a 5 kOe applied field, as in the Er_2CoGa_8 measurement. A plot of the inverse susceptibility as a function of temperature of Er_2CoGa_8, not presented here, showed a crossover of the easy axis at 164 K, suggesting that Er_2CoGa_8 could be on the border between the easy axis lying either parallel or perpendicular to the *c*-axis. Figures 2.2(c) and 2.2(d) showed similar isothermal magnetic behaviour of the two samples, with saturation occurring at approximately 2 T. However, one must note the anisotropy crossover unique to Tm_2CoGa_8 at 11.2 Tesla.

The conclusions drawn from the magnetometry data were further supported by thermal and transport measurements [21]. Anomalies in the heat capacity of Er_2CoGa_8 and Tm_2CoGa_8, shown in figures 2.3(a) and 2.3(b), respectively, coincided with, and hence confirmed, the antiferromagnetic ordering temperatures. The trends in magnetic anisotropy across the R_2CoGa_8 series were reflected in magnetoresistance measurements. Further, resistivity measurements showed that the magnetic correlations can be quite different in different crystallographic directions

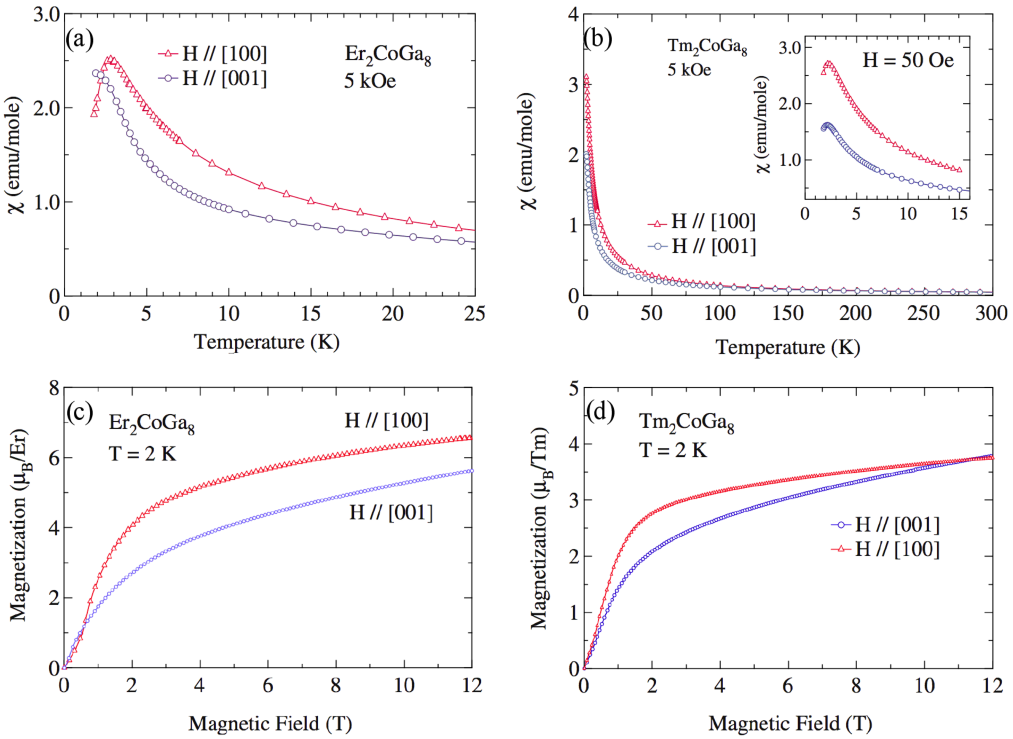

Figure 2.2: Magnetometry results of magnetic susceptibility against temperature for (a) Er_2CoGa_8 and (b) Tm_2CoGa_8 (inset shows the antiferromagnetic transition at low temperature), and isothermal magnetisation against applied magnetic field for (c) Er_2CoGa_8 and (d) Tm_2CoGa_8. Reprinted figures with permission from reference 20. Copyright 2008 by the American Physical Society.

dependent upon the choice of rare-earth ion, suggesting that a variety of magnetic structures may be found across the R_2CoGa_8 series [21].

To better understand the varied macroscopic properties of the R_2CoGa_8 series we require a probe of the microscopic electronic ordering phenomena. The only previously published magnetic structure of any member of the R_2CoGa_8 series was that of Ho_2CoGa_8, determined by magnetic resonant x-ray scattering [79]. It was found that, below T_N = 5.1 K, Ho_2CoGa_8 develops an antiferromagnetic structure with propagation vector $\mathbf{q} = (\frac{1}{2}, \frac{1}{2}, \frac{1}{2})$. Further, it was predicted that the rare-earth magnetic moments align in a collinear fashion, parallel to the c-axis.

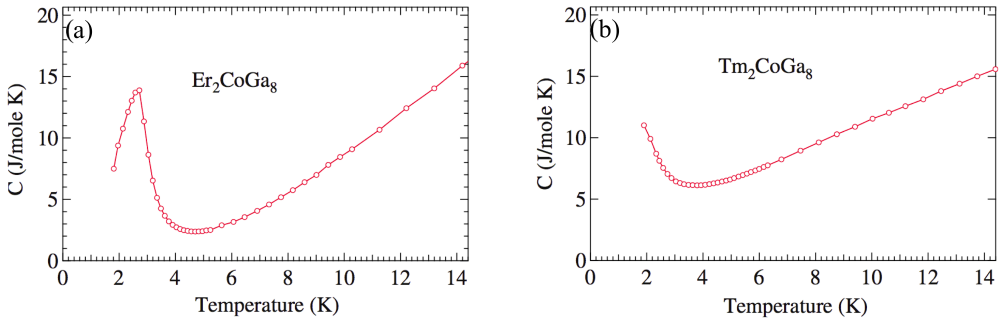

Figure 2.3: Heat capacity measurements against temperature for (a) Er_2CoGa_8 and (b) Tm_2CoGa_8. Reprinted figures with permission from reference 21. Copyright 2009 by the American Physical Society.

In our experiment, single crystal and powder Er_2CoGa_8 and Tm_2CoGa_8 samples were characterised through magnetometry. The antiferromagnetic structures of both compounds have then been solved through Rietveld refinement of neutron powder diffraction data. In spite of a common magnetic easy axis and similar structural characteristics, the magnetic structures of the two compounds were found to be different. This surprising result is discussed with reference to magnetic exchange interactions and CEF effects, known to be prevalent in such materials.

2.3 The crystal electric field

When ions are incorporated into crystalline solids, electronic properties such as magnetisation, heat capacity and optical spectra differ, often dramatically, from what would be predicted for the free ion. This is due to an electronic perturbation on the ion through an electrostatic interaction with its neighbours *i.e.* the crystal electric field (CEF). This results in a splitting of otherwise degenerate energy levels, evident in spectroscopic measurements. Furthermore, the CEF interaction usually induces a significant anisotropy in the system. In this section, some key results of

theoretical CEF calculations are outlined, however far greater detail may be found in the literature [22, 80, 81]. The Hamiltonian describing the magnetism of the system is modified accordingly, gaining an extra term $\mathcal{H}_{\mathrm{CEF}}$ *i.e.*

$$\mathcal{H}_{\mathrm{tot}} = \mathcal{H}_{\mathrm{Coul}} + \mathcal{H}_{\mathrm{exch}} + \mathcal{H}_{\mathrm{CEF}} + \mathcal{H}_{\mathrm{ms}} + \mathcal{H}_{\mathrm{ext}} \tag{2.1}$$

where $\mathcal{H}_{\mathrm{Coul}}$, $\mathcal{H}_{\mathrm{exch}}$, $\mathcal{H}_{\mathrm{ms}}$ and $\mathcal{H}_{\mathrm{ext}}$ are terms describing the Coulomb interaction, magnetic exchange interaction, magneto-striction and any external magnetic field, respectively. The CEF perturbation may be written in general as

$$\mathcal{H}_{\mathrm{CEF}} = \sum_{n,m} A_n^m \langle r^n \rangle O_n \hat{O}_n^m \tag{2.2}$$

where A_n^m and O_n^m are the CEF parameters and Stevens operators, respectively [22, 82]. This summation is limited by two important factors. Firstly, all odd-n terms vanish for configurations with equivalent electrons. Secondly, for lanthanide ions (4f electrons), only terms with $n \leq 6$ are applicable [81]. The summation is often simplified further, as for ions occupying high symmetry point groups, only a small number of terms are found to be non-zero. Indeed, in tetragonal point group symmetry C_{4v}, that of the rare-earth ions in R_2CoGa_8, the summation may be reduced to [71]

$$\mathcal{H}_{\mathrm{CEF}} = B_2^0 O_2^0 + B_4^0 O_4^0 + B_4^4 O_4^4 + B_6^0 O_6^0 + B_6^4 O_6^4 \tag{2.3}$$

where the CEF parameters are now $B_n^m = A_n^m \langle r^n \rangle O_n$ [81]. Theoretical determination of the CEF parameters is difficult, at best only assuming point charges. They are therefore usually determined experimentally from magnetometry data. Once found, they can form the basis of an elegant prediction of physical properties such as magnetic anisotropy, transition temperatures and thermal properties.

Table 2.1: CEF parameters and calculated magnetic exchange parameters for the R_2CoGa_8 series, calculated by Joshi *et al.*. Only B_2^0 is given, as the other parameters were shown to be negligible.

R	B_2^0 (K)	$\mathcal{J}_{ex}^{[100]}/k_B$ (K)	$\mathcal{J}_{ex}^{[001]}/k_B$ (K)
Tb	-1.61	-2.24	-4.94
Dy	-0.7	-1.28	-1.94
Ho	-0.22	-0.51	-0.59
Er	0.089	-0.35	-0.32
Tm	0.35	-0.53	-0.075

Joshi *et al.* [71] determined the CEF parameters for the R_2CoGa_8 series (given in table 2.1) by fitting inverse magnetic susceptibility data. It was found that B_2^0 dominates in equation 2.3, further simplifying the analysis. We note that the trend in B_2^0 across the series mirrors the trend in the electric quadrupole moment of single rare-earth ions [83]. Given that the series is iso-structural, this provides a clear indication that the different magnetic behaviour observed throughout the series is a result of differing occupation of the rare-earth $4f$ electronic states.

A key result of the CEF calculation is in predicting the Ruderman-Kittel-Kasuya-Yosida (RKKY) exchange constants, as defined in the introduction to this thesis, and discussed in context later in this chapter. Mean field theory relates the CEF parameters to the paramagnetic Curie temperature, θ_p, and the RKKY exchange constants as follows [84],

$$\theta_p^{[001]} = \frac{J(J+1)}{3k_B}\mathcal{J}_{ex}^{[001]} - \frac{(2J-1)(2J+3)}{5k_B}B_2^0 \quad (2.4)$$

$$\theta_p^{[100]} = \frac{J(J+1)}{3k_B}\mathcal{J}_{ex}^{[100]} + \frac{(2J-1)(2J+3)}{10k_B}B_2^0 \quad (2.5)$$

Substituting in the experimentally determined paramagnetic Curie temperature and the CEF parameter gives the results presented in table 2.1 (J is determined

assuming a definite ionisation state of the lanthanide ions). The RKKY exchange constants were all found to be negative, showing that antiferromagnetism is dominant in these materials. We note the change of sign of the CEF parameter upon increasing rare-earth weight. This is indicative of a change in magnetic anisotropy, *i.e.* the rotation of the magnetic easy axis from parallel to the *c*-axis (Tb, Dy and Ho) to perpendicular to the *c*-axis (Er and Tm). The fact that for the erbium based compound B_2^0 is close to zero supports the conclusion that Er_2CoGa_8 is on the turning point between different magnetic anisotropies [71].

Another result of the CEF calculations, not discussed in detail here but still noteworthy, is in explaining antiferromagnetic transition temperatures that are experimentally found to be higher than that predicted by de Gennes scaling [17]. Indeed, it was shown to be necessary to include CEF effects when predicting $T_{\rm N}$ for the R_2CoGa_8 series [71]. In the presence of the CEF, the ground state wave function is an admixture of wave functions with common total angular momentum, **J**, but different **M**; the projection of **J** in the z-direction [81]. This results in the expectation value of the magnetic moment in the z-direction being less than that of the free ion. As such, in our magnetic structure refinement we would anticipate refining magnetic moment magnitudes for the rare-earth ions lower than their theoretical free ion values.

The CEF also has interesting consequences for the thermal behaviour of the material. The Schottky heat capacity is defined as [20]

$$C_{\rm Sch} = \frac{\partial}{\partial T}\left[\frac{1}{Z}\sum_n E_n \exp\left(-\frac{E_n}{k_{\rm B}T}\right)\right] \tag{2.6}$$

where Z is the partition function [81] and E_n are the energy levels determined by the CEF. When compared to experimental data for the lanthanide $4f$ contribution to the heat capacity [20], the theoretical Schottky heat capacity agreed well with data measured on the Tb, Dy and Ho based compounds. However, no good agree-

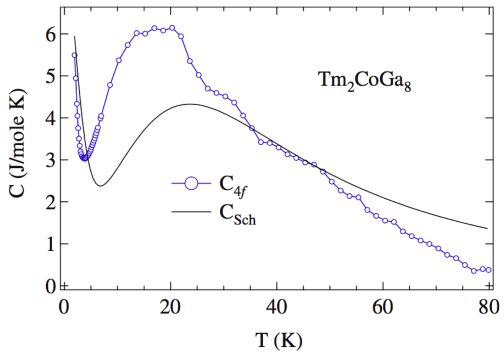

Figure 2.4: The thulium $4f$ electronic contribution towards the heat capacity (blue circles) and the Schottky heat capacity (black line) calculated from the crystal electric field energy levels. Reprinted figures with permission from reference 21. Copyright 2008 by the American Physical Society.

ment was observed with the Er_2CoGa_8 data. The Tm_2CoGa_8 data and calculation are shown in figure 2.4. Here, experiment and theory are only in reasonable agreement. Perhaps, therefore, the CEF parameters determined by Joshi *et al.*, are not completely satisfactory in describing the physical behaviour of the Er_2CoGa_8 and Tm_2CoGa_8 compounds.

2.4 Experiment

Single crystal samples of Er_2CoGa_8 and Tm_2CoGa_8 were grown by the gallium flux technique [85] by our collaborators, C. Adriano, C. Giles and P. G. Pagliuso at the Universidade Estadual de Campinas, Brazil. Their lab-based x-ray powder diffraction data refinements confirmed the Er_2CoGa_8 and Tm_2CoGa_8 room-temperature crystal structures to be tetragonal ($P4/mmm$), with lattice parameters a = 4.210(5) Å and c = 10.96(1) Å, and a = 4.202(5) Å and c = 10.95(1) Å, respectively.

Approximately 1 g of each sample was prepared for neutron powder diffraction

by grinding a number of single crystals using an agate pestle and mortar. This gave fine powders of consistent grain size. From these 1 g samples, approximately 0.04 g was removed and prepared for magnetometry measurements.

Both single crystal (aligned such that the measurement was made parallel to the a-axis) and powder, Er_2CoGa_8 and Tm_2CoGa_8 samples were characterised through magnetometry by employing a Quantum Design magnetic properties measurement system (MPMS) [86] designed to measure the sample magnetisation as a function of temperature (1.8 to 300 K) and applied magnetic field (up to $\pm$5 T).

The MPMS employs a radio frequency superconducting quantum interference device (SQUID). This device is based upon the AC Josephson effect [87] and comprises a superconducting loop, linked by a Josephson junction, inductively coupled to a resonant tank circuit. The quantisation of flux constrains the flux enclosed within the superconducting ring, and hence the phase difference across the Josephson junction. This in turn determines the current flowing around the ring. For a given external flux, the ring current exceeds the critical current of the junction, the voltage across which is then momentarily non-zero. This is detected by the resonant tank circuit via inductance. The voltage of the tank circuit increases with a step like trend as a function of external flux, giving essentially an external flux quantum counter [88]. This, as well as inherently having very low noise, makes the SQUID extremely sensitive to small magnetic moments.

Having zero field cooled (ZFC) to base temperature, the magnetisation of all the samples was measured in a small applied field (as in figure 2.2) in the temperature range 1.8 K to 20 K. We then measured the isothermal magnetisation of the single crystal samples against applied magnetic field at 1.8 K, between -5 T and 5 T.

Neutron powder diffraction data were collected on both samples using WISH [89], the newly built time-of-flight (TOF) instrument on the second target station at the UK neutron spallation source, ISIS [90]. At ISIS, H^- ions are generated

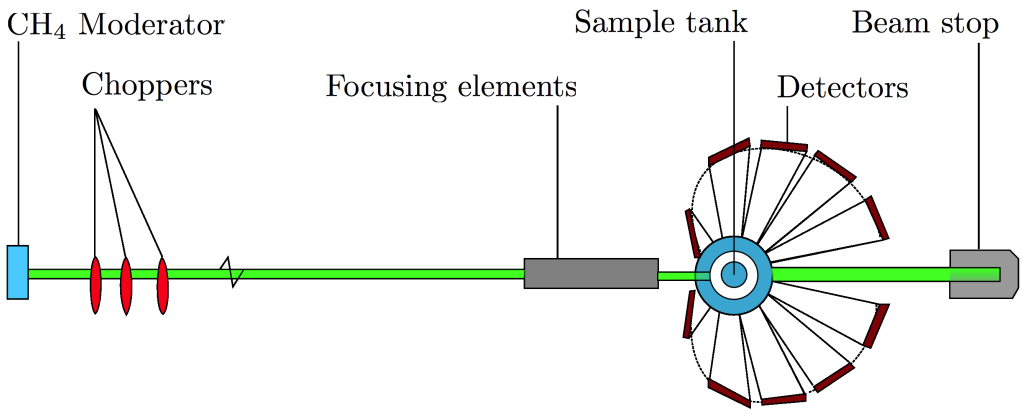

Figure 2.5: Schematic of the WISH instrument adapted from reference 89, highlighting some of the important components.

from hydrogen gas in a discharge plasma. They are then accelerated to 800 MeV, first by a radio frequency quadrupole accelerator, then a LINAC, and finally in a synchrotron. Just before entering the synchrotron electrons are stripped from the H^- ions by an aluminium oxide foil, leaving a proton beam. The beam is initially pulsed by the LINAC with 200 μs pulses. These pulses are then shortened by the synchrotron to 100 ns, once fully accelerated. The proton beam is then guided to two tungsten targets (and one carbon target for muon production) where neutrons are produced through spallation. WISH is located on the low power, low repetition rate, target station 2, which is optimised for the production of long wavelength neutrons; ideal for magnetic structure determination. In this experiment, pulsed neutrons were moderated by a decoupled liquid methane moderator, however, future plans are to run with solid methane to improve performance.

WISH is primarily designed as a TOF powder diffractometer, with the additional capability to perform single-crystal or polarised experiments. The instrument is optimised to achieve high resolution at long d-spacing (0.7 - 17 Å), with the aim of solving some of the most complex magnetic structures. Figure 2.5 is a schematic of the instrument layout. The neutron beam is first conditioned by choppers close to

the moderator and then guided over approximately 50 m, giving excellent TOF resolution. Interchangeable focusing elements allow the user to manipulate the beam from the unfocused size of 20 x 40 mm, to a super focused spot of 1 x 1 mm at the sample position. In this experiment we used an unfocused beam. Five banks of ^{3}He detectors, covering an angular range of 10° to 175°, surround the sample tank. These therefore cover at low angle (bank 1) the long d-spacing reflections, whilst maintaining very high resolution at high angles (bank 5) of the shorter d-spacing reflections. Such a detector array enables the collection of a colossal amount of TOF data, permitting relatively short collection times.

In this experiment, a ^{3}He sorption insert was employed within a standard Oxford Instruments cryostat to achieve sample temperatures of less than 300 mK. Each sample was loaded into a 6 mm diameter vanadium can with a thick copper head, covered with a cadmium mask, placed in contact with the ^{3}He pot. A copper wire (cold finger) was run through the length of the can to ensure better thermal conductivity through the sample. Data were collected with high counting statistics above $T_{\rm N}$ and at 300 mK, the base temperature of the ^{3}He insert. Shorter data collections were performed upon warming through the transition to determine the temperature dependence of the magnetic scattered intensity. Determinations of the nuclear and magnetic structures were performed using the FULLPROF suite of programs [24], as discussed in the introduction.

2.5 Results and Discussion

2.5.1 Magnetometry

Figure 2.6 shows the magnetometry results of the samples used in our neutron diffraction experiment. Figures 2.6(a) and 2.6(b) give the magnetic susceptibility of both single crystal and powder samples, measured as a function of temperature.

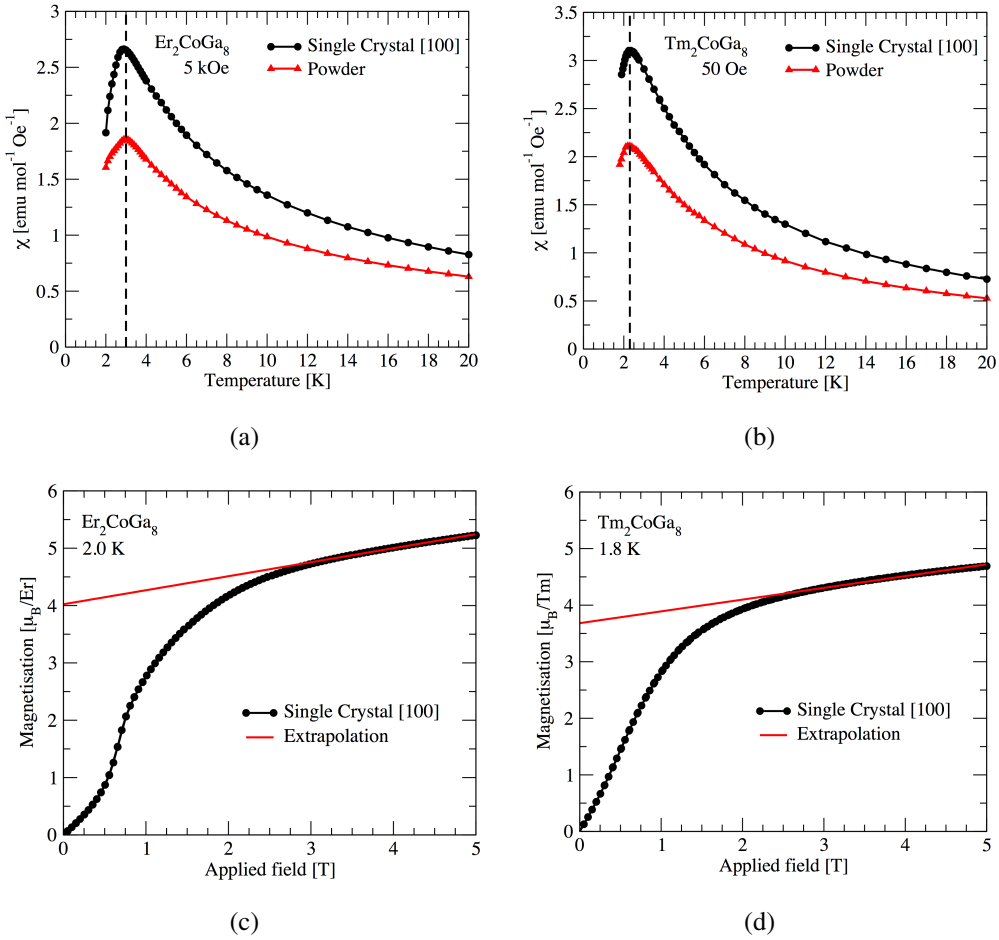

Figure 2.6: Magnetometry results for our samples with magnetic susceptibility against temperature for (a) Er_2CoGa_8 and (b) Tm_2CoGa_8, and isothermal, magnetisation against applied magnetic field for (c) Er_2CoGa_8 and (d) Tm_2CoGa_8.

T_N was found to be 3.0 K and 2.2 K for the Er_2CoGa_8 and Tm_2CoGa_8 samples, respectively. The data reproduce that published (figure 2.2 [20]), showing our samples to be comparable to those already studied. Importantly, it is also clear that the magnetic properties of the samples were not altered upon powdering. As the single crystal measurement was performed along the [100] easy axis, the lower magnetisation apparent in the powder sample is simply due to the powder average.

Figures 2.6(c) and 2.6(d) give the isothermal magnetisation measured as a func-

tion of applied field for both single crystal samples. Both data trends are in good agreement with that published [20], however it is surprising to find that the magnetisation of our Tm_2CoGa_8 sample at 5 T was approximately 40 % larger than that presented in the literature, particularly when considering the fine result in figure 2.6(b). The high field section of the curve is extrapolated down to zero field in order to make a prediction of the rare-earth moments. These were found to be 4.0 μ_B/Er and 3.7 μ_B/Tm. A similar analysis performed on the data measured by Joshi *et al.* [20] gave zero field rare-earth moment values of 4.6 μ_B/Er and 2.90 μ_B/Tm. The difference in the erbium moments is due to our measurement being limited to 5 T. Extrapolating data from higher fields will give a higher, more accurate zero field moment. The difference in the predicted thulium moments is due to the surprisingly high magnetisation measured by us, which remains unexplained.

2.5.2 Neutron powder diffraction

Figures 2.7 & 2.8 and 2.9 & 2.10 show the neutron powder diffraction patterns, plotted against d-spacing, above and below the antiferromagnetic transition for Er_2CoGa_8 and Tm_2CoGa_8, respectively. The Rietveld refinement, discussed in the following paragraphs, is overlaid, with the associated tick marks and difference pattern shown under the diffraction data. In all data sets, a peak at $d \sim 2.43$ Å was shown to be anomalous, and so has been excluded from all refinements (blanked in figures 2.7 to 2.10).

The crystal structures of both compounds were refined both above and below T_N in the tetragonal $P4/mmm$ space group, as has been reported for Ho_2CoGa_8 [20]. In order to properly reproduce the experimental data, it was necessary to account for additional reflections due to extraneous scatter from the sample can. We therefore included in the refinements a copper nuclear phase (Cu cold finger). This phase was fitted by Le Bail intensity fitting [91] as the copper wire was found to be textured.

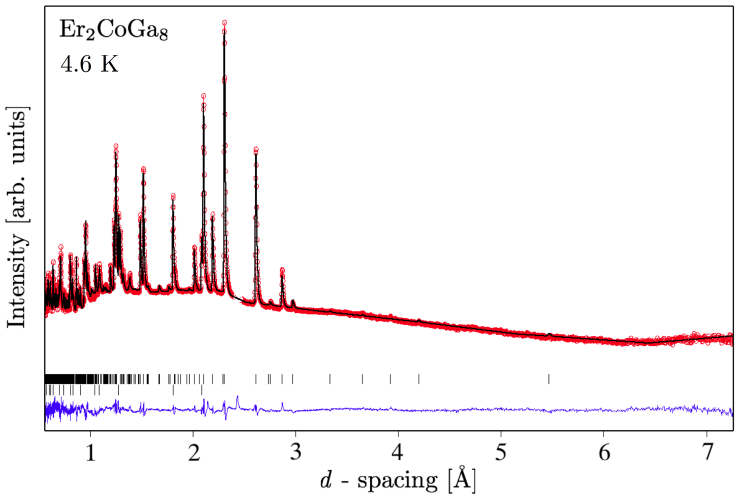

Figure 2.7: Rietveld refinement pattern for Er_2CoGa_8 at 4.6 K. The top and bottom tick marks refer to Er_2CoGa_8-nuclear, and Cu-nuclear (cold finger) phases, respectively. The difference pattern is shown at the bottom of the figure (blue line).

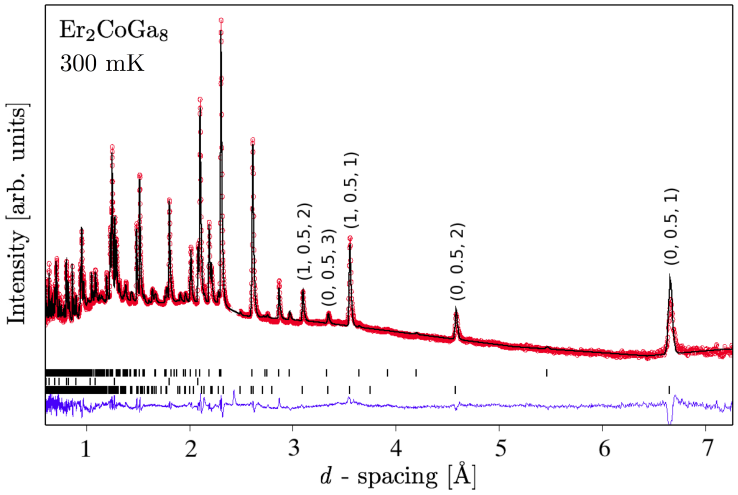

Figure 2.8: Rietveld refinement pattern for Er_2CoGa_8 at 300 mK. The top, middle and bottom tick marks refer to Er_2CoGa_8-nuclear, Cu-nuclear (cold finger) and Er_2CoGa_8-magnetic phases, respectively. The difference pattern is shown at the bottom of the figure (blue line). A number of prominent magnetic reflections are indexed.

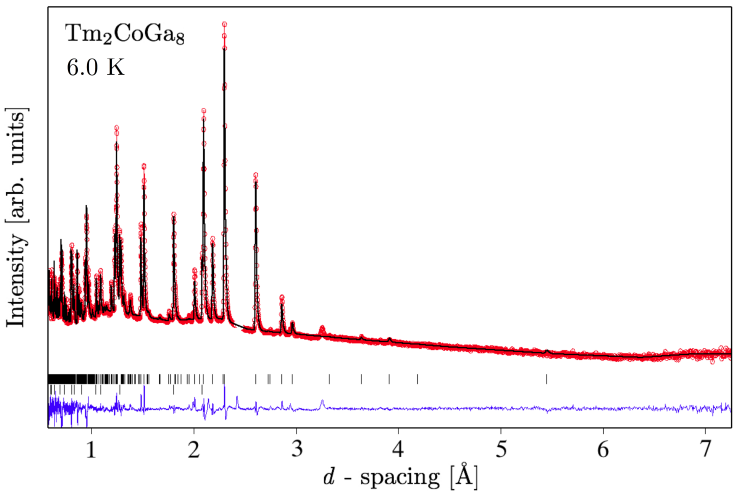

Figure 2.9: Rietveld refinement pattern for Tm_2CoGa_8 at 6.0 K. The top and bottom tick marks refer to Tm_2CoGa_8-nuclear, and Cu-nuclear (cold finger) phases, respectively. The difference pattern is shown at the bottom of the figure (blue line).

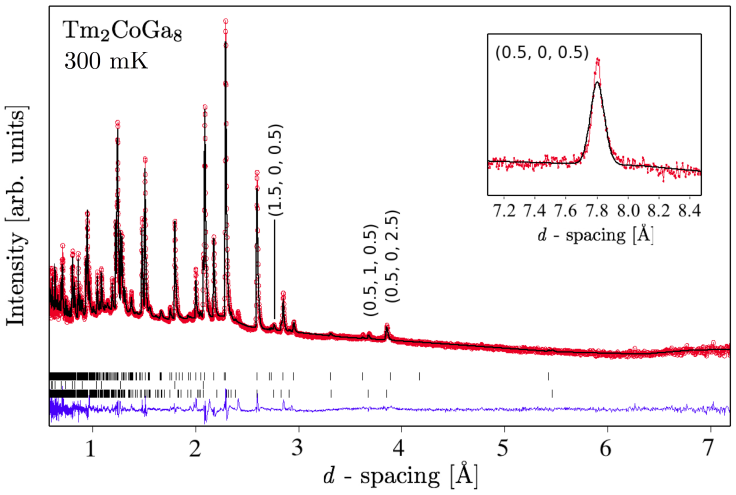

Figure 2.10: Rietveld refinement pattern for Tm_2CoGa_8 at 300 mK. The top, middle and bottom tick marks refer to Tm_2CoGa_8-nuclear, Cu-nuclear (cold finger) and Tm_2CoGa_8-magnetic phases, respectively. The difference pattern is shown at the bottom of the figure (blue line). A number of prominent magnetic reflections are indexed.

Tables 2.2 and 2.3 give the lattice parameters and structural parameters refined for both materials. It is clear that within the high accuracy of the refinement there are no statistically significant changes of lattice or structural parameters occurring upon the magnetic transition, indicating that the magneto-elastic coupling was negligibly small in both materials.

Table 2.2: Lattice parameters of Er_2CoGa_8 and Tm_2CoGa_8 refined in space group $P4/mmm$ from neutron powder data.

	Er_2CoGa_8		Tm_2CoGa_8	
	300 mK	4.6 K	300 mK	6.0 K
a (Å)	4.20195(5)	4.20187(4)	4.18980(7)	4.18988(6)
c (Å)	10.9438(2)	10.9433(2)	10.9109(3)	10.9107(3)

By comparing the powder patterns measured above T_N and at 300 mK, a large number of additional magnetic reflections became evident. We investigated the behaviour of the magnetic phase of both Er_2CoGa_8 and Tm_2CoGa_8 upon warming through the transition. The integrated intensities of selected magnetic diffraction peaks are plotted as a function of temperature in figure 2.11, clearly showing transition temperatures of 3.0 and 2.0 K for Er_2CoGa_8 and Tm_2CoGa_8, respectively. This is in good agreement with the bulk magnetometry results measured in this study (figure 2.6), and those in reference 20 (figure 2.2).

Upon antiferromagnetic ordering a continuous phase transition occurs at the critical temperature (T_N). At the transition symmetry is broken within the crystal. This symmetry breaking is represented by an order parameter, which in the case of magnetism is the magnetisation, **M**. Critical phase transitions are theoretically described by the Ginzberg-Landau theory, or mean field theory [92, 93]. However, this theory only successfully predicts experimental data of a small number of phase transitions, for example that in type-I superconductors [93]. A more satisfactory

Table 2.3: Structural and magnetic parameters of Er_2CoGa_8 and Tm_2CoGa_8 refined above and below T_N. The direction of the magnetic moments of the rare-earth ions are chosen to lie parallel to the *b*-axis (as opposed to the *a*-axis).

		Er_2CoGa_8		Tm_2CoGa_8	
Atom		300 mK	4.6 K	300 mK	6.0 K
R (1)	*x*	0	0	0	0
	y	0	0	0	0
	z	0.3068(3)	0.3083(5)	0.2964(7)	0.2958(7)
	$\mu_B \| b$	4.71(3)	-	2.35(4)	-
R (2)	*x*	0	0	0	0
	y	0	0	0	0
	z	-0.3068(3)	-0.3083(5)	-0.2964(7)	-0.2958(7)
	$\mu_B \| b$	-4.71(3)	-	-2.35(4)	-
Co	*x*	0	0	0	0
	y	0	0	0	0
	z	0	0	0	0
Ga (1)	*x*	0	0	0	0
	y	0.5	0.5	0.5	0.5
	z	0.5	0.5	0.5	0.5
Ga (2)	*x*	0.5	0.5	0.5	0.5
	y	0.5	0.5	0.5	0.5
	z	0.2952(5)	0.2945(5)	0.3100(6)	0.3076(6)
Ga (3)	*x*	0	0	0	0
	y	0.5	0.5	0.5	0.5
	z	0.1177(2)	0.1175(2)	0.1176(2)	0.1181(2)

approach is to describe the physical behaviour of the system by a simple power law and the universality hypothesis [94, 95]. Although unproven, this has been shown to be effective in predicting a wealth of experimental data. For the intensity of magnetic diffraction peaks that scale as the square of the magnetisation, the power law may be written as

$$I = A\left(\frac{T_N - T}{T_N}\right)^{2\beta} \tag{2.7}$$

where I is the diffraction intensity, A is an arbitrary scale factor, T_N is the critical

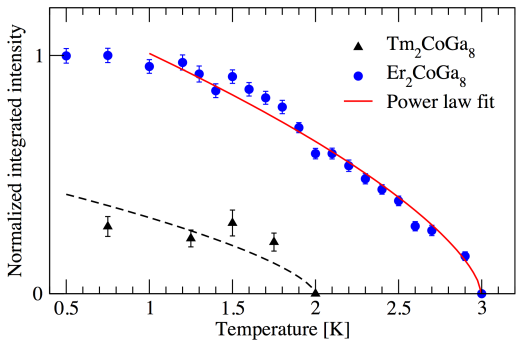

Figure 2.11: The temperature dependence of the integrated intensity of the (1, 0.5, 1) magnetic reflection of Er_2CoGa_8 ($d \simeq 3.56$ Å) and the (0.5, 0, 2.5) magnetic reflection of Tm_2CoGa_8 ($d \simeq 3.86$ Å), shown as blue circles and black triangles, respectively. A power law has been fitted to the Er_2CoGa_8 data (solid red line), giving a critical exponent of $\beta = 0.33 \pm 0.02$ and $T_N = 3.00 \pm 0.01$ K. The Tm_2CoGa_8 data was not of sufficient quality to obtain a reliable fit, however the transition at $T_N = 2$ K is clear. A scaled power law with the same exponent as that fitted to the Er_2CoGa_8 data is overlaid (broken black line).

Table 2.4: The β critical exponent of a selection of universality classes for the magnetisation order parameter [93].

	2D Ising	3D Ising	2D X-Y	3D X-Y	3D Heisenberg
β	0.125	0.326	-	0.345	0.367

temperature, and β is the critical exponent. According to the universality hypothesis the critical exponent is dependent upon the dimensionality of the order parameter and that of the system. Table 2.4 gives theoretically exact and experimentally determined critical exponents for a selection of universality classes. By fitting the power law to our experimental data, it was possible to predict the universality class and hence dimensionality of the system.

Figure 2.11 shows such a fit to the Er_2CoGa_8 data (the Tm_2CoGa_8 data is insufficient for fitting). We found a critical exponent of $\beta = 0.33 \pm 0.02$, which by

reference to Table 2.4, suggests that these compounds adopt either the 3D-Ising or the 3D-XY universality class. These classes represent 3-dimensional systems with either a 1-, or 2-dimensional order parameter, respectively. We note that the power law is only exact at the transition, and becomes less accurate upon decreasing temperature. For this reason we only fit the data less than 2 K below the transition.

In the refinement of the Er_2CoGa_8 magnetic structure, only data from bank 3 (average $2\theta = 90°$) of the WISH instrument was required to capture all magnetic reflections and give sufficiently high resolution. However, in the Tm_2CoGa_8 refinement it was necessary to include data measured on bank 2 (average $2\theta = 58.33°$), which captured the (0.5, 0, 0.5) magnetic reflection at $d \sim 7.8$ Å, outside the range of bank 3, shown in the inset to figure 2.10.

It was assumed that only the rare-earth ions are magnetic. The cobalt ions are expected to be non-magnetic due to an effective filling of the transition metal $3d$ states by an excess of gallium $4p$ electrons in the conduction band [80]. This is confirmed by the fact that Y_2CoGa_8 and Lu_2CoGa_8 are diamagnetic metals. Furthermore, the low transition temperatures are a signature of probable rare-earth ordering.

Despite having very similar crystal structures and common magnetic easy axes [20], the 300 mK diffraction patterns (Fig. 2.8 and 2.10) clearly show that the two samples have different magnetic propagation vectors. These were determined to be $\mathbf{q}$ = (0, 1/2, 0) and $\mathbf{q}$ = (1/2, 0, 1/2) for the erbium and thulium compositions, respectively. In tetragonal symmetry, the choice of the *a* and *b* axes is arbitrary when defining the propagation vectors. The important consideration is the direction of the magnetic moments in the *ab*-plane with respect to the propagation vector. Here, the *a* and *b* axes have been defined such that the magnetic moments lie parallel to the *b*-axis, as will become apparent later.

Representational analysis was performed using the BasIreps program, part of the FULLPROF suite [24], in order to determine the possible magnetic structures al-

lowed by the known symmetry and wave vectors of Er_2CoGa_8 and Tm_2CoGa_8. For both propagation vectors there exists the same eight one-dimensional irreducible representations (irreps). Six of these irreps are involved in the magnetic reducible representation of the $2g$ Wyckoff position of the $P4/mmm$ space group occupied by erbium or thulium. These correspond to magnetic moments lying parallel to the *a*(*b*) or *c* axes, with parallel and antiparallel alignment on the Er/Tm(1) and Er/Tm(2) sites.

Magnetic structure refinements corresponding to the six possible single-irrep models were performed for each sample. The magnetic and structural reliability factors (R_{Mag} and R_{Bragg}) and χ^2 for the refinements are given in Table 2.5. It is clear that for each sample only a single model successfully fits the data, as highlighted in bold in Table 2.5 and shown in figures 2.7 and 2.9. We note that for all Tm_2CoGa_8 models, the χ^2 values are similar. This is due to the magnetic reflections being weak compared to both the structural reflections and the background. However the R_{Mag} values, which are also large due to the weak magnetic reflections, clearly show the correct model. For both Er_2CoGa_8 and Tm_2CoGa_8, the fitted magnetic structures correspond to moment directions aligned parallel to the *b*-axis (with respect to our defined propagation vectors) and an AFM stacking along the *c*-axis of $(+-+-)$ and $(++--)$, respectively. In a magnetic resonant x-ray diffraction study on Ho_2CoGa_8 [79] it was not possible to determine whether the holmium moments stacked $(++--)$ or $(+--+)$ along the *c*-axis. Tm_2CoGa_8 also adopts a similar *c*-axis stacking, however our results are not ambiguous, and clearly show a single magnetic structure solution.

The magnitudes of the magnetic moments at 300 mK were refined to be 4.71(3) μ_{B}/Er and 2.35(4) μ_{B}/Tm, as given in Table 2.3. These values are in good agreement with those obtained from bulk magnetisation measurements. Our magnetometry data predicted rare-earth moments of 4.0 $\mu_{\mathrm{B}}/\mathrm{Er}$ and 3.7 $\mu_{\mathrm{B}}/\mathrm{Tm}$, and extrapolating

Table 2.5: Reliability factors of refinements of the six possible single-irrep magnetic structure models for both Er_2CoGa_8 and Tm_2CoGa_8.

Moment axis	*c*-axis stacking	R_{Mag}	R_{Bragg}	χ^2
	Er_2CoGa_8, $\mathbf{q}$ = (0, 1/2, 0)			
a	$(++++)$	67.5	11.7	43.4
a	$(+-+-)$	68.7	9.05	29.3
b	$(++++)$	75.7	11.0	42.4
b	$(+-+-)$	**14.7**	**7.29**	**8.91**
c	$(++++)$	83.6	11.7	44.3
c	$(+-+-)$	45.5	9.7	20.0
	Tm_2CoGa_8, $\mathbf{q}$ = (1/2, 0, 1/2)			
a	$(+--+)$	102.0	8.97	14.3
a	$(++--)$	54.4	7.5	12.1
b	$(+--+)$	114.3	9.1	14.4
b	$(++--)$	**21.4**	**6.9**	**10.3**
c	$(+--+)$	93.9	9.0	14.4
c	$(++--)$	50.8	7.7	12.5

the data measured by Joshi *et al.* [20] gives moments of $4.6\ \mu_{\mathrm{B}}/\mathrm{Er}$ and $2.90\ \mu_{\mathrm{B}}/\mathrm{Tm}$. Only the prediction for the thulium moment from our data is in rather poor agreement with the neutron refinement result. As discussed in section 2.5.1, this is due to an unexplainably high moment evident throughout the magnetisation measurement.

The rare-earth ion moments are found to be much smaller than their theoretical free-ion values of 9 μ_{B}/Er and 7 μ_{B}/Tm. As discussed, this is expected in such systems where the magnetic behaviour is dominated by crystal electric field (CEF) effects [81]. The ground state multiplet degeneracy of the R^{3+} ions is lifted by the CEF. The wave functions of the split energy levels, $|\psi_n\rangle$, were calculated from the CEF parameters found by Joshi *et al.*, [20] in terms of the basis states $|\mathrm{J},\ \mathrm{J_z}\rangle$, using the McPhase software package [96]. The zero-field ground states of both Er^{3+} (doublet) and Tm^{3+} (singlet) are non-magnetic. The state energies, shown in figures 2.12(a) and 2.12(b), and associated ion moments, shown in figures 2.12(c) and 2.12(d), were calculated as a function of internal magnetic field using the following equations.

$$\mathrm{E}_n = \mathrm{E}_0 + \mathrm{B}\mu_{\mathrm{B}}\mathrm{J_z} \tag{2.8}$$

where n denotes the state, E_0 is the zero-field energy of the n^{th} state, B is the internal magnetic field, and $\mathrm{J_z} = \langle\psi_n|\mathrm{J_z}|\psi_n\rangle$. The expectation value of $\mathrm{J_z}$ for the ion is given by

$$\langle\mathrm{J_z}\rangle = \frac{\sum_n \mathrm{J_z}\exp(\frac{-\mathrm{E}_n}{\mathrm{k_B}T})}{\sum_n \exp(\frac{-\mathrm{E}_n}{\mathrm{k_B}T})} \tag{2.9}$$

The ion magnetic moment is then equal to $-g_{\mathrm{J}}\langle\mathrm{J_z}\rangle\mu_{\mathrm{B}}$.

At 300 mK only the ground state is occupied. For Er^{3+}, the moment = $4.0\ \mu_{\mathrm{B}}$ in the field range 18 to 47 T, and for Tm^{3+}, the moment = $2.7\ \mu_{\mathrm{B}}$ in the field range 1.5 to 76 T. These values, clearly illustrating the reduction in moment due to the CEF, are close to those determined from neutron powder diffraction. The deviation from the empirically determined values is likely to be due to uncertainties in the

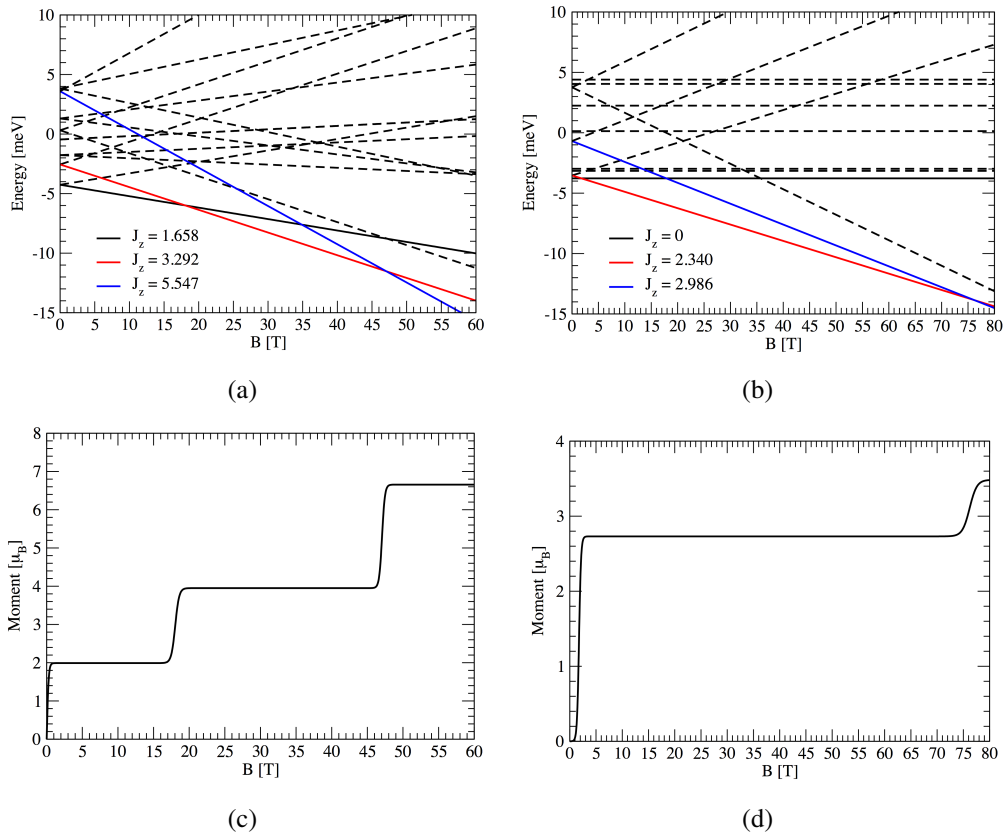

Figure 2.12: (a) and (b): The calculated CEF energy level splitting as a function of internal magnetic field for Er^{3+} and Tm^{3+}, respectively. (c) and (d): The magnetic moment of the ion at 300 mK, approximately corresponding to that of the ground state energy level given in a and b, as a function of internal magnetic field for Er^{3+} and Tm^{3+}, respectively.

CEF parameters, upon which the calculation is based. These calculations illustrate the significance of the internal magnetic field due to the local atomic environment present within such systems

In Er_2CoGa_8 magnetism propagates antiferromagnetically (AFM) along the *b*-axis in the direction of the moments, which ferromagnetically (FM) couple along the *a*-axis (figure 2.13). The *ab*-planes of rare-earth ions, containing the easy axis of magnetisation, are stacked AFM $(+ - +-)$ along the *c*-axis. By contrast, in Tm_2CoGa_8 the moments in the *ab*-plane align in an opposite fashion to Er_2CoGa_8

i.e. FM along the *b*-axis and AFM along the *a*-axis (figure 2.14). Furthermore, the planes are stacked alternately FM / AFM along the *c*-axis ($++--$).

As explained in section 2.2, the R_2CoGa_8 crystal structure can be thought of as a stacking of RGa_3 units, separated by $CoGa_2$ layers. In Ce_2RhIn_8 the common rare-earth magnetic structures of Ce_2RhIn_8 and $CeIn_3$ [69] suggests that the $RhIn_2$ layers have little influence on the magnetic structure, giving 2D characteristics. We note that this is not the case in the R_2CoGa_8 series. The simple collinear antiferromagnetic structures refined in this study do not reflect the more complicated magnetic structures of the RGa_3 (R = Er and Tm) compounds [78]. For example, the $TmGa_3$ magnetic structure is multi-axial, involving two or three propagation vectors. Indeed, the evaluation of the critical exponent predicts a magnetic structure that is 3-dimensional.

The spacings of the rare-earth ions (Table 2.3) are approximately 10 times greater than the typical radius of the localised, magnetically ordered rare-earth $4f$ states ($\sim$0.5 Å). There is insufficient overlap of wavefunctions for direct exchange (section 1.2) to occur. The dominant exchange interaction in these compounds is therefore the Ruderman-Kittel-Kasuya-Yosida (RKKY) interaction (section 1.2) that supports both FM and AFM exchange, dependent upon the inter-atomic distances. In competition with the RKKY exchange integral are the CEF terms of the Hamiltonian [81], as described in section 2.3. As a consequence, rare-earth inter-metallic systems may exhibit a wide variety of magnetic structures ranging from collinear FM [97] to spin glasses [98]. As both Er_2CoGa_8 and Tm_2CoGa_8 have similar inter-atomic distances between the rare-earth ions, we suggest that the difference in magnetic structures is due primarily to the CEF terms. These terms are clearly of great importance in these materials, as they have already been shown to account for the extreme magnetic anisotropy [20]. The magnetic structures refined for Er_2CoGa_8 and Tm_2CoGa_8 clearly give easy axes lying in the *ab*-plane. The CEF results in a

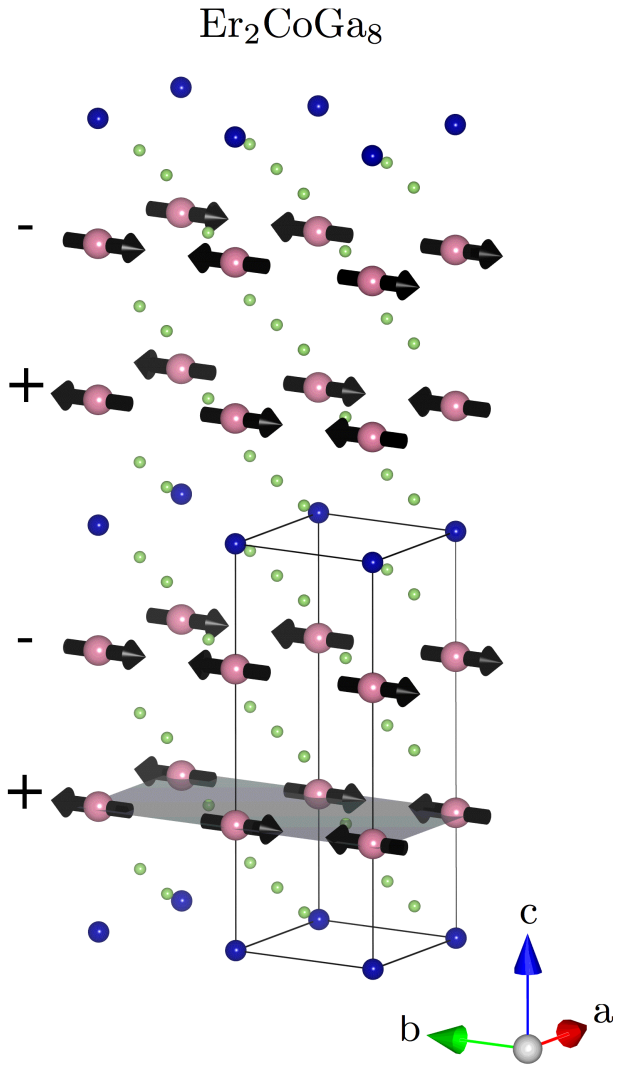

Figure 2.13: The crystal structure of Er_2CoGa_8 with the magnetic structure superimposed, represented by black arrows. Erbium, cobalt and galium ions are shown by pink, blue and green spheres of decreasing size, respectively. The $P4/mmm$ unit cell is drawn in black, and *ab*-planes of rare-earth ions are shaded grey.

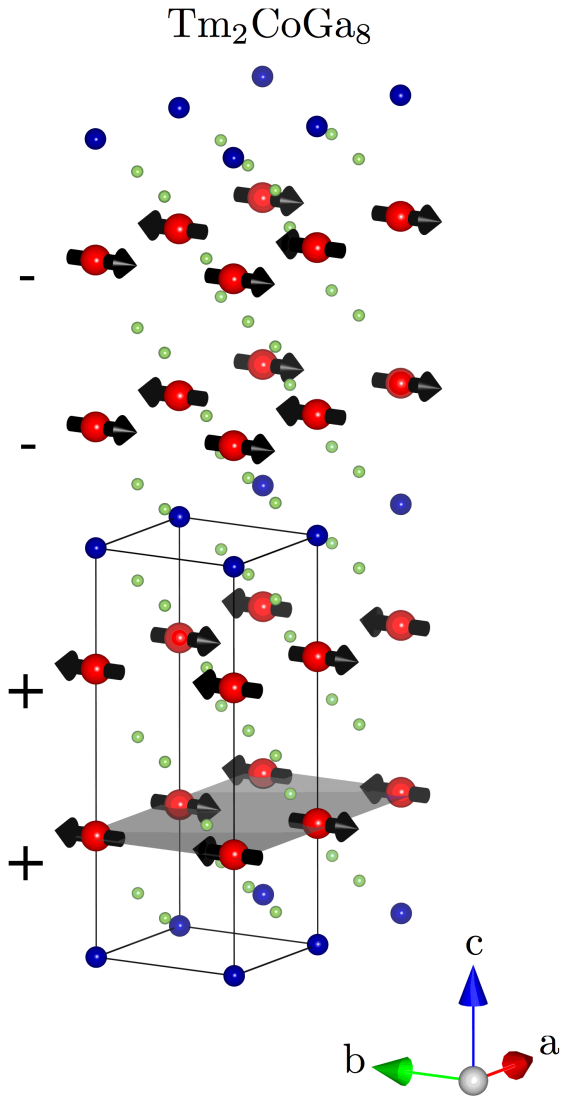

Figure 2.14: The crystal structure of Tm_2CoGa_8 with the magnetic structure superimposed, represented by black arrows. Thulium, cobalt and galium ions are shown by red, blue and green spheres of decreasing size, respectively. The $P4/mmm$ unit cell is drawn in black, and *ab*-planes of rare-earth ions are shaded grey.

higher susceptibility in the *ab*-plane, and the magnetic structure allows for a canting of moments in the same direction.

The in-plane and *c*-axis nearest-neighbour exchange constants for the R_2CoGa_8 series, determined by Joshi *et al.* [20] through CEF calculations, are given in Table 2.1. For Er_2CoGa_8 $\mathcal{J}_{ex}^{ab}/k_B = -0.35$ K and $\mathcal{J}_{ex}^{c}/k_B = -0.32$ K, and for Tm_2CoGa_8, $\mathcal{J}_{ex}^{ab}/k_B = -0.53$ K and $\mathcal{J}_{ex}^{c}/k_B = -0.075$ K.

In Er_2CoGa_8 $\mathcal{J}_{ex}^{c}$ is approximately equal to $\mathcal{J}_{ex}^{ab}$. Our results show that this scenario favours a $(+-+-)$ AFM stacking of planes, with an equivalent, anisotropic AFM coupling in the *ab*-plane, along the *b*-axis. By comparison, in Tm_2CoGa_8 $\mathcal{J}_{ex}^{c}$ is small compared to the large $\mathcal{J}_{ex}^{ab}$ value. The magnetic structure is therefore dominated by a strong, in-plane AFM coupling with a favoured $(++--)$ *c*-axis stacking. The magnetic structures refined in this study are therefore consistent with, and reinforce, the calculated CEF dependent exchange constants. Importantly, this shows that by choice of the rare-earth ion one can modify the CEF within the R_2CoGa_8 series in order to predetermine the magnetic structure.

2.6 Conclusions

In this chapter, we have presented a study of the magnetic structure of two, newly synthesised inter-metallic compounds, Er_2CoGa_8 and Tm_2CoGa_8. In both materials, the magnetic structure has been solved through the refinement of neutron powder diffraction. Rare-earth magnetic moments were found to lie parallel to the *b*-axis, with magnitudes 4.71(3) μ_B/Er and 2.35(4) μ_B/Tm. Despite having common easy axes of magnetization (in the *ab*-plane) the magnetic propagation vectors were found to be different; in Er_2CoGa_8 $\mathbf{q}$ = (0, 1/2, 0) and in Tm_2CoGa_8, $\mathbf{q}$ = (1/2, 0, 1/2). The different magnetic structures are due to a competition between crystal electric field effects and the RKKY exchange interaction. We have shown that the magnetic order parameter adopts either the 3D-Ising or 3D-XY universality

class, with transition temperatures of 3.0 K and 2.0 K, for the erbium and thulium compounds, respectively. Further, by comparison of the R_2CoGa_8 and RGa_3 magnetic structures, we suggest that the $CoGa_2$ layers play an important role in the 3D magnetism in this series, as opposed to inducing a quasi-2D magnetic structure as in Ce_2RhIn_8.

Chapter 3

Ion-specific magnetic structures in $TbMn_2O_5$ solved by resonant x-ray diffraction

3.1 Magneto-electric multiferroics

3.1.1 Introduction to multiferroics

Ferroic materials have been instrumental in modern, solid-state technology. For years data storage media has been based upon ferromagnetic materials in which a spontaneous magnetisation may be switched by an external magnetic field. Ferroelectric materials exhibit a spontaneous electric polarisation, which may be switched by an external electric field, and so are of great importance to the sensor industry. Furthermore, ferroelectrics often structurally distort (ferroelastic) upon changes in the electric polarisation that occur in response to the applied field, and as such are ideally suited to use as nanoscale actuators, sonar devices and medical imaging.

Figure 3.1 illustrates the three ferroic properties discussed above. The coloured

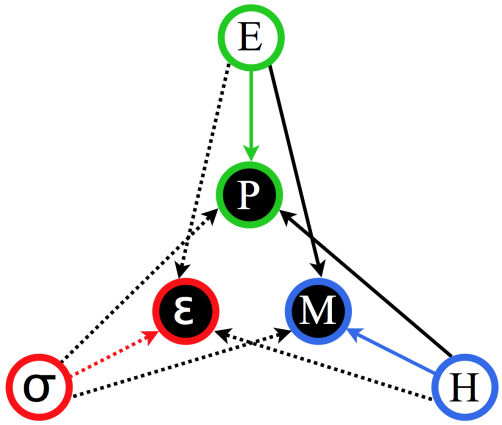

Figure 3.1: Diagram illustrating the ferroic order parameters, electric polarisation (**P**), magnetic polarisation (**M**), and strain (ε), and their associated external parameters, electric field (**E**), magnetic field (**H**), and stress (σ). These are linked by coloured arrows, respectively. The desired multiferroic coupling is indicated by black arrows. In particular, the magneto-electric effect, studied in detail in this thesis, relates to the solid arrows. The diagram is based upon figure 1 of reference 4.

arrows indicate the ferroic coupling paths between the external parameters, electric field (**E**), magnetic field (**H**) and stress (σ), and the respective material order parameters, polarisation (**P**), magnetisation (**M**) and strain (ε). The black arrows represent multiferroic coupling. The study of multiferroicity has been lead by the desire to combine ferroic properties in a single phase of a material, not only such that the material has a number of useful simultaneous electronic responses, but also to entwine the properties through a coupling mechanism such that new physical phenomena might be realised [3]. Indeed, since Maxwell derived his famous equations in 1865, it has been clear that one might expect magnetism and electricity to be closely coupled in the solid state. This coupling has been shown to occur in a small class of materials named magneto-electric multiferroics, some examples of which have been studied in detail in this thesis. With the possibility of 4-state memory devices and revolutionary developments in sensing applications, research

into these materials boomed [99]. Not only have magneto-electric memory effects and magnetic / electric switching already been demonstrated [4], new fundamental physics that provides a greater understanding of the quantum electronic behaviour of solids has been developed [40, 100–102].

The microscopic requirements of conventional ferroelectricity and magnetism makes the two mutually exclusive. In the classic ferroelectric perovskite $BaTiO_3$, electronic covalency between the oxygen ligand $2p$ and the titanium $3d$ states stabilises the ferroelectric displacement of the otherwise centred titanium ion. For this scenario to be energetically favourable, the titanium ion (or in general any oxygen coordinated transition metal ion) must have empty d states [3]. This is not compatible with magnetism, where for a net magnetic moment to occur on a given ion there must exist unpaired valence electrons. For this reason single-phase multiferroics rely upon a number of unconventional mechanisms for ferroelectricity, outlined in the following examples. In $BiMnO_3$ and $BiFeO_3$, stereochemical activity can give rise to a ferroelectric polarisation [103] where the non-bonded $6s$ bismuth electrons form lone pairs that have a high polarisability. In $YMnO_3$ a geometric mechanism results in a ferroelectric polarisation whereby rigid MnO_5 blocks tilt, hence causing a change in Y-O bond lengths. This results in two 'up' dipoles and one 'down' dipole (located at the Y-O bonds) per MnO_5; hence giving a net electric polarisation [104]. In $La_{0.6}Ca_{0.4}MnO_3$ and $Pr_{1-x}Ca_xMnO_3$, there exists a long-range ordering of manganese ions with average valencies +3 and +4, which takes the form of a superposition of site-centred and bond-centred charge ordering. This superposition gives rise to local dipole moments, and hence a ferroelectric polarisation [105]. Finally, there exists two additional mechanisms for ferroelectricity which are key to the study presented in this thesis. These involve the development of an electric polarisation as a direct consequence of a complex, frustrated magnetic order. The coupling results from either the antisymmetric spin-orbit interaction

of Dzyaloshinsky-Moriya (DM) exchange (section 1.2) or the exchange-striction mechanism. Key to these two mechanisms, described in detail later in this chapter, is that because the ferroelectricity originates in the magnetism the electric polarisation has a high sensitivity to externally applied magnetic fields despite a potentially weak magneto-electric coupling [40].

Due to the requirement of unconventional ferroelectricity, very few examples of single-phase multiferroic materials have been found that exhibit a significant magneto-electric coupling. However, through developments in crystal growth techniques, experimental methods, and the desire to find a theoretical microscopic explanation of the coupling mechanisms, a small but varied range of materials are available for study [4]. As shown above, a number of different mechanisms may lead to ferroelectric, and hence single-phase multiferroic behaviour in solid state materials. Two types of multiferroics are defined, accordingly. Type I compounds (or proper ferroelectrics) are those in which ferroelectricity and magnetism have different microscopic origins with different ordering temperatures (often $T_{\mathrm{FE}} > T_{\mathrm{C}}$), and as such are largely independent and extremely weakly coupled. In these systems the electric polarisation originates in stereochemical, charge ordered or geometric ferroelectricity. In type II multiferroics (improper ferroelectrics) the spontaneous electric polarisation occurs due to a complex lattice distortion or some other long-range order parameter. The magneto-electric coupling tends to be strong, however due to the improper nature of the ferroelectricity, the electric polarisation is often found to be weak [102]. The electric polarisation originates in either the antisymmetric DM interaction or the exchange-striction mechanism. This splits this type of multiferroic into two respective classes; those with spiral magnetic structures, for example $TbMnO_3$ [106], $Ni_3V_2O_8$ [107], and $MnWO_4$ [108], and those with collinear magnetic structures of which the most prominent members are the $R Mn_2O_5$ series [23].

3.1.2 Magneto-electric coupling in type II multiferroics

Due to their strong magneto-electric effects, we focus solely on type II multiferroics. In this section we describe in general the possible mechanisms for the respective magneto-electric coupling. The primary constraint on the coupling is that the symmetries of electric (**P**) and magnetic (**M**) polarisations are very different. **P** changes sign with spatial inversion and is time independent, whereas the opposite is true for **M**. Therefore, for static **P** and **M** a linear coupling is forbidden, allowing only the very weak, non-linear terms in the expansion of the free energy [101]. Linear coupling is possible only if the **P** and **M** vectors vary in both space and time [40]. Symmetry analysis provides a wealth of information on multiferroic behaviour, however it is beyond the theoretical scope of this thesis. We refer the reader to references 109, 110, and 111 for further details on symmetry.

In type II multiferroics, magnetic frustration is essential as it brings about a spatial variation in **M**. Frustration occurs when there is no possible spin configuration that can satisfy a number of competing exchange interactions and minimise the ground state energy. It is often prevalent in geometrically complex systems, particularly those with a number of magnetic ion species and hence distinct magnetic sub-lattices.

The first class of type II multiferroics are those with spiral magnetic order. The spirals often take the form of incommensurate cycloidal magnetic structures. The spiral breaks both time-reversal and spatial inversion symmetry, hence allowing a substantial linear magneto-electric coupling to develop. The magnetic exchange between the transition metal spins occurs indirectly *via* oxygen ligands and is described by the Dzyaloshinsky-Moriya (DM) exchange interaction, given in equation 1.4 [40, 112]. The DM vector, $\mathbf{D} \propto \mathbf{x} \times \mathbf{r}$, where $\mathbf{r}$ is a vector connecting the interacting ions (parallel to the propagation $\mathbf{q}$) and $\mathbf{x}$ is a vector describing a displacement of the mediating oxygen ion. As such, **D** is maximised, and hence the ground

state energy is minimised, when the oxygen ion is displaced perpendicular to the chain of magnetic ions. As $\mathbf{S_1} \times \mathbf{S_2}$ (from equation 1.4) is always in the same direction for a spiral (*i.e.* the axis of spin rotation $\mathbf{e}_3$), all oxygen ions are displaced in the same direction, orthogonal to both $\mathbf{q}$ and $\mathbf{e}_3$. This oxygen displacement results in a net dipole moment and hence the spontaneous electric polarisation. The geometry is illustrated in figure 3.2. It is now widely acknowledged that this mechanism is responsible for the magneto-electric behaviour in the *R*MnO_3 series [39, 113–116], on the condition that the radius of the rare-earth ion is sufficiently small to cause frustration, *e.g.* terbium or dysprosium [40]. In $TbMnO_3$, $\mathbf{q}$ is parallel to the *b*-axis, the cycloid rotates around the *a*-axis, and an electric polarisation parallel to *c* spontaneously develops simultaneously with the incommensurate cycloidal magnetic order [106].

We now focus on the second class in which the magneto-electric coupling may originate in collinear magnetic structures. It is possible for a spontaneous ferroelectric polarisation to occur when ionic sites of different charges are coupled through bonds of different lengths due to a frustrated magnetic structure; the exchange-striction model. The simplest model, shown in figure 3.3, is the axial next-nearest-neighbour Ising model (ANNNI) [100]. In this model we consider a chain of Ising spins with both nearest-neighbour (NN) and next-nearest-neighbour (NNN) exchange interactions. In this scenario the Ising model may be written as

$$H = J_1 \sum_i S_i^z S_{i+1}^z + J_2 \sum_i S_i^z S_{i+2}^z \tag{3.1}$$

If J_2, the NNN interaction, is at least half the magnitude of J_1 and positive (*i.e.* antiferromagnetic), a frustrated spin chain of $\uparrow\uparrow\downarrow\downarrow$ moments will result. If J_1 is negative, the frustration will be relieved by a shortening of $\uparrow\uparrow$ bonds and a lengthening of $\uparrow\downarrow$ bonds, as depicted in figure 3.3. The opposite is true for $J_1 > 0$. In this way spatial inversion symmetry is lost and a multiferroic state may arise.

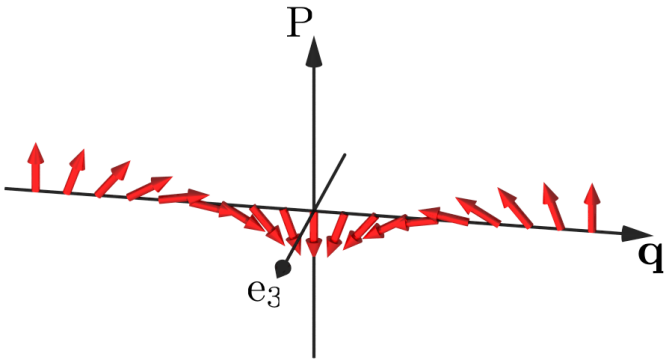

Figure 3.2: The electric polarisation induced by the Dzyaloshinsky-Moriya exchange interaction with respect to a magnetic cycloid, rotating about e_3, propagating along **q**.

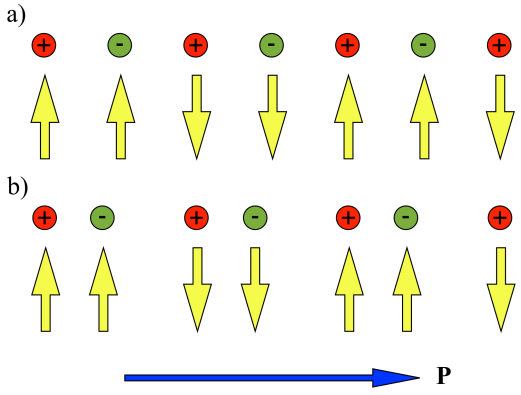

Figure 3.3: A possible magneto-electric mechanism for collinear magnetic structures. The axial next-nearest-neighbour Ising model is coupled with charge order, giving rise to an electric polarisation.

We note that despite the possibility of a strong dependence of the electric polarisation on applied magnetic fields, the inverse effect is not as likely. The spontaneous electric polarisation does not break time-reversal symmetry in the same way as the spatial inversion symmetry breaking of the frustrated magnetic structures. This technologically desirable coupling has therefore driven the search for further magneto-electric coupling mechanisms, in particular the consideration of magnetic and electric domains. In the remaining chapters of this thesis we study two members of the $R\mathrm{Mn_2O_5}$ series, $\mathrm{TbMn_2O_5}$ and $\mathrm{TmMn_2O_5}$, in which the behaviour of magneto-electric domains is considered to be key in explaining the extreme magneto-electric phenomena.

3.2 The $R\mathrm{Mn_2O_5}$ series

3.2.1 Multiferroic phenomena

Through the continual discovery of type II multiferroics, it is becoming apparent that the majority of magneto-electric effects observed are best described by the DM interaction, originating in cycloidal magnetic structures. The $R\mathrm{Mn_2O_5}$ series (R = rare-earth, Bi or Y) therefore remains an exception. This is because, despite the probable existence of a c-axis cycloid (see section 3.2.3), the strongest electric polarisation is found in the collinear, commensurate magnetic phase [117, 118]. The origin of the magneto-electric coupling in the $R\mathrm{Mn_2O_5}$ series has therefore been a subject of intense debate [117–125], particularly due to the range of exciting magneto-electric phenomena observed in its members.

$R\mathrm{Mn_2O_5}$ has been synthesised with all lanthanide elements (excluding cerium), and with yttrium, bismuth and lanthanum. Those composed of lanthanum and rare-earth ions lighter than, and including neodymium, are not ferroelectric, and so we omit them from the following discussion. In general the series develops three or four

low temperature, multiferroic phases, depending on whether or not the rare-earth ion is magnetic. Below $T_{\mathrm{ICM2}} \simeq 45$ K, a two dimensional incommensurate (ICM2) manganese magnetic structure forms with propagation vector $\mathbf{q} = (q_x,\ 0,\ q_z)$. At $T_{\mathrm{CM}} \simeq 35$ K, the magnetic propagation locks into a commensurate phase (CM) with $\mathbf{q} = (0.5,\ 0,\ 0.25)$, accompanied by the evolution of an electric polarisation parallel to the *b*-axis. Then unusually at $T_{\mathrm{ICM2}} \simeq 25$ K, there occurs a re-entry into a second incommensurate phase (ICM1) and a dramatic reduction in the electric polarisation. For those members with magnetic rare-earth ions (*i.e.* excluding Y, Bi or La) a final transition occurs at $T_{\mathrm{RE}} \simeq 10$ K into the LT-ICM phase, marking the onset of spontaneous rare-earth ordering. We note that even above T_{RE} the rare-earth ions are found to be spin polarised with a propagation vector in common with the manganese magnetic structure due to an interaction between the rare-earth $4f$ electrons and the manganese dipole field [126, 127]. There are three exceptions to the above general phase diagram. Firstly, the Y, Er, and Tm members additionally exhibit a coexisting 1D-ICM and CM phase over a narrow temperature range between the ICM2 and CM phase. This magnetic phase is also weakly ferroelectric. Secondly, $DyMn_2O_5$ is commensurate below T_{RE} with $\mathbf{q} = (0.5,\ 0,\ 0)$ [128], and thirdly $BiMn_2O_5$ only exists in a single CM, ferroelectric phase with $\mathbf{q} = (0.5,\ 0,\ 0.5)$ [129, 130].

The properties of the $R Mn_2O_5$ series are highly dependent upon the choice of rare-earth ion. Heat capacity measurements showed a clear dependence of the above transition temperatures [23]. As the radius of the rare-earth ion decreases, both magnetic and ferroelectric transition temperatures monotonically increase due to changes in the crystal structure [23], as discussed in the following section. The value of q_x always remains approximately or exactly 0.5 in the ICM and CM phases, respectively; regardless of the choice of rare-earth ion. However, a significant variation in q_z has been observed across the series ranging from 0 to 0.5. This is a

result of the different magnetic interactions of the rare-earth ions with the surrounding crystal, for example differing single-ion anisotropies, f-d interaction strengths, and ionic radii [117]. The temperature dependence of the electric polarisation also varies dramatically across the series; summarised in figure 3.4. The above magnetic effects give rise to the diverse range of magneto-electric phenomena, the most important of which are summarised as follows.

YMn_2O_5 is arguably one of the simplest members of the RMn_2O_5 series as it has no magnetic rare-earth ions. Despite this, it still exhibits a wealth of multiferroic properties. It has been reported that in the ICM1 phase, an applied pressure of 10 kbar can reverse the electric polarisation and return the system to the CM phase [131]. This provides very strong evidence for the importance of lattice strain and hence supports the exchange-striction mechanism. Indeed, the electric polarisation that occurs simultaneously with the CM phase [132] has been predicted based upon a model involving simple magneto-elastic coupling to the crystal lattice [119]. However, there is strong evidence from the refinement of single-crystal neutron diffraction data that a cycloidal magnetic structure exists, propagating parallel to the *c*-axis [120, 130], hence allowing the antisymmetric DM interaction. The exact nature of the magneto-electric coupling mechanism therefore remains uncertain. Also, it was shown that by cooling YMn_2O_5 in applied electric fields one can switch the preferential occupation of different magnetic domains [121], as explained in section 3.2.3. By considering these domains, one can explain the electric polarisation reversal that was observed upon the CM / ICM1 phase transition [121]. In the ICM1 phase of $HoMn_2O_5$ a magnetic field > 11 T applied parallel to the *b*-axis returns the system to the CM phase, hence reinstating the *b*-axis electric polarisation [118, 133]. Interestingly the opposite is true for $ErMn_2O_5$ in which a low magnetic field applied parallel to the *c*-axis or a high magnetic field applied parallel to the *a*-axis suppresses the ferroelectricity [118, 123].

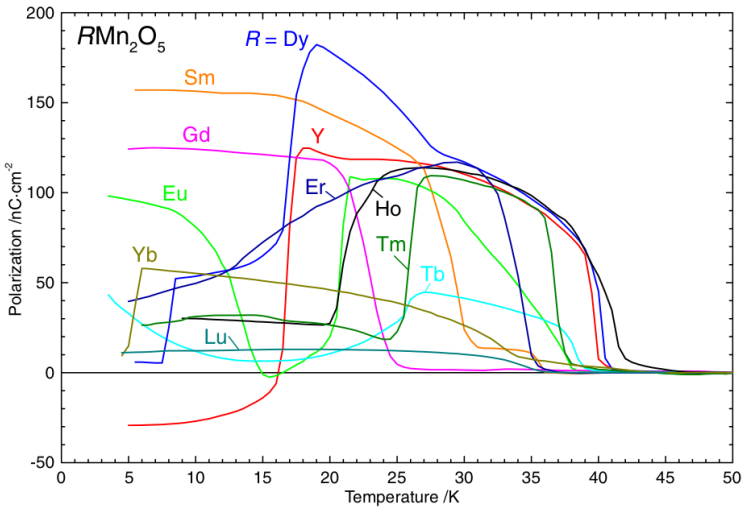

Figure 3.4: The temperature dependence of the electric polarisation for selected members of the $R Mn_2O_5$ series. The figure is reproduced from reference 134, published in the Journal of the Physical Society of Japan.

$TbMn_2O_5$ and $TmMn_2O_5$ are arguably the most important members of the series as the magneto-electric effects observed are technologically desirable. In $TbMn_2O_5$ a repeatable polarisation flip was measured by applying a 2 T magnetic field parallel to the *a*-axis, below T_{RE} [135]. In $TmMn_2O_5$, a polarisation flop was observed (rotation by 90° from along the *b*-axis to along the *a*-axis) on cooling through T_{RE} [136]. This is one of only two cases (the other being $YbMn_2O_5$) of an electric polarisation measured parallel to the *a*-axis in the $R Mn_2O_5$ series. It is a surprising result as the point group symmetry of the multiferroic phases is widely accepted to be *m2m*, hence only allowing a polarisation parallel to the *b*-axis [117]. An unprecedented structural change must therefore occur at this thermally induced transition. Furthermore, a 0.5 T magnetic field applied parallel to the *c*-axis returns the electric polarisation to the *b*-axis [137]. The magneto-electric coupling in the CM phase of $TmMn_2O_5$ is investigated in Chapter 5, and we report studies of $TbMn_2O_5$ in the remainder of this chapter, and in Chapters 4 and 6.

There are four important observations regarding the variety of magneto-electric phenomena and the series as a whole. Firstly, the CM phase uniformly exhibits the largest net electric polarisation, however the magneto-electric effects described above are only observed in the ICM1 / LT-ICM phases. The commensurability of the magnetic structure therefore plays a key role. Secondly, the two extreme effects of the thulium and terbium compounds would appear to be closely coupled to the spontaneous magnetic ordering of the rare-earth sub-lattice, hence consigning these effects to low temperatures. Thirdly, the above compounds (R = Y, Ho, Er, Tb and Tm) all have the same crystal structure and very similar Mn^{3+} and Mn^{4+} magnetic structures (described in section 3.2.3) [117]. Indeed, in the CM phase at 30 K, where the magnetism is dominated by the manganese ions, the behaviour of the electric polarisation is common to all five compounds [134]. Clearly the variety of magneto-electric phenomena across the series is due to the influence of the rare-earth ions that becomes significant at lower temperatures. This is particularly apparent in the case of YMn_2O_5, where no magnetic field induced, magneto-electric effects are apparent in applied fields less than 20 T [138]. Finally, stressing the importance of the rare-earth ion magnetism, the magnetic field induced effects occur when the field is applied parallel to the rare-earth ion easy axis of magnetisation (except in $DyMn_2O_5$).

3.2.2 Crystal structure and magnetic exchange

At room temperature the RMn_2O_5 series adopts the orthorhombic space group *Pbam*. In the low temperature multiferroic phases the *b*-axis inversion symmetry is lost and the crystal symmetry reduces, probably to $Pb2_1m$. The crystal structure is best described by considering *ab*-planes and a *c*-axis stacking, as shown in figure 3.5. Mn^{4+} ions are located within octahedral oxygen coordinations (dark green in figure 3.5) that form infinite edge sharing chains along the *c*-axis. These chains are linked

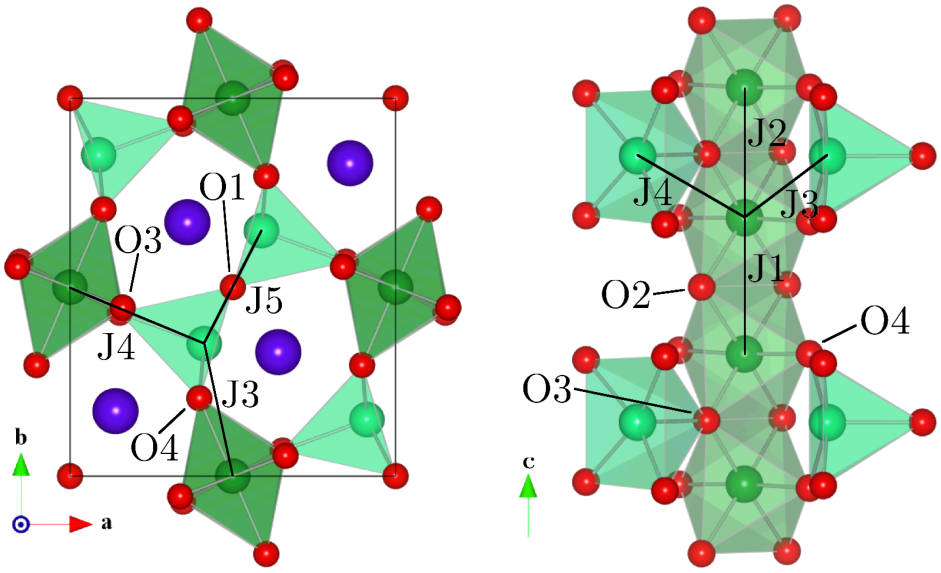

(a) *ab*-plane (b) *c*-axis stacking

Figure 3.5: The crystal structure of the RMn_2O_5 series. Mn^{4+} ions are located at the centre of octahedral oxygen coordinations (dark green), and Mn^{3+} ions are located close to the base of square-based pyramid coordinations (light green). Rare-earth and oxygen ions are shown as purple and red spheres, respectively. Note that the rare-earth ions have been omitted from (b) for clarity. They are coplanar with the O2 ions. Superimposed are the five manganese exchange interactions, J1-J5 and the mediating oxygen ions O1-O4.

in the *ab*-plane by corner sharing Mn^{3+} ion square-based pyramids. The corner sharing occurs through both basal and apical oxygen ions. The Mn^{3+} pyramids are themselves linked through a base edge. In the *c*-axis direction the interconnecting Mn^{3+} pyramids form layers that interweave layers of rare-earth ions coplanar with the O2 oxygen ions (omitted from figure 3.5b for clarity).

Such a complex structure results in five manganese magnetic exchange interactions, the competition of which gives rise to the frustrated magnetic structures described in the following section. In compounds with magnetic rare-earth ions the complete model becomes vastly more complex; for now we only consider the manganese magnetism. The exchange interactions, J1 to J5, and the mediating oxygen

ions, O1 to O4, are shown in figure 3.5. The labelling system used is that adopted in reference 38 and is common throughout the literature.

J1 to J5 are all super exchange interactions with the possibility of an additional direct exchange component to J1, J2 and J5. The sign of the exchange integral for J3 and J4 is determined by the Mn^{4+}-O3-Mn^{3+} bond angle, which is close to the critical angle between FM and AFM [38]. Figure 3.5b shows that J3 and J4 are in competition with J2 via the O3 oxygen ions. Regardless of the sign of J3 or J4, this competition will always force J2 to be FM. The sign of J1 is determined by the radius of the rare-earth ions which are coplanar with the mediating O2 oxygen ion. This gives rise to a number of possible stacking patterns of magnetic moments along the *c*-axis [117], and is discussed in the following section. In the *ab*-plane the next-nearest neighbour interaction along the *a*-axis (J4, J5) is stronger than that along the *b*-axis (J3, J5). This results in zig-zag AFM chains parallel to the *a*-axis mediated by $J4 > 0$ and $J5 > 0$. J3 is then close to zero, and alternates between FM and AFM, linking the AFM chains [38].

Following the structural determination of Sm, Eu, Gd, Tb, Dy and Y compounds, analysis of bond angles showed that on decreasing rare-earth radius, the AFM exchange interactions J1, J4 and J5 are strengthened and the J2 interaction is weakened [23]. The frustration resulting from the competition of J3/J4 and J2 is therefore relieved, hence explaining the increase in magnetic transition temperatures on decreasing rare-earth radius, reported in section 3.2.1.

3.2.3 Magnetic structures and domains

We split our discussion of the magnetic structures into approximately collinear magnetic *ab*-planes and their coupling along the *c*-axis. All RMn_2O_5 compounds with a strong FE/CM phase have a common *ab*-plane manganese magnetic structure that differs only slightly in moment angles across the series [117, 118, 130]. Figure 3.6

shows the structure of YMn_2O_5 as an example [130]. One factor that dictates the direction of the manganese magnetic moments is the magnetic anisotropy of the Mn^{3+} ions. Due to the crystal field splitting of the square-based pyramid coordination, a spin direction along the axis of the pyramid is favoured [117], *i.e.*, approximately 15° from the *a*-axis.

The wave vector star of the commensurate magnetic structure is essentially a single **q** domain, as **q** = (0.5, 0, 0.25) and -**q** map onto **q** = (0.5, 0, -0.25) and **q** = (-0.5, 0, 0.25) *via* a reciprocal space vector [130]. However, one must also account for orientational symmetries that are lost for the magnetic phase but present in the paramagnetic phase. Symmetry analysis performed in reference 130 shows that magnetic domains may exist that are related by inversion symmetry. Figures 3.6(a) and 3.6(b) illustrate both possible *ab*-plane configurations (labelled I and II). The AFM zig-zag chains running parallel to the *a*-axis are clear. One can also think of the difference between the two domains as being a shift of a zig-zag chain by one unit cell in the *a* direction with respect to its neighbours (as shown in red and blue in figure 3.6). An important consequence of the inversion related domains is that the electric polarisation will be in opposite directions, respectively.

There are three distinct magnetic sub-lattices in the plane; Mn^{3+}, Mn^{4+}, and R^{3+} (when magnetic). These sub-lattices are best thought of as spin density waves (SDW) propagating through the crystal where both manganese SDW's are in phase, and the rare-earth SDW has a relative $\pi/4$ phase shift. It is also important to consider the relative phase of the two zig-zag chains, as a phase difference (or slipping) between the two would result in the incommensurate magnetic structures [117].

The *c*-axis stacking is dependent upon the sign of J1 and J2. As described previously, J2 is always FM due to competition with J3 and J4. If J1 is always FM then the *c*-axis stacking is FM $(++\,++)$ and **q**=(0.5, 0, 0); this is the case for $DyMn_2O_5$. If J1 is always AFM, then the stacking is AFM $(+-\,+-)$ and

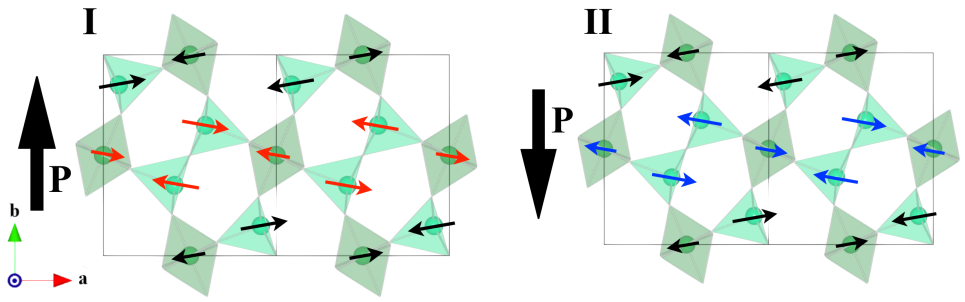

(a) (b)

Figure 3.6: The manganese magnetic structure of the RMn$_2$O$_5$ series (using YMn$_2$O$_5$ as an example). (a) and (b) show the two possible *ab*-plane structures that are related by inversion symmetry, respectively. The electric polarisation is marked by the black arrow. The *a*-axis zig-zag chains are differentiated by the red and blue coloured arrows. The figure has been redrawn from reference 121.

q=(0.5, 0, 0.5), as in BiMn$_2$O$_5$. In the other ferroelectric members of the series J1 is close to zero and alternates between FM and AFM. This gives rise to a $++--$ *c*-axis stacking and **q**=(0.5, 0, 0.25), as in the anisotropic next nearest neighbour Ising (ANNNI) model. The rare-earth ions are situated in between these planes. Hence, if the plane either side is AFM coupled, the rare-earth ion will experience a zero net dipole field. As a consequence, in compounds with $++--$ *c*-axis stacking only every other layer of rare-earth ions will be spin polarised above T_{RE}.

Only recently has it been possible to grow large enough single crystals for neutron diffraction. As a consequence earlier powder diffraction data has been surpassed, revealing a small *c*-axis magnetic moment component [73, 120, 121, 124, 130]. It is now widely accepted that this adopts the form of a flat cycloidal magnetic structure propagating parallel to the *c*-axis (except FM DyMn$_2$O$_5$) [73, 121, 124, 130], which is described by a phase difference between S_x, S_y, and S_z spin components of 0, π and $\pm\pi/2$, respectively [124]. The cycloidal rotation axis is given by the cross-product between the moment direction in the *ab*-plane (approximately 15° from the *a*-axis) and the direction of propagation (*c*-axis). In the *ac*-plane, neigh-

bouring cycloids rotate with opposite chirality, whereas in the *bc*-plane they rotate in the same direction [130]. The *bc*-plane magnetic structures of YMn_2O_5 (again there are two related by inversion symmetry as in the *ab*-plane) are shown in figure 3.7.

In the commensurate phase of the $R Mn_2O_5$ series four magnetic domains may exist. These originate in the admixture of *ab*-plane and *bc*-plane magnetic structures presented in figures 3.6 and 3.7, respectively. Explicitly, these are structures I+III, II+IV, I+IV, and II+III. Domains I+III and II+IV are related by inversion symmetry and are therefore indistinguishable by diffraction, with the same true for domains I+IV and II+III [117]. Although the occupation of all domains is possible, neutron diffraction results showed that the occupation of domains I+III, II+IV is clearly favoured in the commensurate phases of the $R Mn_2O_5$ series [121].

Before describing the possible magneto-electric coupling mechanisms active in the $R Mn_2O_5$ series, we first note a consequence of the inversion symmetry relation between domains. For the AFM zig-zag chain at the edge of the unit cell, the inversion leaves the S_x and S_y magnetic moment components unchanged, but reverses the S_z component. The opposite is true for the zig-zag chain running through the centre of the unit cell, for which the S_z component remains unchanged upon inversion, but the S_x and S_y components reverse.

3.2.4 Magneto-electric coupling

The exchange-striction model for the $R Mn_2O_5$ series in the *ab*-plane is analogous to the ANNNI interaction (section 3.1.2). The charge order in the $R Mn_2O_5$ series is realised through the existence of both Mn^{3+} and Mn^{4+} ions. As described above, the ions are located on crystallographically inequivalent sites and so the series is not truly charge ordered, however in the following mechanism the charge order is effective. Looking down the *c*-axis at the *ab*-plane there are distinct loops of five

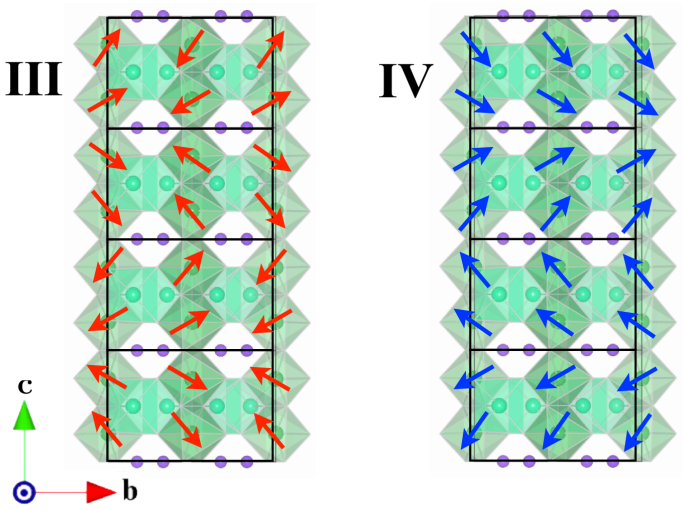

Figure 3.7: The *bc*-plane manganese magnetic structure of the RMn_2O_5 series (using YMn_2O_5 as an example). (a) and (b) show the two possible structures that are related by inversion symmetry, respectively. The figure has been reproduced from reference 121

manganese spins; Mn^{4+}-Mn^{3+}-Mn^{3+}-Mn^{4+}-Mn^{3+}. The associated super-exchange interactions, J4-J5-J3-J4-J3, cannot be satisfied, resulting in magnetic frustration. Half the moments align parallel, and half antiparallel. In accordance with the exchange interactions, it is energetically favourable for the antiparallel spins to lie closer together, and for the parallel spins to move apart. In this way the J3 interactions are no longer equivalent and the frustration is satisfied. There occurs a displacement of Mn^{3+} ions, breaking inversion symmetry, and resulting in a net electric polarisation along the *b*-axis. We note that the magnetic energy gain in satisfying the frustration is linear, whereas the energy loss due to the structural distortion is quadratic [117]. Hence, any such displacements will be small. Energy calculations on $TbMn_2O_5$ showed that the system is energetically stable when the J3 interactions are split through a lowering of symmetry to $Pb2_1m$ [139]. Furthermore, as J3 became weaker compared to J4, the CM phase became more stable and

the ICM phase was reduced. Compared to the weak DM interaction, this mechanism is based upon the Heisenberg model (see section 1.2); a stronger interaction that potentially results in a much larger electric polarisation [40].

The above exchange-striction model has the following consequences for the *R*Mn_2O_5 series. We only need to consider the magnetic structure in the *ab*-plane in which non-collinearity is not essential. As such the S_z spin component is irrelevant. The key exchange interaction in the magnetic frustration is J3, which is highly dependent upon the phasing between the AFM zig-zag chains. In the CM phase, the zig-zag chains are in-phase and so the J3's are identical. The magnetism is therefore frustrated, resulting in the distortion, and hence the electric polarisation. In the ICM phase, the phase between the zig-zag chains slips, making the J3's inequivalent, hence relieving the frustration; a possible explanation for the sudden loss of electric polarisation [117]. The importance of the J3 interaction was made clear in *ab-initio* calculations, which successfully predicted the phase diagram of the *R*Mn_2O_5 series using $\mathbf{P} \propto \langle \mathbf{S_3} \cdot \mathbf{S_4} \rangle$, where $\mathbf{S_3}$ and $\mathbf{S_4}$ are the spins of the Mn^{3+} and Mn^{4+} ions coupled via J3 [125].

In contrast to the exchange-striction model, the cycloidal magnetic structure propagating parallel to the *c*-axis can also result in an electric polarisation parallel to the *b*-axis via the DM interaction, described in section 3.1.2. However, there are a number of observations that are not predicted by this magneto-electric coupling. Firstly, the DM interaction does not give rise to a structural distortion parallel to the *c*-axis, as measured in synchrotron x-ray diffraction experiments [124]. Secondly, the electric polarisation is expected to be proportional to S_z. $BiMn_2O_5$, YMn_2O_5, and $HoMn_2O_5$ have approximately equivalent magnitudes of electric polarisation, however S_z in $BiMn_2O_5$ is much smaller than in the other two compounds [130]. Finally, the cycloidal magnetic structures could simply be the result of the loss of inversion symmetry due to exchange-striction coupling.

It has been proposed that the RMn$_2$O$_5$ series is in fact ferrielectric, as opposed to ferroelectric [118, 137]. In this scenario, the commensurate phase supports an antiferroelectric component of electric polarisation parallel to the *a*-axis, and a ferroelectric component parallel to the *b*-axis; resulting in a reduced, net polarisation parallel to the *b*-axis. In favour of the cycloidal model of magneto-electric coupling is the provision of an elegant description of the ferrielectricity. As described in section 3.2.3, the cycloids rotate in-phase in the *bc*-plane, and out of phase in the *ac*-plane. According to the DM interaction, this would result in the ferrielectricity observed [118]. Furthermore, the electric polarisation flop exhibited by $TmMn_2O_5$ could be a consequence of a chirality reversal of a cycloid, such that the spin rotations are in-phase in the *ac*-plane, and out of phase in the *bc*-plane [118, 137]. Indeed, calculations have shown that it is necessary to include the DM interaction to properly describe the magnetic phase diagram [117]. However, as it is dependent upon the spin-orbit interaction, it can be assumed to be weak compared to the exchange-striction coupling.

We return to the possible magnetic domains described in section 3.2.3. Regardless of the origin of the electric polarisation, switching between domains with structures I and II (exchange-striction) or III and IV (DM interaction) will reverse the electric polarisation. Furthermore, a 50/50 occupation of two domains related by inversion symmetry will result in a zero net polarisation. In YMn_2O_5, an applied electric field was shown to switch a 100% occupation of domains with structures I and II [121]; further evidence that the *ab*-plane magnetic structure, and hence exchange-striction mechanism, is dominant.

A comprehensive study of electromagnons in the RMn$_2$O$_5$ series also strongly supports the exchange-striction model, even in the ICM1 phase [122, 140]. The magneto-electric interactions that give rise to the electric polarisation also couple magnetic oscillations (magnons) to polar lattice vibrations, giving rise to the pos-

sible excitation of particles named electromagnons. The electromagnon excitations were only observed in the low temperature ICM1 phase and give rise to the step like function in the dielectric constant, which is evident at the CM/ICM1 phase transition of the ferroelectric RMn$_2$O$_5$ members (except Bi which has no ICM phase) [122]. The electromagnon excitation has a dependence on the polarisation of the incident photon, which originates in the symmetry of the magneto-electric coupling. This study showed that only symmetric magneto-electric coupling gave rise to the measured electromagnons, evidence for the exchange-striction mechanism taking effect in the ICM1 phase [122, 140].

The exact mechanism responsible for the magneto-electric effects of the RMn$_2$O$_5$ series therefore remains largely unknown. It is likely that both exchange-striction and DM coupling coexist and are strongly coupled. The two would then take effect with varying prominence throughout the multiferroic phase diagram (for example that proposed for $YbMn_2O_5$, $TmMn_2O_5$ and YMn_2O_5 shown in figure 3.8 [134]), giving rise to the rich and varied magneto-electric phenomena [117, 118].

3.3 $TbMn_2O_5$

Measurements of bulk the magnetisation, shown in figure 3.9(a), and dielectric constant, shown in figure 3.9(b), indicated that $TbMn_2O_5$ exhibits a number of multiferroic phases at low temperatures, in common with the other members of the RMn$_2$O$_5$ series [135] (the magnetic phase diagram has been determined through neutron diffraction and is described in detail later). A large magnetic anisotropy was evident, giving an easy direction of magnetisation parallel to the a-axis that saturates at approximately 2 T with a moment of 8.2 μ_{B} per terbium ion (close to the expected paramagnetic moment of 9.73 μ_{B}/Tb) [135, 141]. The observation of multiferroic behaviour prompted further investigation, which lead to the discovery of a highly reproducible electric polarisation reversal under applied magnetic fields

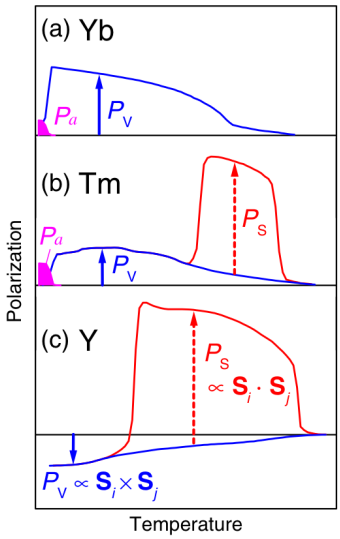

Figure 3.8: The polarisation components expected for (a) $YbMn_2O_5$, (b) $TmMn_2O_5$ and (c) YMn_2O_5. The broken and solid arrows indicate the polarisation components along the *b*-axis by the $\mathbf{S_1} \cdot \mathbf{S_2}$ exchange-striction and $\mathbf{S_1} \times \mathbf{S_2}$ DM couplings, respectively. The *a*-axis polarisation measured in the Yb and Tm compounds are shown. The figure is reproduced from reference 134, published in the Journal of the Physical Society of Japan.

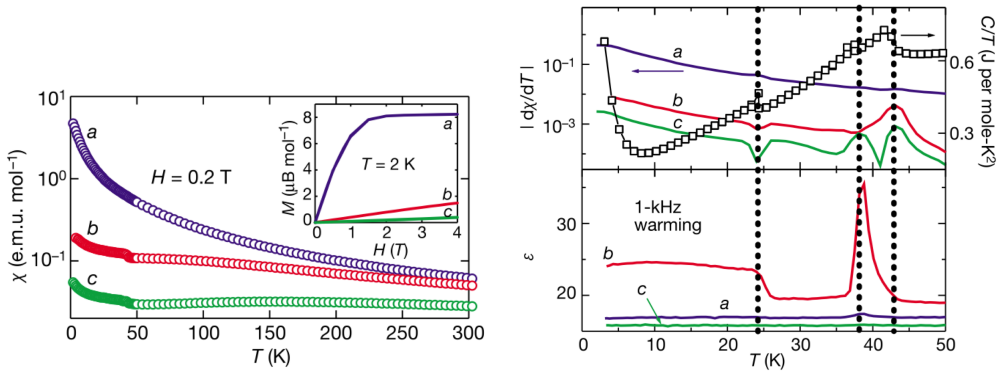

(a) (b)

Figure 3.9: (a) The magnetic susceptibility of $TbMn_2O_5$ measured along the three principle axes as a function of temperature. The inset shows the isothermal magnetisation at 2 K. (b) The differential magnetic susceptibility, heat capacity and dielectric constant measured as a function of temperature, indicating the multiferroic phases of $TbMn_2O_5$. Both figures are reproduced from reference 135.

of 2 T at 3 K, and the ability to imprint a permanent electric polarisation [135].

Figure 3.10(a) clearly illustrates the large polarisation reversal of approximately 80 nC cm^{-1}. Given that the polarisation flip occurs at the same applied magnetic field as the saturation of the terbium magnetic structure, it is believed that the rare-earth ions play a key role in this electronic behaviour. It is likely that the rare-earth ions break the magnetic time-reversal symmetry, and hence allow a large linear magneto-electric coupling [38, 135, 141]. By comparison the phenomenology behind the permanent polarisation imprint is more complex. Figure 3.10(b) shows the electric polarisation measured as a function of temperature after four different cooling conditions. The two solid lines show the electric polarisation having magnetically zero field cooled (ZFC) the sample under a poling electric field parallel to the $\pm b$-axes, respectively. The dashed line shows the polarisation after field cooling (FC) in 9 T with the poling field along the $+b$-axis, and the dotted line shows the effect of ZFC with a $+b$ poling field, then applying a 9 T magnetic field at 3 K which is removed only after turning off the poling field. The behaviour of the elec-

tric polarisation is most simply described by assuming two polarisations, P_1 and P_2, that are always antiparallel along the *b*-axis. Upon cooling through the multiferroic phases, the poling electric field determines the direction of P_1, which is relatively insensitive to applied magnetic fields. P_2 then aligns opposite to P_1 and is very sensitive to the applied magnetic fields, giving rise to the polarisation reversal. The permanent polarisation imprint can be explained as follows. The 9 T field applied at 3 K promotes P_2, which is set in the +*b* direction by the poling field. As the poling field is removed before the magnetic field, P_2 remains in this direction, forcing P_1 in the -*b* direction. Upon removing the magnetic field, the sample is then polarised (P_1) in the opposite direction to the applied poling field, hence leaving a negative polarisation imprint [135]. The existence of two contributions to the electric polarisation in $TbMn_2O_5$, and a probable third component below the spontaneous rare-earth ordering temperature, was shown by an optical second harmonic generation study (ideally suited to the study of non-centrosymmetric polar systems) [142]. We must note that despite this elegant description of the electronic behaviour, the exact microscopic mechanisms behind P_1 and P_2, and hence the magneto-electric coupling, remains in dispute [38, 121, 139, 143].

As discussed in section 3.2, the exchange-striction model is a likely candidate for the magneto-electric coupling in the RMn_2O_5 series. A neutron powder diffraction study of the $TbMn_2O_5$ crystal structure, which was in good agreement with that previously reported [144], found no direct evidence for small ionic displacements or the predicted lowering of symmetry to a polar space group [38, 139]. The same study did, however, provide some indirect evidence in the lattice parameters and the atomic displacement parameters, shown in figure 3.11. A significant step was observed in the *b* lattice parameter at the ferroelectric ordering temperature, indicating a substantial structural distortion in this direction. This was also accompanied by a small step in the *a* lattice parameter, whilst the *c* lattice parameter temperature

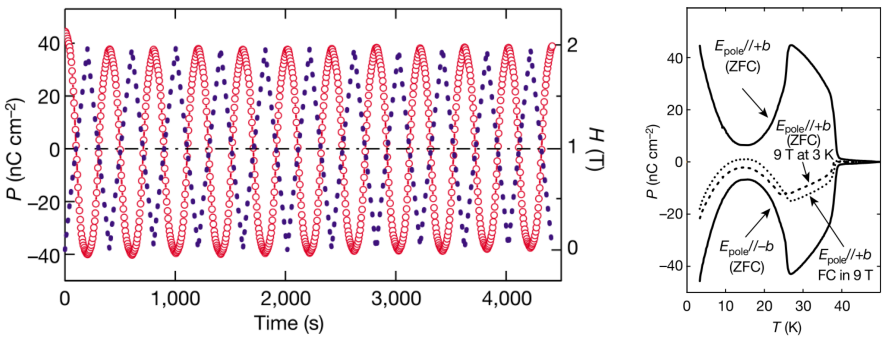

(a) (b)

Figure 3.10: (a) The electric polarisation (red circles) measured as a function of an applied magnetic field oscillating between 0 and 2 T (purple dots), showing the reproducable polarisation flipping at 3 K. (b) The electric polarisation measured under four different cooling conditions (see text for details) showing the permanent polarisation imprint. Both figures are reproduced from reference 135.

dependence remained featureless. Furthermore, a comparison of selected atomic displacement parameters indicated a significant displacement of the Mn^{3+} ions.

A number of neutron diffraction studies have determined the magnetic phase diagram of $TbMn_2O_5$ which is summarised as follows [38, 139, 145]. The manganese sub-lattices (Mn^{3+} and Mn^{4+}) of $TbMn_2O_5$ are found to exist in incommensurate (ICM) and commensurate (CM) magnetic phases at low temperatures, in which for both cases the manganese ion moments align in the *ab*-plane forming two spin density waves with wave vector $(\delta, 0, \tau)$. Along the *c*-axis these moments alternate with ferromagnetic and antiferromagnetic layers $(++--)$ [139], giving alternating layers of spin polarised terbium ions. One would also expect a small modulation of the terbium and O2 oxygen positions, which was indeed evident in the refined atomic displacement parameters [139]. The ferroelectric and magnetic phase diagram is shown in figure 3.12. At $T_{\mathrm{ICM2}} = 43$ K, the system enters an incommensurate phase (ICM2) in which manganese ions order antiferromagnetically with $\delta \simeq 0.5$ and $\tau \simeq 0.3$ [38]. Slightly lower in temperature, $T_{\mathrm{FE}} = 38$ K marks the onset of

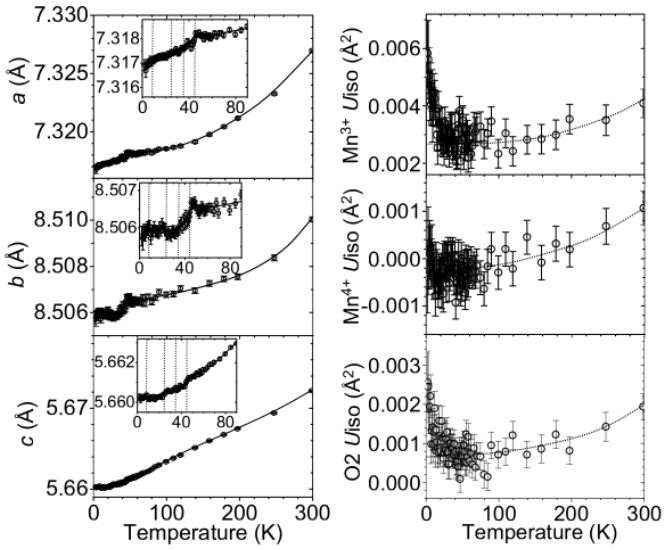

Figure 3.11: The variation of the lattice parameters (left) and selected atomic displacement parameters (right) as a function of temperature. Reprinted figure with permission from reference 38. Copyright 2004 by the American Physical Society.

ferroelectric order with $\mathbf{P} \parallel b$ [135], indicated by a sharp feature in the dielectric constant (figure 3.9(b)). In the temperature range 33 K > T > 24 K the system locks into a CM magnetic structure, ($\delta = \frac{1}{2}$, $\tau = \frac{1}{4}$), which is diagrammatically shown in Fig. 3.13, as refined from neutron powder diffraction experiments [38, 139]. The terbium magnetic structure is omitted from the figure as it could not be reliably determined. The lattice parameters in this phase were refined to be $a = 7.3251$ Å, $b = 8.5168$ Å, and $c = 5.6750$ Å [144]. A small *c*-axis component for the magnetic moments was reported, however the actual *c*-axis magnetic structure also could not be reliably refined from the powder data [139]. A single-crystal experiment is yet to be published, however one would expect a cycloidal *c*-axis magnetic structure, as determined in other members of the $R\mathrm{Mn_2O_5}$ series [73, 130]. It is surprising that T_{CM} does not coincide with T_{FE}; this cannot be explained through theoretical symmetry analysis [146]. The value of T_{CM} = 33 K is indeed in dispute as recent

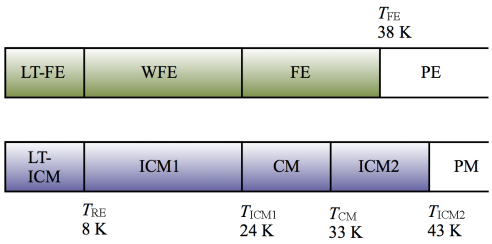

Figure 3.12: The low temperature multiferroic phase diagram of $TbMn_2O_5$ [38, 139]. The ferroelectric transitions are shown on the upper green bar, and the magnetic transitions on the lower blue bar, both with the same scale.

synchrotron x-ray studies have shown that the transition occurs at 38 K [147, 148], concomitant with T_{FE}. At T_{ICM1} = 24 K $TbMn_2O_5$ enters another incommensurate phase (ICM1) with δ = 0.48 and τ = 0.32 [38], accompanied by a dramatic loss of electric polarisation. This is an unlikely transition as one might expect a commensurate ground state of any ordered system. The behaviour of the magnetic propagation vector and the magnetic neutron scattered intensity through the multiferroic phases is shown in figure 3.14 [145].

Below T_N, the manganese magnetic structure spin polarises the electronic states of the terbium ions such that they adopt a long range order with the same propagation vector as the manganese sub-lattices. This phenomena was shown to occur and discussed not only in $TbMn_2O_5$ [139], but also in other manganese oxide multiferroics such as $TbMnO_3$ [53] and $HoMn_2O_5$ [127]. Blake *et al.* [139] suggested that this is specifically due to an interaction with the Mn^{4+} spin density. The existence of a separate spontaneous magnetic order on the terbium ions was hypothesised below T_{RE} = 8 K [141], resulting in the dramatic increase in magnetic diffraction intensity in figure 3.14 and a large increase in the electric polarisation [145]. The terbium sub-lattice magnetic structure in this phase is to some extent coupled to that of the manganese as it adopts the same propagation vector. However, upon saturation in an applied magnetic field of 2.5 T, evident in figure 3.9(a), neutron diffraction data

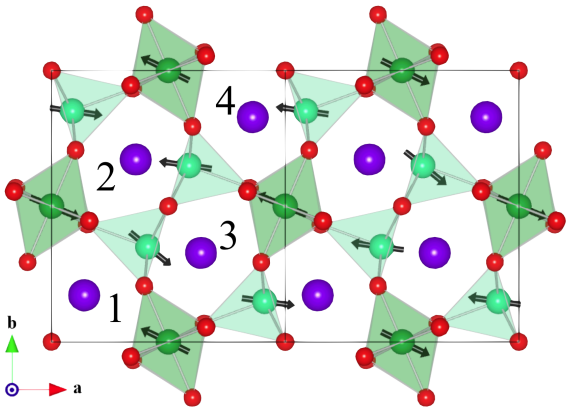

Figure 3.13: The commensurate manganese magnetic structure of $TbMn_2O_5$ in the *ab*-plane, adapted from Fig. 3 in reference 38. Antiferromagnetically aligned moments lie on the Mn^{3+} (light green) and Mn^{4+} (dark green) ions that are located in square-based pyramid and octahedral coordinations respectively; the terbium and oxygen ions are shown in purple and red, respectively.

showed that the terbium ions became ferromagnetically ordered with no measurable change in the manganese magnetic structure [38]. This indicates that the f-d interaction in $TbMn_2O_5$ is in fact weak. The opposite is true for $HoMn_2O_5$, where an applied magnetic field affects both the holmium and manganese sub-lattices, suggesting a stronger f-d coupling [117]. YMn_2O_5 was investigated in order to test the invariance of the manganese magnetic order under applied magnetic fields, and hence show that the manganese structure can only be modified *via* a strong interaction with the rare-earth ions. This study did indeed show that the manganese magnetic structure was invariant in magnetic fields up to 8 T at 1.6 K [117].

Koo *et al.* have measured the coexistence of the Mn^{3+}, Mn^{4+} and Tb^{3+} magnetic sub-lattices through neutron [149] and synchrotron x-ray [147] diffraction experiments, in order to investigate the discommensuration and loss of spontaneous electric polarisation in $TbMn_2O_5$ at T_{ICM1}. It was shown that the diffraction intensity attributed to each magnetic order had a different temperature dependence.

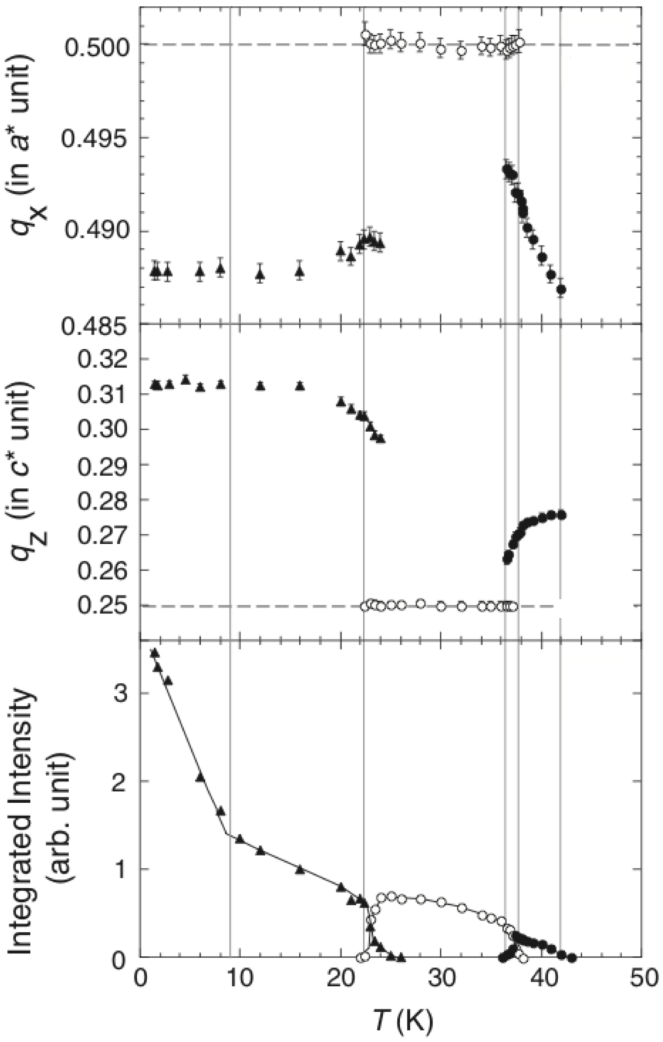

Figure 3.14: The temperature dependence of the magnetic propagation vector and the neutron diffracted intensity measured through the multiferroic phases of $TbMn_2O_5$. The figure is reproduced from reference 145, published in the Journal of the Physical Society of Japan.

Also, by studying a number of magnetic diffraction signals, it was clear that the relative diffraction intensities associated with the three sub-lattices were also strongly dependent upon the wave vector. The total magnetic structure therefore cannot be described by a single order parameter. This gives rise to a scenario whereby the competition and phase slipping between order parameters may result in discommensuration, as observed in $TbMn_2O_5$. The loss of electric polarisation was then described by assuming the exchange-striction model and incorporating anti-phase domain walls [147]; essentially the same argument as that proposed by Chapon *et al.* [38] and Radaelli *et al.* [121], described in section 3.2.3.

Finally, before moving on to the experimental sections of this chapter we comment on an *ab-initio* theoretical study of $TbMn_2O_5$ based upon density functional theory calculations [150, 151]. These calculations verified a number of the key points discussed above. Firstly, the small ionic displacements that break inversion symmetry ($Pb2_1m$) were predicted, and shown to be largest at the Mn^{3+} sites ($\delta y \simeq 10^{-3}$). The displacements were calculated to have mirror symmetry in the *a*-direction, but not in the *b*-direction, in agreement with the existence of ferrielectricity with a net polarisation parallel to the *b*-axis. The most significant result of these calculations, however, was the prediction of energetically degenerate domains. The degeneracy is lifted by the atomic displacements in which the electric polarisation originates. The two domains are equivalent to those predicted in neutron diffraction studies [38, 121, 130]. This result is summarised diagramatically in figure 3.15 [150].

In the early sections of this chapter it was shown that the behaviour of the rare-earth ions in the RMn_2O_5 series is likely to be the primary mediator behind the varied magneto-electric phenomena observed. To elucidate further the magneto-electric properties of $TbMn_2O_5$ we have performed a novel study of the terbium magnetism. The terbium magnetic order couples with the manganese magnetism

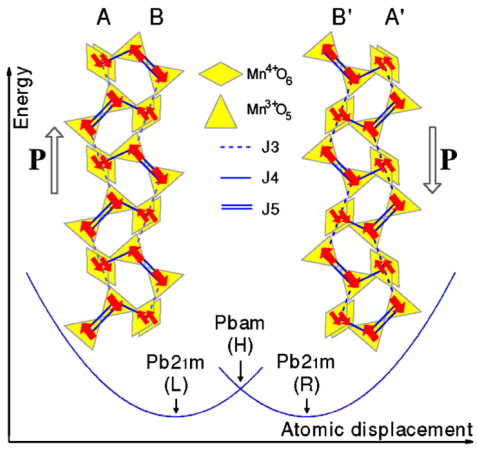

Figure 3.15: The two energetically degenerate magnetic domains predicted through *ab-initio* calculations. The inversion symmetry breaking atomic displacements lifts the degeneracy, making the two domains equivalent to those predicted in neutron diffraction studies [38, 121, 130]. Reprinted figure with permission from reference 150. Copyright 2007 by the American Physical Society.

and the lattice, the effect of which increases at low temperature due to an increase in the magnitude of the average terbium magnetisation. It is however not possible to directly probe the magnetic moment of the rare-earth ion using neutron diffraction or bulk transport or magnetisation measurements. Furthermore, no magnetic structure refinement has been reported for the ICM1 or LT-ICM phases.

In the remainder of this chapter we have investigated the interaction of the terbium ion sub-lattice with the manganese spins (and also any independent ordering) in the commensurate phase by magnetic resonant x-ray diffraction (MRXD). It can be assumed that the terbium $5d$ valence states have a large overlap not only with the lower energy terbium $4f$ states, but also with the $3d$ manganese states. The terbium $5d$ states will therefore be spin polarised *via* interaction with neighbouring Mn^{4+}, Mn^{3+}, and Tb $4f$ electronic spin density. MRXD is an electronic state and ion specific technique, and so is ideal for unravelling such complex magnetic interactions. In this case, at the terbium L_{III} edge, the $5d$ states are probed by the

$2p \Leftrightarrow 5d$ dipole (E1-E1) transition and the $4f$ states, in which the unpaired electrons exist, are probed by the $2p \Leftrightarrow 4f$ quadrupole (E2-E2) transition, as explained later. Also, we have solved the terbium ion magnetic structures in both CM and LT-ICM phases by MRXD via a novel technique that employs full linear polarisation analysis [60, 152].

3.4 Experiment

3.4.1 Resonant x-ray diffraction

A high quality single crystal of $TbMn_2O_5$ with dimensions approximately 2 x 2 x 0.5 mm was grown at the Department of Chemistry in the National Taiwan University by flux growth. The single crystal was prepared such that the (4, 4, 0) Bragg reflection was close to surface normal. This reflection was chosen due to constraints in the physical size of the sample. However, this direction is suitable for measuring magnetic satellites of structural Bragg reflections. As such, we set out to measure ($h\pm\delta$, h, $0\pm\tau$) type reflections, where the magnetic propagation vector $\mathbf{q} = (\delta,\ 0,\ \tau)$. Prior to the experiment, the sample surface was polished to reduce surface damage and roughness that would lead to a reduction in the scattered intensity. The sample was then mounted on the six-circle diffractometer in the second experimental hutch on beam line ID20 [153] at the European Synchrotron Radiation Facility; a 6 GeV machine ideally suited to hard x-ray energy studies. The instrument is shown in figure 3.16. The crystallographic c-axis was orientated perpendicular to the horizontal scattering plane.

Beam line ID20 is located on an undulator x-ray source, providing high intensity x-rays, horizontally polarised (with respect to the laboratory), in the energy range 3 keV to 30 keV. The incident x-ray energy is tuneable through use of a double bounce silicon monochromator, giving an energy resolution of $\Delta E/E < 10^{-4}$. This

is essential for performing high resolution energy scans through element specific absorption edges, described later.

The six-circle, horizontal scattering diffractometer incorporates an Oxford Instruments 10 T superconducting split-coil cryomagnet sample environment. Stable sample temperatures were achieved, down to a base temperature of 2 K, by a helium flux cryostat.

3.4.2 Full linear polarisation analysis

Full linear polarisation analysis is a relatively new technique, which has been shown to be capable of unravelling multipole resonances in K_2CrO_4 [60] and modelling competing magnetic domain contributions within $NpRhGa_5$ [152]. Chapter 1 describes the theory behind resonant x-ray diffraction. In full linear polarisation analysis we exploit the scattered beam's polarisation dependence on the magnetic moment direction. When measured in terms of Poincaré-Stokes parameters, P1 and P2, the theory used to describe, simulate and fit the scattered polarisation dependence, is summarised as follows:

$$\mathrm{P1} = \frac{|\sum_j f_{E1,E2}^{RXMS}(\epsilon'_\sigma, \epsilon, \hat{\mathbf{z}}_j, \mathbf{k}', \mathbf{k}) e^{i\mathbf{q}.\mathbf{r_j}}|^2 - |\sum_j f_{E1,E2}^{RXMS}(\epsilon'_\pi, \epsilon, \hat{\mathbf{z}}_j, \mathbf{k}', \mathbf{k}) e^{i\mathbf{q}.\mathbf{r_j}}|^2}{|\sum_j f_{E1,E2}^{RXMS}(\epsilon'_\sigma, \epsilon, \hat{\mathbf{z}}_j, \mathbf{k}', \mathbf{k}) e^{i\mathbf{q}.\mathbf{r_j}}|^2 + |\sum_j f_{E1,E2}^{RXMS}(\epsilon'_\pi, \epsilon, \hat{\mathbf{z}}_j, \mathbf{k}', \mathbf{k}) e^{i\mathbf{q}.\mathbf{r_j}}|^2} \tag{3.2}$$

and

$$\mathrm{P2} = \frac{|\sum_j f_{E1,E2}^{RXMS}(\epsilon'_{+45^\circ}, \epsilon, \hat{\mathbf{z}}_j, \mathbf{k}', \mathbf{k}) e^{i\mathbf{q}.\mathbf{r_j}}|^2 - |\sum_j f_{E1,E2}^{RXMS}(\epsilon'_{-45^\circ}, \epsilon, \hat{\mathbf{z}}_j, \mathbf{k}', \mathbf{k}) e^{i\mathbf{q}.\mathbf{r_j}}|^2}{|\sum_j f_{E1,E2}^{RXMS}(\epsilon'_{+45^\circ}, \epsilon, \hat{\mathbf{z}}_j, \mathbf{k}', \mathbf{k}) e^{i\mathbf{q}.\mathbf{r_j}}|^2 + |\sum_j f_{E1,E2}^{RXMS}(\epsilon'_{-45^\circ}, \epsilon, \hat{\mathbf{z}}_j, \mathbf{k}', \mathbf{k}) e^{i\mathbf{q}.\mathbf{r_j}}|^2} \tag{3.3}$$

All quantities and parameters used are defined in section 1.3.4. By a least-squares method, it is possible to fit equations 3.2 and 3.3 to experimental data (measurement of P1 and P2 as a function of incident polarisation) and hence refine the

Figure 3.16: The six-circle, horizontal scattering diffractometer with *in-situ* 10 T superconducting magnet, located in the second experimental hutch at ID20, ESRF.

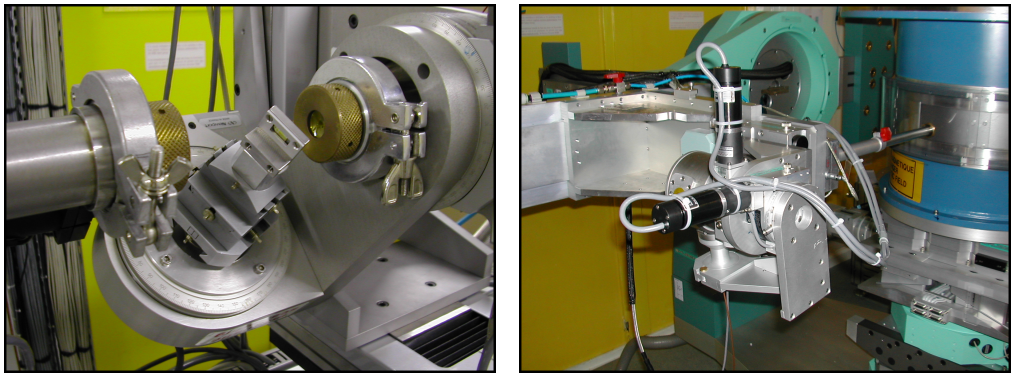

(a) Diamond phase plate (b) Polarisation analyser

Figure 3.17: (a) The diamond phase plate and (b) the polarisation analyser, photographed on beam line ID20, ESRF.

magnetic moment directions.

The technique of using a phase plate, positioned in the incident beam such that it rotates the horizontally polarised light to any arbitrary linear polarisation, was employed. A 720 μm thick diamond crystal was used as the phase retarder by scattering near the (111) reflection. A convenient forward-scattering geometry is possible due to the low absorption coefficient of diamond. Figure 3.17(a) shows the diamond phase plate in the incident beam path at ID20.

The phase plate was calibrated by measuring the scattered intensity in the σ-channel when rotating the phase plate theta through the Bragg angle, see figure 3.18. A minimum in the calibration curve (blue dashed line in figure 3.18) was selected as the angle at which the diamond crystal behaves as a half-wave plate. A minimum 92 % polarisation conversion when operating as a half-wave plate was achieved. Note that a χ phase plate rotation about the incident beam (see figure 3.19) equates to a $\epsilon = 2\chi$ rotation in polarisation.

The scattered beam polarisation was determined using a gold analyser crystal scattering at the (2, 2, 2) reflection. The methodology behind polarisation analysis is described in section 1.3.4, and the apparatus is shown in figure 3.17(b). The key

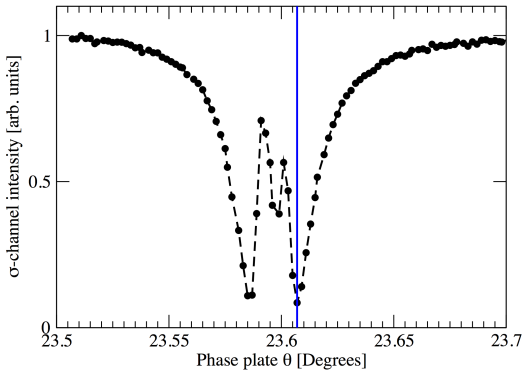

Figure 3.18: The transmitted intensity in the σ-channel as a function of the phase plate theta angle. The diamond crystal behaves as a half-wave plate when aligned such that theta corresponds to a minimum in the graph as shown by the blue line [154]. This is symmetrical about the Bragg angle.

elements of the experimental setup facilitating full linear polarisation analysis, as described above, are diagrammatically illustrated in figure 3.19.

3.5 Results and Discussion

3.5.1 Resonant x-ray diffraction

First, the sample fluorescence was measured by scanning the incident x-ray energy through the terbium L_{III}-edge, with the detector slits wide open and at a position well away from any diffraction peaks. This measurement, shown in figure 3.20, confirmed that the x-ray beam was incident on the sample and provided a reference in energy to which to compare the resonant spectra. The terbium absorption edge, defined as the point of inflection in the energy spectra, was found at 7.516 keV. This is 2 eV higher than the binding energy of elemental terbium, however such an energy shift is to be expected for a covalently bonded oxide. The crystal was then aligned through locating a number of structural Bragg reflections.

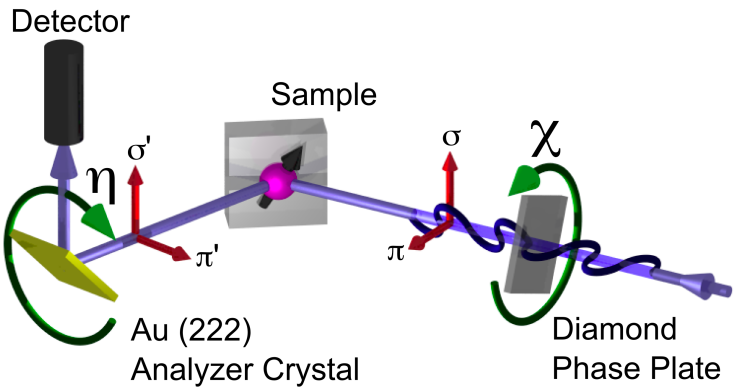

Figure 3.19: A schematic of the experimental setup. The polarised x-ray beam (blue) enters from the right. The polarisation of the incident beam was rotated by a diamond phase-plate. The scattered beam polarisation was determined through a separate scattering process from an analyser crystal prior to detection. Note the σ and π orientations where primes (eg. σ', π') refer to the scattered beam.

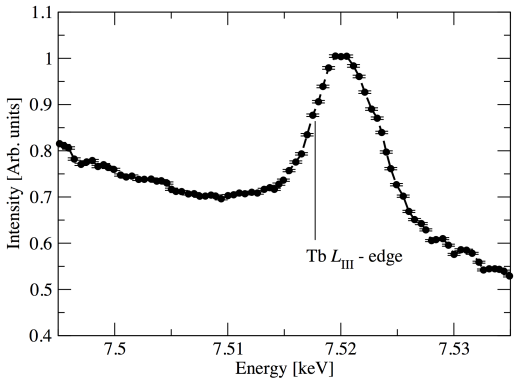

Figure 3.20: The measured fluorescence curve of $TbMn_2O_5$ showing the terbium L_{III} absorption edge at 7.516 keV (labelled in the figure).

The sample was then cooled to 25 K; within the CM phase. Having realigned the crystal for the low temperature lattice parameters, a number of magnetic satellite reflections were located around the (4, 4, 0), (2, 2, 0), (4, 3, 0), (4, 2, 0) and (5, 2, 0) Bragg reflections with the expected propagation vector **q**=(δ, 0, τ), where $\delta = 0.5$ and $\tau = 0.25$. Importantly, the use of a polarisation analyser (PA) crystal greatly reduces the charge background, essential for observing the weak magnetic reflections. It was only possible to observe a full set of satellite reflections (*i.e.* the ($+\delta$, 0, $+\tau$), ($+\delta$, 0, $-\tau$), ($-\delta$, 0, $+\tau$) and ($-\delta$, 0, $-\tau$)) around the (4, 4, 0) reflection, probably due to the weak intensity of others. In horizontal scattering geometry, the unrotated incident x-ray polarisation is in the π channel (section 1.3.4). The magnetic reflections were on average seven times as intense in the rotated $\pi - \sigma'$ channel than in the $\pi - \pi'$ channel. We therefore measured only in the $\pi - \sigma'$ in the following survey of the energy resonances.

Scans of the scattered intensity as a function of incident x-ray energy through the terbium L_{III} edge at constant wavevector were performed at the (4, 4, 0) magnetic satellite reflections in the CM phase at 25 K. Two distinct energy resonances at each reflection were observed, shown in figure 3.21. These excitations are centred at 7.510 and 7.518 keV. By comparison with the fluorescence spectrum shown in figure 3.20, the higher-energy peak occurs just above the terbium L_{III} absorption edge, as one would expect for an E1-E1 dipole transition. The other resonance is likely to be of quadrupolar E2-E2 origin. It exists 8 eV lower, a characteristic shift between dipole and quadrupole energy resonances in the rare-earth series [155–157]. Indeed, the E2-E2 transition usually occurs a few eV below the absorption edge, due to a stronger interaction between the core hole and excited electron [158].

The sample was then cooled to base temperature (2 K) well below both the ICM1 transition temperature and the onset of Tb-Tb order. The (4, 4, 0) satellite reflections, now at incommensurate positions, were re-found. At this temperature

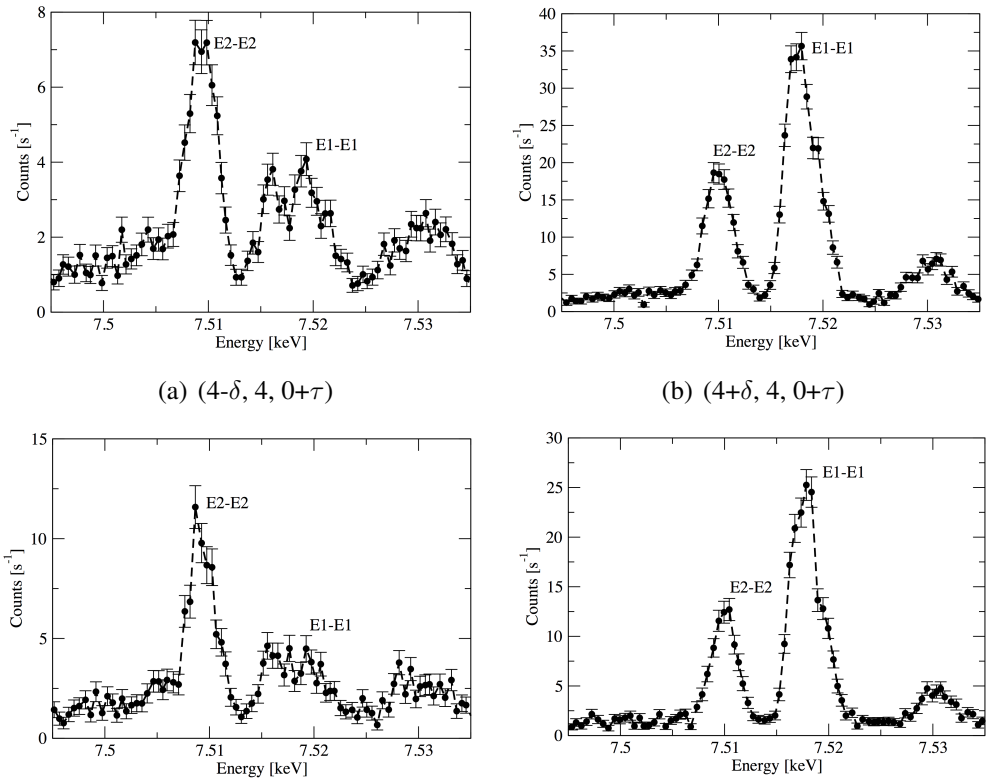

(a) (4-δ, 4, 0+τ) (b) (4+δ, 4, 0+τ)

(c) (4-δ, 4, 0-τ) (d) (4+δ, 4, 0-τ)

Figure 3.21: Scans of the scattered intensity of the (4, 4, 0) satellite reflections measured as a function of the incident x-ray energy at 25 K, in the CM phase, measured through the terbium L_{III}-edge in the $\pi - \sigma'$ polarization channel.

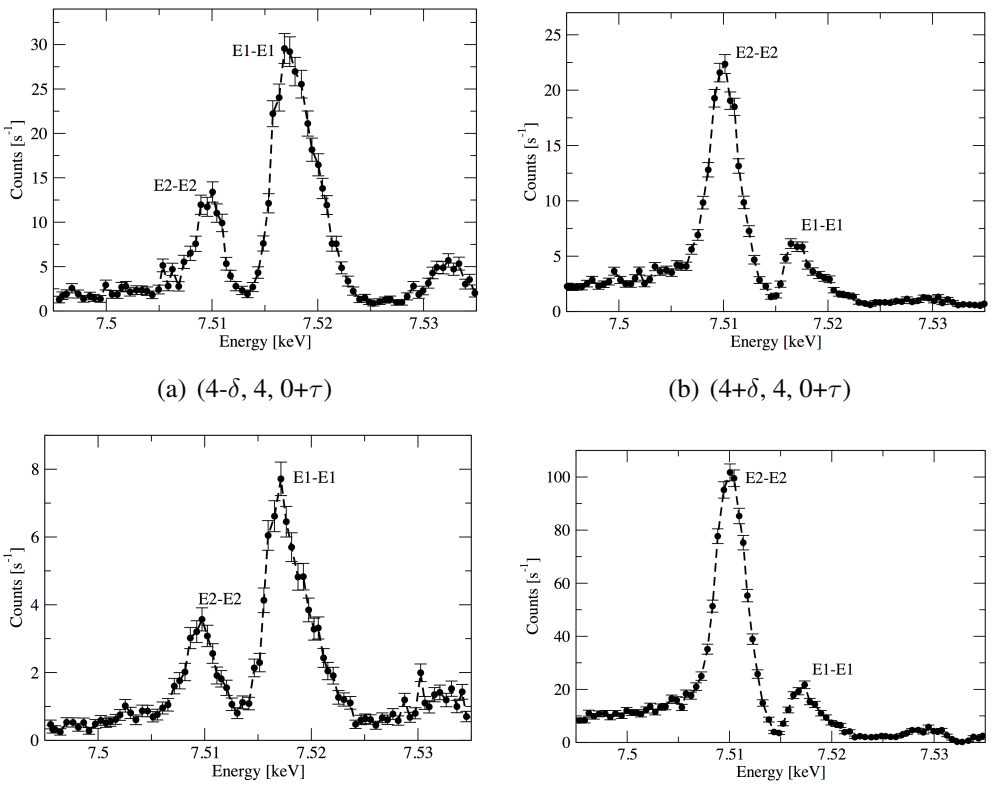

(a) (4-δ, 4, 0+τ) (b) (4+δ, 4, 0+τ)

(c) (4-δ, 4, 0-τ) (d) (4+δ, 4, 0-τ)

Figure 3.22: Scans of the scattered intensity of the (4, 4, 0) satellite reflections measured as a function of the incident x-ray energy at 2 K, in the LT-ICM phase, measured through the terbium L_{III}-edge in the $\pi - \sigma'$ polarization channel.

the magnetic propagation vector was $\mathbf{q}$ = (0.487, 0, 0.315), in good agreement with the literature [38, 139]. The energy scans were then repeated, as shown in figure 3.22. We note that in the CM phase the relative intensity of the E1-E1 resonance is greater than that of the E2-E2 resonance for $+\delta$ reflections, while the opposite is evident for the $-\delta$ reflections. This trend is reversed in the ICM1 phase.

Due to experimental time constraints we focused only on the (4+δ, 4, 0-τ) reflection (it being the most intense in the LT-ICM phase) in further data collections, and hence the analysis. To gain an estimate of the magnetic correlation within the sample, the (4+δ, 4, 0-τ) peak (measured along the highest instrumental resolution

direction, [1, 0, 0], at the E1-E1 transition) was fitted with a Lorentzian squared function centred at h = 4.488. The peak and fit is shown in figure 3.23.The inverse correlation length, defined as

$$\xi^{-1} = \frac{2\pi}{a}\Delta\mathbf{h}_{HWHM}, \tag{3.4}$$

where a is the lattice parameter and $\Delta\mathbf{h}$ is the half width at half maximum, gave $\xi^{-1} = 2.212\times10^{-3}\pm6.2\times10^{-5}\text{Å}^{-1}$. The inverse correlation length of this reflection remained constant within experimental error in the temperature range $2<T<35$ K, except for a slight increase close to the ICM1/CM transition. The real space correlation length, ξ, for a Lorentzian squared peak profile may be found using the following relationship [159]

$$\Delta\xi^{-1}\Delta\xi = 1.38127(8) \tag{3.5}$$

giving $\xi = 908 \pm 20$ Å for our measurement, indicating that the magnetism in our sample is very long range correlated.

The wavevector positions in reciprocal space and the transition temperatures of the ICM1 and CM reflections were measured and compared with neutron diffraction results to confirm that the reflections were indeed of magnetic origin. Figure 3.24 shows the position in h (Fig. 3.24, top pane) and position in l (Fig. 3.24 middle pane) as functions of temperature, measured at the E1-E1 resonance. The transition from an incommensurate to a commensurate wavevector on warming is clear and agrees well with published δ and τ values [38, 139]. In addition we observed that the two phases coexist in the temperature range of 20 - 22 K. This coexistence has also been observed by both soft x-ray and neutron diffraction studies [143, 145], showing the phase transition to be strongly first order. The correlation length of the reflection decreases in the coexistence region, evidence of the formation of smaller domains

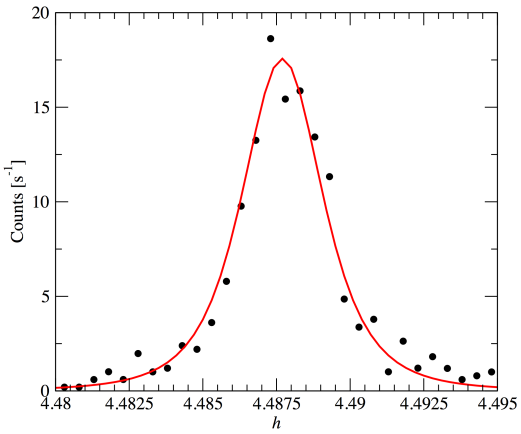

Figure 3.23: Scan of the magnetic (4+δ, 4, 0-τ) reflection along the h reciprocal space direction (black circles), in the LT-ICM phase at the E1-E1 resonance. The red line shows a fit of a Lorentzian squared profile from which the half width at half maximum was evaluated, used to calculate the correlation length.

through the phase transition. The lower pane of figure 3.24 shows the temperature dependence of the integrated intensity of the (4+δ, 4, 0-τ) reflection measured in the h direction. Upon cooling, the intensity of the CM reflection decreases. At 22 K, the ICM1 reflection simultaneously begins to increase in intensity and continues to do so below 20 K, at which temperature the CM reflection becomes extinct. The CM and ICM1 data, which are shown in figure 3.24 in blue and black, respectively, were measured on different experiments. It is therefore not possible to draw direct comparisons of the magnitude of the integrated intensity in the two phases. We note that the widely acknowledged transition temperature of 24 K falls outside this range. This discrepancy is likely to be a result of x-ray beam heating or a discrepancy in the experimental calibration due to the limited proximity of the temperature sensor to the sample.

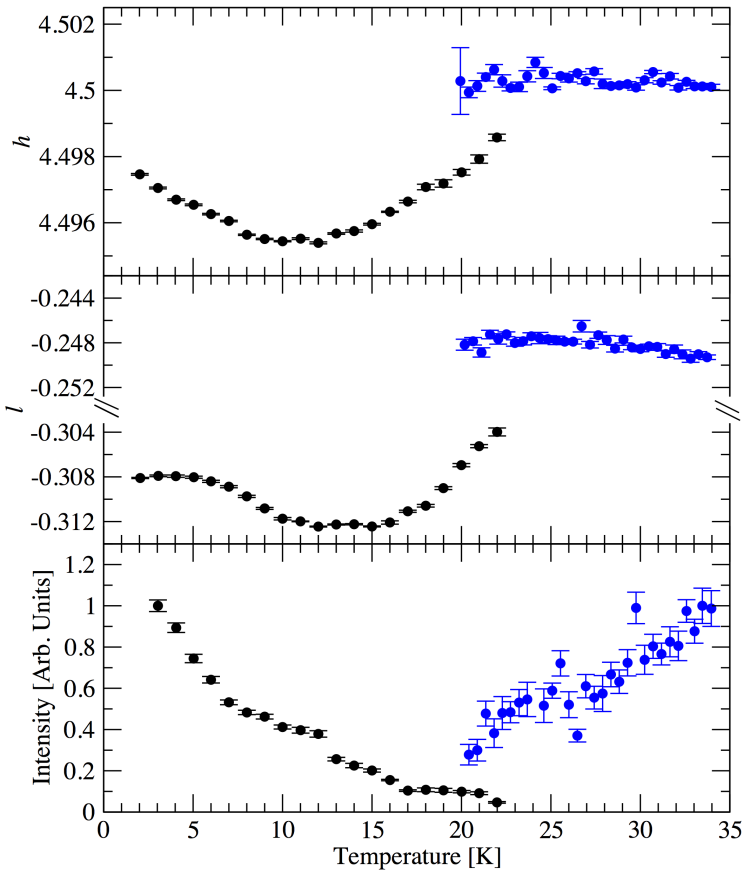

Figure 3.24: The position in reciprocal space measured along h (top pane) and l (middle pane) of the (4+δ, 4, 0-τ) magnetic satellite reflection as a function of temperature in the range 2 K $< T <$ 34 K. The CM - ICM1 phase transition at approximately 21 K is clearly seen, together with the phase coexistence occurring between 20 - 22 K. Within the ICM1 phase the incommensurate wavevector varies in both h and l as a function of temperature. Bottom pane: The temperature dependence of the integrated intensity of the (4+δ, 4, 0-τ) reflection measured in the h direction. The black (ICM1) and blue (CM) data were collected on different experiments. Direct comparison of the scattered intensity in the two phases is therefore not possible, however one can observe the trend of the CM reflection decreasing in intensity on decreasing temperature, and the growth of the ICM1 reflection on cooling below 22 K.

3.5.2 Full linear polarisation analysis

Full linear polarisation analysis of the (4+δ, 4, 0-τ) reflection was performed at an energy of 7.518 keV corresponding to the E1-E1 transition, probing the terbium $5d$ band. Figure 3.25 shows the Poincaré-Stokes parameters P1 and P2, measured as functions of incident polarisation in the CM phase.

In the *R*Mn_2O_5 series it was hypothesised that a magnetic rare-earth sub-lattice (excluding, for example, yttrium and lanthanum compounds) is spin polarised below $T_{\mathrm{N}} \sim 45$ K, despite the rare-earth ordering temperature being much lower; typically < 10 K [130, 139]. The spin polarisation is predicted to occur due to the interaction of the rare-earth moment with the magnetic dipole field associated with the manganese magnetic structure, in particular that of the Mn^{4+} spin density. By probing the delocalised terbium $5d$ valence states at this transition, any refinement or simulation of magnetic structure would reveal the origin of the spin polarisation.

Superimposed in figure 3.25 are three simulations calculated using equations 3.2 and 3.3, and the respective theory outlined in sections 1.3.4 and 1.3.3. The blue solid line shows the line shape calculated if the terbium ion magnetism in the CM phase is solely a result of interaction with the Mn^{4+} dipole field, as predicted [130, 139]. The dashed red line is the line shape calculated if the scattering occurs due to a similar interaction with the Mn^{3+} spin density, and the green dash-dotted line is the line shape of a simulation of the scattering due to the spin polarisation of the $5d$ states by the localised terbium $4f$ magnetic moments. The terbium $4f$ magnetic order also exists as a consequence of spin polarisation through interaction with the manganese magnetic structure, the directions of which were refined by the fit to the data taken at the E2-E2 transition, presented later in this chapter.

The reduced χ^2 values of the Mn^{4+}, Mn^{3+}, and Tb simulations are 2.8, 17.9, and 5.8, respectively. This result conclusively verifies the hypothesis of Blake *et al.* [139] that the terbium sub-lattice is polarised by the close proximity of the

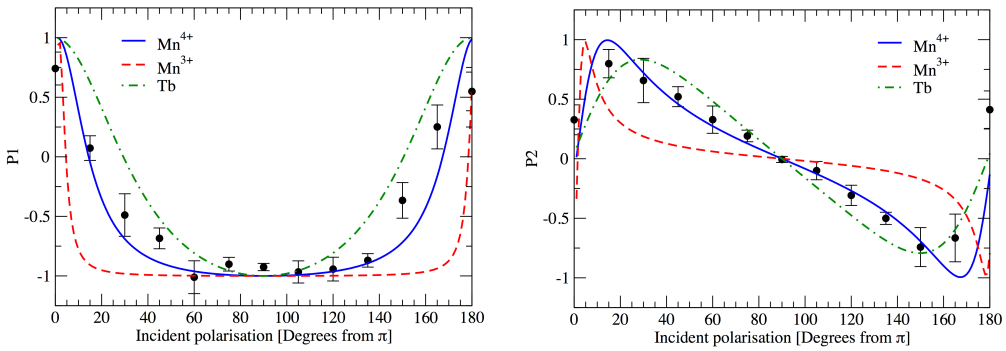

(a) P1 (b) P2

Figure 3.25: A plot of the measured Poincaré-Stokes parameters P1 and P2 as a function of the incident x-ray polarisation of the commensurate (4+δ, 4, 0-τ) reflection at the E1-E1 energy resonance at 25 K. Simulations of the Mn^{4+} and Mn^{3+} magnetic structures (as refined by Blake *et al.*[139]) are shown as blue solid and red dashed lines respectively. A simulation of the terbium magnetic structure scattering at the E1-E1 transition in this phase, as refined later in this chapter at the E2-E2 transition, is shown by the green dash-dotted line.

Mn^{4+} spin density, as opposed to Mn^{3+} spin density. A reduced χ^2 value of 2.8 of the Mn^{4+} simulation, when compared to the value of 5.8 of the Tb $4f$ band simulation, also shows that the Tb $5d$ band is predominantly polarised by the Mn^{4+} $3d$ band; however, one clearly cannot exclude the interaction with the terbium $4f$ spin configuration. Indeed, in a MRXS study of $HoMn_2O_5$ [127] performed at the dipole transition at the Ho L_{III} edge, an azimuthal dependence on scattered intensity measured in the commensurate phase, showed excellent agreement with a theoretical azimuthal dependence on scattering from holmium with the $5d$ band polarised by the $4f$ band magnetic structure.

To confirm this result, a conventional azimuthal dependence of the scattered intensity in the $\sigma - \pi'$ channel was measured at the same energy at the (4+δ, 4, 0+τ) reflection in a vertical scattering geometry. The data, shown in figure 3.26, compared to a simulation of the expected azimuthal dependence, assuming scattering from the terbium sub-lattice when polarised by Mn^{4+} spin density (solid line in

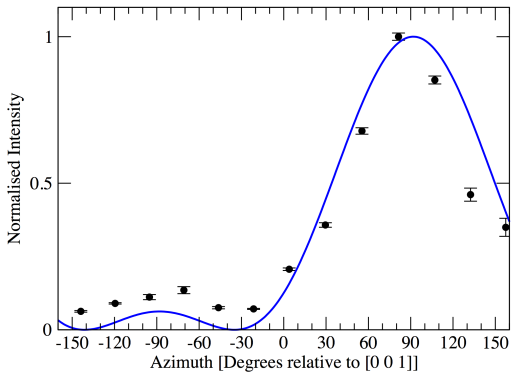

Figure 3.26: The measured intensity of the commensurate (4+δ, 4, 0+τ) reflection at the E1-E1 energy resonance at 25 K in the $\sigma - \pi'$ channel as a function of azimuth angle of the sample. The solid line shows a simulation of the azimuthal dependence expected when the terbium magnetic ions are influenced solely by the Mn^{4+} magnetic structure [as refined by Blake *et al.*[139]].

figure 3.26), also shows excellent agreement.

The full linear polarisation analysis was performed again at the same energy (7.518 keV) in the incommensurate phase. The data is shown in figure 3.27. Due to the lack of a refined magnetic structure in the literature of the ICM1 phase the large number of free parameters results in an unreliable refinement using this technique. We can therefore only make comparison to simulations of known magnetic structures. The CM Mn^{4+} magnetic structure simulation, which is shown to be of best agreement to the CM polarisation analysis presented in figure 3.25, is shown here as a blue line. In comparison to the data, the sensitivity of this technique to a magnetic structure rearrangement upon the CM/ICM1 transition, resulting in a change of spin polarisation of the $5d$ band, is clear. This could be due to a realignment of the manganese magnetic structure or a stronger interaction with the terbium sublattice or both. The green dash-dotted line plotted in figure 3.27 is a simulation of the scattering expected due to an interaction of the terbium $5d$ band with the terbium $4f$ magnetic structure, as refined later in this chapter at the E2-E2 transition. From

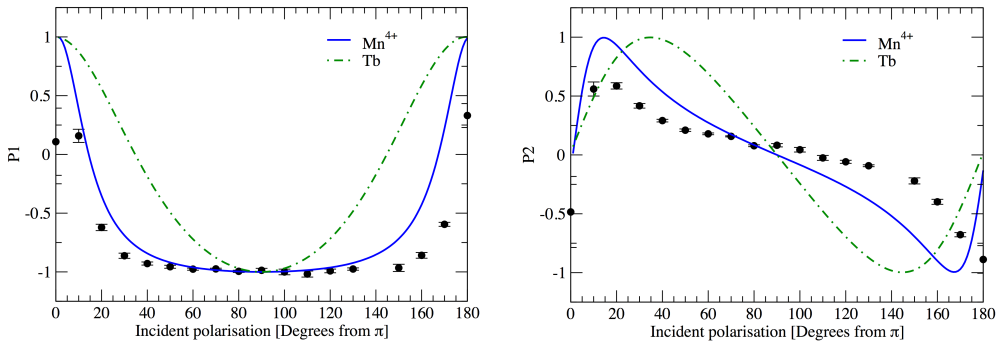

(a) P1 (b) P2

Figure 3.27: A plot of the measured Poincaré-Stokes parameters P1 and P2 as a function of incident x-ray polarisation of the incommensurate (4+δ, 4, 0-τ) reflection at the E1-E1 energy resonance at 2 K. The commensurate Mn^{4+} magnetic structure simulation shown in blue in figure 3.25 is shown here again. The green dash-dotted line shows a simulation of the terbium magnetic structure scattering at the E1-E1 transition in the LT-ICM phase, as refined later in this chapter at the E2-E2 transition.

the poor agreement of the terbium simulation, we would conclude that in this phase the $5d$ band remains predominantly polarised by the manganese magnetic structure. The difference in full polarisation analysis data between the two phases is therefore likely be a result of a realignment of Mn^{4+} moments.

The full linear polarisation analysis measurement was also conducted in the commensurate phase at the E2-E2 resonance (7.510 keV). At this transition we directly probed unpaired electrons in the terbium $4f$ band and, hence, the terbium sub-lattice magnetic structure. Figure 3.28 shows the data and a least-squares fit (blue solid line), similar to the analysis used in a study of UPd_3 [160]. We note that in the fitting procedure we determine only two parameters, P1 and P2, from which we find the magnetic moment directions. As P1 and P2 follow well defined functions (equations 3.2 and 3.3), in theory, it is therefore only necessary to measure the scattered polarisation at three different incident polarisations. However, in order to minimise systematic and random errors in the experimental procedure and obtain

a reliable fit, the scattered beam polarisation was measured at substantially more incident polarisation states. This makes full linear polarisation analysis essential.

There are four crystallographically distinct terbium ions in the magnetic unit cell, labelled here according to the convention used by Blake *et al.*, [139] as shown in figure 3.13. In a recent neutron single crystal diffraction study of $HoMn_2O_5$ [130], which showed very similar macroscopic properties and microscopic structure to $TbMn_2O_5$, holmium ion positions 1 and 2 were found to have the same moment direction as were holmium ions 3 and 4. This is in contradiction to the earlier neutron powder diffraction study by Blake *et al.* [139] in which both terbium and holmium compounds have the rare-earth positions 1-4 and 2-3 paired in the refinement. In fitting the data it was evident that it was necessary to pair the terbium ions as in the recent $HoMn_2O_5$ single crystal study. Fixing the *a* component of moments on sites 1 and 2 and the *b* component of moments on sites 3 and 4 gave a fit with four degrees of freedom. Magnetic moment directions on the terbium 1 and 2 sites were refined to be $10.5 \pm 2.6^\circ$ in the *ab*-plane relative to the *a*-axis and $0.2 \pm 0.1^\circ$ out of plane, and on the terbium 3 and 4 sites $292.5 \pm 2.0^\circ$ in the *ab*-plane relative to the *a*-axis and $0.2 \pm 0.1^\circ$ out of plane.

These moment directions are in contradiction with neutron powder diffraction measurements on the RMn_2O_5 series as reported by Blake *et al.* [139], however, so are recent refinements of $HoMn_2O_5$ by neutron and synchrotron single-crystal data [73, 127, 130] when compared to the same 2005 study. In these $HoMn_2O_5$ experiments, holmium directions were reported to be pointing along the *a* and *b* axes with a small component in the direction of the *c*-axis. These directions are comparable to those refined in this study on $TbMn_2O_5$. Here, terbium moments are found to be coupled in the same fashion and lie approximately along the crystallographic axes in the *ab*-plane (the moments are in fact refined to be canted away from the axes by approximately 10°) with a slight *c*-axis component. However, the configuration of

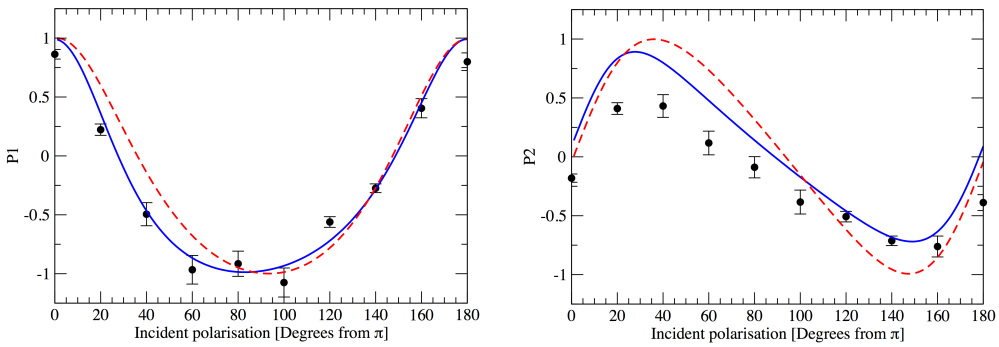

(a) P1 (b) P2

Figure 3.28: A plot of the measured Poincaré-Stokes parameters P1 and P2 as a function of incident x-ray polarisation of the commensurate (4+δ, 4, 0-τ) reflection at the E2-E2 energy resonance at 25 K. A least squares fit with a reduced χ^2 value of 13.9 is shown in blue (solid line). See text for the refined moment directions. The incommensurate fit performed in figure 3.29 is shown by the red dashed line.

the spin orientations of the rare earth and the Mn^{4+} magnetic structure differ to that of the holmium compound.

By considering the manganese magnetic structure of $TbMn_2O_5$ reported in references 38 and 139, it is not possible to explain the terbium ordering in terms of a simple antiferromagnetic super exchange interaction between terbium and nearest-neighbour Mn^{4+} ions where the manganese moment *a* and *b* axis components cancel at sites 1-2 and 3-4, respectively, the argument that was put forward by Vecchini *et al.* [130] in the $HoMn_2O_5$ study. Section 3.2 describes the possible magnetic domains of the RMn_2O_5 series. This discussion of domains introduced a possible manganese magnetic structure related by inversion symmetry to that reported in references 38 and 139. If one considers the latter manganese magnetic structure then the CM terbium magnetic structure predicted by us can be tentatively explained in terms of a simple antiferromagnetic super exchange interaction between terbium and nearest-neighbour Mn^{4+} ions; similar to $HoMn_2O_5$. At sites 1-2, the net Mn^{4+} dipole field is approximately zero, and so the terbium moments align close to the

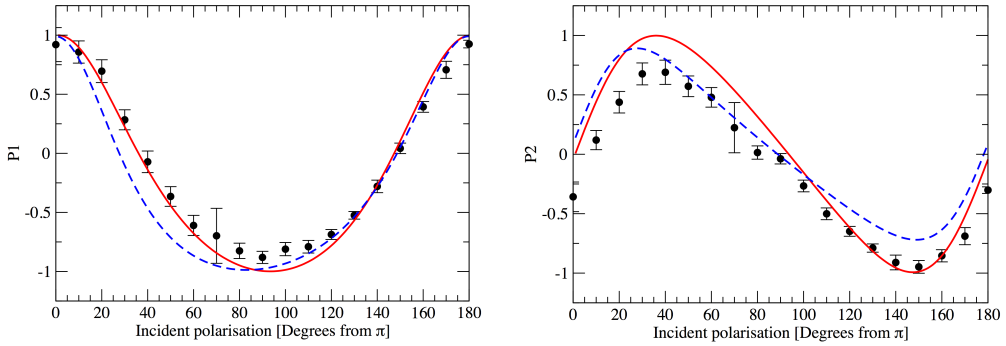

(a) P1 (b) P2

Figure 3.29: A plot of the measured Poincaré-Stokes parameters P1 and P2 as a function of incident x-ray polarisation of the incommensurate (4+δ, 4, 0-τ) reflection at the E2-E2 energy resonance at 2 K. A least squares fit with a reduced χ^2 value of 7.5 is shown in red (solid line). See text for the refined moment directions. The commensurate fit performed in figure 3.28 is shown by the blue dashed line.

magnetic easy axis. At sites 3-4, the net dipole field is strong, and the terbium moments align accordingly. We acknowledge, however, that the actual interactions within the system are likely to be far more complex.

The LT-ICM phase of the $R\mathrm{Mn_2O_5}$ series is less understood, with no complete neutron or synchrotron study of the magnetic structure published to date. Full polarisation analysis performed below 10 K at the E2-E2 transition will refine the moment directions of the terbium ion magnetic order. These can then be compared to those refined in the commensurate phase.

Figure 3.29 shows the Poincaré-Stokes parameters P1 and P2 measured as a function of incident x-ray polarisation at 2 K in the LT-ICM phase. Superimposed is a least-squares fit (red solid line), assuming the same pairing of terbium as in the CM phase. Again the *a* and *b* components of moments on sites 1-2 and 3-4, respectively, were fixed, giving a fit with four degrees of freedom. The refined moment directions on the terbium 1 and 2 sites were $322.0 \pm 4.6^\circ$ in the *ab*-plane relative to the *a*-axis and $0.5 \pm 0.1^\circ$ out of plane, and on the terbium 3 and 4 sites

they were $308.9 \pm 10.4^\circ$ in the *ab*-plane relative to the *a*-axis and $0.6 \pm 0.1^\circ$ out of plane. This refinement of the 2 K terbium sub-lattice magnetic structure results from Tb-Tb ordering below 10 K as predicted [135], as well as interaction with the Mn^{4+} sub-lattice, the magnetic structure of which is unknown in the LT-ICM phase. However, below 10 K the terbium order dominates the bulk magnetisation of the sample [135].

Also plotted as dashed lines in figure 3.28 (CM) and figure 3.29 (LT-ICM) are the LT-ICM and CM fits, respectively. On visual inspection there appears to be little difference between the two fits, particularly when comparing them with the data in figure 3.29. It is surprising then to find that the refinement suggests significantly different spin configurations. The fitting process is clearly sensitive to small changes in the the polarisation dependence and therefore demands high experimental accuracy. This imposes an important limitation of the technique, one that must be considered when interpreting the results. However, due to the small error on the data, we have refined the moment directions with a high degree of precision.

The Mn^{4+} and Mn^{3+} magnetic structures have been shown not to change on substitution of different R^{3+} rare-earth ions in the commensurate phase [73]. This strongly suggests that the manganese ion magnetic structures are responsible for the ferroelectric polarisation in the RMn_2O_5 series. Experimental confirmation that the terbium ions are spin polarised specifically by the Mn^{4+} spin density is therefore of great significance in further understanding of the underlying coupling mechanism, and, by extension, the magneto-electric properties of these compounds.

Probing the terbium ion $4f$ band in the CM and LT-ICM phases at 25 and 2 K, respectively, has provided a direct measurement of the terbium sub-lattice spin configuration in both phases. Importantly, at 2 K we have observed the spontaneous terbium sub-lattice ordering. By assuming a pairing of terbium ions as found by neutron single-crystal data on $HoMn_2O_5$ [130], precise moment directions of the prob-

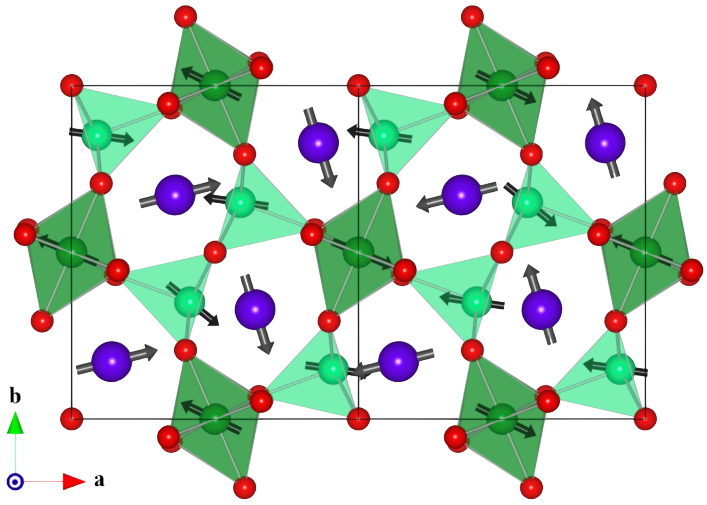

(a) Commensurate

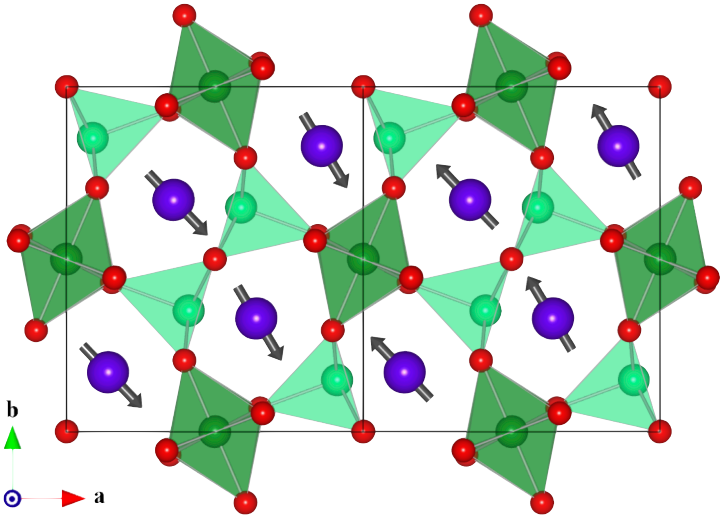

(b) Incommensurate

Figure 3.30: Diagrammatic illustration of the refined terbium ion magnetic moment directions (black arrows) in (a) the CM phase and (b) the LT-ICM phase. There exists a slight component out of the *ab* plane not shown here. The manganese ion magnetic moment directions in the commensurate phase are shown by grey arrows [139]. These directions are currently unknown in the incommensurate phase.

able terbium magnetic structures were found. We observed a change in spin configuration due to a weakening of the terbium ion average magnetisation as expected above 10 K [135], allowing for a stronger interaction with the Mn^{4+} spin density, as shown by the dipolar resonance that probes the $5d$ valence band. Figure 3.30 diagrammatically illustrates the terbium moment directions refined in both the CM and the LT-ICM phases. The moment directions on manganese ions have been omitted in figure 3.30(b) as they are unknown in the incommensurate phase. By visual comparison of the polarisation dependence we observe little change in CM/ICM1 transition; however, when fitting to the data we refine a significant change in spin configuration with precise error bounds. As previously discussed, this illustrates a key limitation of the technique.

3.6 Conclusions

Two energy resonances have been experimentally observed at all four (4, 4, 0) magnetic satellite reflections, one just above the terbium L_{III} edge while the other at 8 eV lower, in both the low-temperature (ICM1) and (CM) phases of $TbMn_2O_5$. The higher energy resonance originates from the E1-E1 dipolar transition, which probes the terbium $5d$ band, and the lower energy resonance originates from the E2-E2 quadrupolar transition, which probes the terbium $4f$ band. The temperature dependence and wave vector measurements confirmed the reflections to be of magnetic origin. Full linear polarisation analysis conducted at the (4+δ, 4, 0-τ) E1-E1 resonance confirmed that the $5d$ band of terbium is polarised predominantly by the Mn^{4+} spin density in the commensurate phase, with an additional interaction with the spin polarised terbium $4f$ magnetic structure. Tuning to the (4+δ, 4, 0-τ) E2-E2 excitation at 2 K (LT-ICM) and fitting to full linear polarisation analysis data enabled the refinement of directions of the spin ordering of the unpaired terbium $4f$ electrons. The measurement and refinement were also performed in the CM phase.

Chapter 4

Antiferromagnetic oxygen ions in $TbMn_2O_5$

4.1 Introduction

Resonant x-ray diffraction (RXD) is only possible when there exists a non-zero transition probability between the two electronic states that coincide with the x-ray absorption edge in question. Therefore, a key requirement is that the final electronic state of the transition is vacant. One might not expect an RXD signal at the oxygen *K*-edge (probing the $2p$ states), as it is often assumed that oxygen atoms will readily form ions with a valency of $2-$, and hence have fully occupied $2p$ states. However such formal valencies are rarely realised. Indeed, a number of RXD studies have provided exciting results through the analysis of resonances measured at the oxygen *K*-edge [161–165].

A soft RXD study by Beale *et al.* [148] set out to investigate the possible existence of such a diffraction signal in $TbMn_2O_5$, which did indeed show a resonance at the oxygen *K*-edge. The resonance was measured in the commensurate (CM) phase at the (0.5, 0, 0.25) magnetic propagation vector, suggesting that not only

do the oxygens have vacant $2p$ states, but also that they carry a net magnetic moment. Further experimental data were collected that conclusively showed that the resonance was indeed of magnetic origin. The temperature dependence of the intensity of the oxygen reflection was shown to coincide with the evolution of the CM magnetism of the manganese ions, measured in the same experiment at the manganese *L*-edges (directly probing their magnetic $3d$ states). Also, a comparison of the azimuthal dependence of the oxygen *K*-edge and manganese *L*-edge diffraction signals showed the two to originate from the same magnetic structure [148]. The existence of the oxygen resonance therefore indicates an antiferromagnetically ordered spin polarisation on the oxygen sites within $TbMn_2O_5$.

Two principal aims arise following this observation. Firstly we must confirm the exact origin of the resonance in order to comment on the significance of such a measurement in the study of transition metal oxides in general. Secondly, we can exploit the detection of the oxygen resonance to investigate the role of the oxygen ions in the formation of the multiferroic phases and the magneto-electric coupling in $TbMn_2O_5$. Such a study could be particularly informative, considering that oxygen magnetism is frequently omitted in magnetic structure determinations and the associated physical interpretations

The behaviour of the oxygen ions is instrumental in the multiferroic properties of $TbMn_2O_5$. This is not only because they mediate the magnetic super exchange interactions that result in the frustrated magnetic structures of the RMn_2O_5 series, but more importantly because the oxygen electron density is intimately linked to the formation of an electric polarisation. The evolution of an ionic polarisation based upon the exchange-striction model was described in section 3.1.2 by the anisotropic next nearest neighbour Ising model. The full picture, however, is not yet complete. The charge transfer between the magnetic ions and the mediating oxygen ligands may be isotropic; resulting in a zero net electric dipole (electronic polarisation),

and hence a dominant ionic polarisation remains. This is illustrated in figure 4.1(a) [100]. However, in the *R*Mn_2O_5 series, the charge order arises from the existence formally Mn^{4+} and Mn^{3+} sub-lattices. The Mn^{4+} ions have three valence t_{2g} electrons that, due to intra-atomic Coulomb interactions, behave as a closed shell with small polarisability. The $3d$ electrons of the Mn^{3+} ions, by comparison, do not have the same crystal field splitting and are readily available to form a dipole bond and hence an electric polarisation [150, 151, 166], as illustrated in figure 4.1(b). In this case, the electric polarisation is almost as large as the ionic polarisation, but in the opposite direction. This gives rise to a small net polarisation, calculated to be in excellent agreement with that measured experimentally in the *R*Mn_2O_5 series [151, 166]. This interpretation also supports the belief that the behaviour of the Mn^{3+} ions is dominant in the evolution of the ferroelectricity [38].

The electric polarisation associated with the Mn-O charge transfer was quantified by Moskvin *et al.* [167]. They show that the polarisation is spin dependent, and defined as,

$$\mathbf{P} = \sum_{ij} \mathbf{\Pi}_{ij}(\mathbf{S}_i \cdot \mathbf{S}_j) \tag{4.1}$$

where $\mathbf{\Pi}_{ij}$ is the effective dipole moment of the transition metal orbital states, $\mathbf{S}_i$ is the spin of the oxygen ligand, and $\mathbf{S}_j$ is the spin of the transition metal ion. Assuming that the RXD signal measured at the oxygen *K*-edge is a signature of an antiferromagnetic, long-range spin polarisation of the oxygen sites, it provides a direct measurement of the magnetism parameterised in equation 4.1; key to the formation of the electric polarisation.

In this chapter we employ the *ab-initio* FDMNES code, described in section 1.4.2, to simulate the oxygen *K*-edge resonance. The electronic origin of the resonance is then discussed through analysis of the density of states of the manganese and oxygen ions, calculated as an intermediate step in the simulation. We also predict the magnitude of the magnetic moments on the oxygen sites that result from

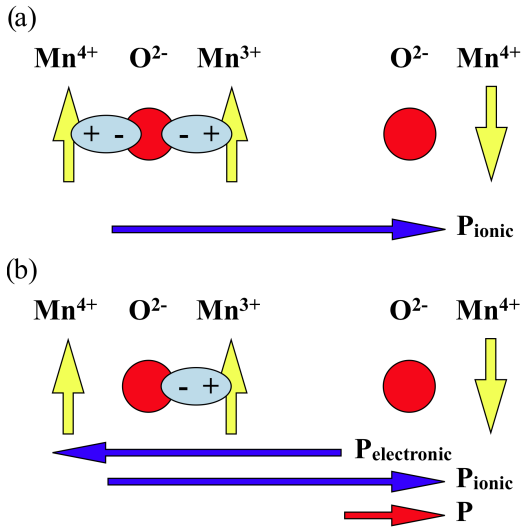

Figure 4.1: The formation of (a) an ionic and zero electronic polarisation, and (b) an ionic and electric polarisation, opposite in direction, resulting in a small net polarisation as measured in the RMn$_2$O$_5$ series.

the spin polarisation. Finally, we investigate the displacement of the Mn^{3+} ions, suggested to give rise to the ionic polarisation, with respect to the intensity of the RXD signal.

4.2 Simulation of the oxygen *K*-edge resonance

The FDMNES calculation was based upon the crystal structure and manganese magnetic structure reported by Blake *et al.* [139]. The terbium magnetic structure was taken from the results of Chapter 3 (Johnson *et al.* [126]), and the oxygen positions from Alonso *et al.* [144]. A magnetic unit cell of 2*a* x *b* x 4*c* was inputted, containing 160 oxygen atoms on 40 inequivalent sites. The computation time of a finite difference method calculation of such a large unit cell was unfeasible, and so the cluster based, multiple scattering mode was used (see section 1.4.2). A cluster radius of 4 Å containing on average 23 atoms was sufficient, with no improve-

ment in the reproduction of the experimental data achieved for larger clusters. For oxygen, the probability of an E2-E2 quadrupole transition between the $1s$ and the $n = 3$ s or d states is negligible, therefore in the calculation we assumed that only the E1-E1 dipole transition contributed to the resonant intensity.

Figure 4.2 shows the x-ray fluorescence spectrum (black circles) of $TbMn_2O_5$, measured by Beale *et al.* [148], through the oxygen *K*-edge. The main edge at approximately 534.5 eV is evident, with two additional pre-edge features at approximately 529.5 and 531.5 eV that originate in the electronic hybridisation of the $2p$ states with neighbouring electron density. The FDMNES calculation is superimposed in figure 4.2 (red line) in which a Fermi level cut-off of 527.7 eV was set (dashed line) in order to properly reproduce the experimental data. The calculation is in excellent agreement with the experimental data, providing a successful initial test of the calculation.

Figure 4.3 shows the oxygen *K*-edge resonance of the (0.5, 0, 0.25) commensurate magnetic reflection [148]. The calculation, again shown by the red line, accurately reproduces the main feature of the energy spectra. The resonance coincides with the dominant pre-edge feature in the absorption curve, and so is likely to originate in the hybridisation of oxygen $2p$ states with the nearest neighbour manganese $3d$ states. We note, however, that the higher energy shoulder and the feature at 531.5 eV are not reproduced by the calculation. We currently cannot explain why this is the case, however we suggest that they also originate in hybridisation between $2p$ and higher energy $3d$ states [168].

4.3 Electronic origin of the resonance

Having shown that our simulation accurately reproduces the experimental data, we now exploit the calculation to find the electronic origin of the resonance. We first perform test calculations to investigate the relative contributions of Mn^{4+} and Mn^{3+}

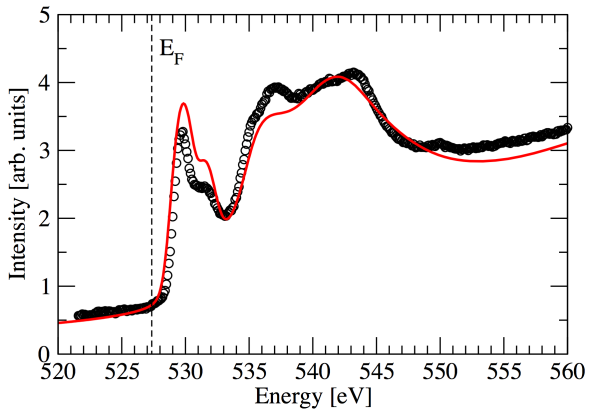

Figure 4.2: The fluorescence spectrum of $TbMn_2O_5$ measured through the oxygen *K*-edge (black circles) [148]. The FDMNES calculation is superimposed (red line), and the Fermi level for the calculation is marked (black dashed line).

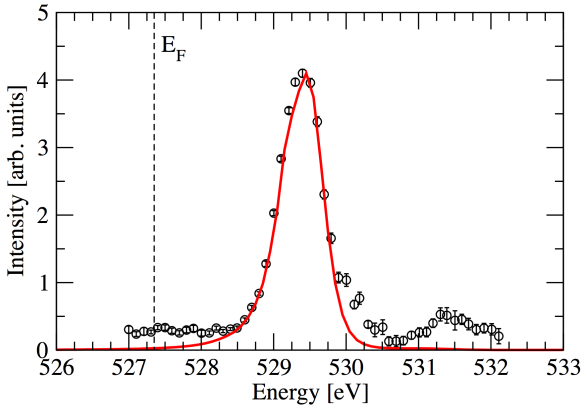

Figure 4.3: The oxygen *K*-edge resonance of the (0.5, 0, 0.25) commensurate magnetic reflection measured by Beale *et al.* [148] (black circles), with the FDMNES simulation superimposed (red line).

hybridisation to the oxygen resonance. Figure 4.4 shows the oxygen *K*-edge energy spectra calculated for $TbMn_2O_5$ with non-magnetic Mn^{4+} ions (red line) and then non-magnetic Mn^{3+} ions (blue line). The resonance calculated with the unmodified magnetic structure is also shown (black line). The magnetism on the manganese sub-lattices was 'switched off' by setting the respective number of up and down spins equal. Upon switching off the Mn^{4+} magnetism, the magnitude of the resonance remains approximately the same. It is surprising to find that the resonance shifts to lower energy, however the calculation is based upon a rather crude manipulation of the true electronic structure. The resonance was completely extinguished when the Mn^{3+} magnetism is switched off. This result clearly suggests that the long-range antiferromagnetic spin polarisation of the oxygen ions measured by the *K*-edge resonance originates in hybridisation solely with Mn^{3+} ions.

To confirm this hypothesis we analysed the average density of states (DOS) of the Mn^{3+} and Mn^{4+} ions, which are outputted from an intermediate step in the FDMNES calculation. Figure 4.5 shows both DOS and the oxygen resonance superimposed. An RXD energy resonance originates in an electronic excitation into available unoccupied electronic states either at an absorption edge, or in the case of hybridisation, in the pre-edge region. Figure 4.5 clearly shows that the only available states above the Fermi level are those of the Mn^{3+} ions. The nearest available Mn^{4+} states are more than 10 eV higher, well above the absorption edge.

The obvious difference between the two manganese sub-lattices, and hence reason for the different oxygen hybridisation characteristics, is the ionisation state. We note, however, that no oxygen *K*-edge resonance has been observed in $TbMnO_3$, in which all manganese ions have a formal valence of $3+$, located within octahedral oxygen coordinations. This indicates that the local geometry (*i.e.* square based pyramid in $TbMn_2O_5$) plays a greater role.

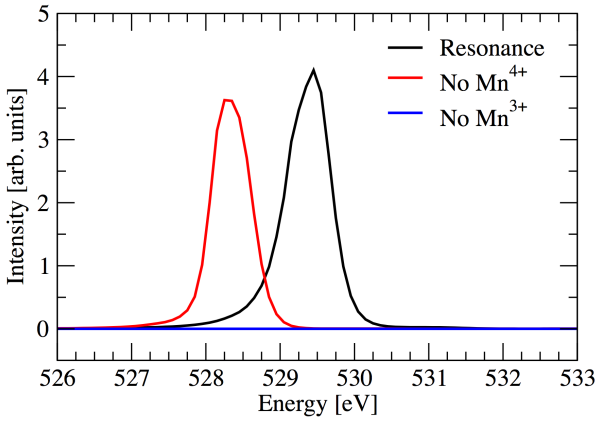

Figure 4.4: The calculated RXD energy spectra at the oxygen *K*-edge with the magnetism switched off on the Mn^{4+} (red line) and Mn^{3+} (blue line) sub-lattices. The original calculation for an unmodified magnetic structure is shown in black.

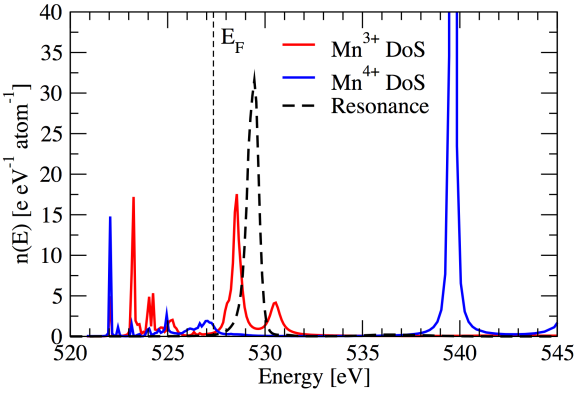

Figure 4.5: The average density of states of the Mn^{3+} (red line) and Mn^{4+} (blue line) sub-lattices. The oxygen *K*-edge energy resonance is superimposed, shown by the black dashed line. The coincidence of the resonance with Mn^{3+} states above the Fermi level confirms the origin of the resonance.

4.4 Density of states analysis - oxygen moments

As explained earlier, the 2*a* x *b* x 4*c* magnetic unit cell contains 160 oxygen atoms located at 40 inequivalent sites. The analysis of individual oxygen ion moments would be impractical. We have therefore simplified the problem by grouping the oxygen ions according to the magnetic exchange interaction that they mediate *i.e.* O1, O2, O3 and O4 (see section 3.2.2) and determining an average magnetic moment. This provides a more useful analysis with greater relevance to the magnetic behaviour of $TbMn_2O_5$.

The average magnetic moment for a given ion may be calculated from the spin up and spin down DOS using:

$$m = \mu_{\mathrm{B}}\left(\int_{-\infty}^{E_{\mathrm{F}}} n_{\uparrow}(E)\mathrm{d}E - \int_{-\infty}^{E_{\mathrm{F}}} n_{\downarrow}(E)\mathrm{d}E \right) \tag{4.2}$$

where E_{F} is the Fermi level, and $n_{\uparrow}(E)$ and $n_{\downarrow}(E)$ are the spin up and spin down DOS, respectively [169, 170]. Figure 4.6 shows the average up (black) and down (red) spin DOS for the four oxygen groups. The calculated magnetic moment magnitudes are shown on the figure. All sites have a significant magnetic moment induced through spin polarisation. The largest average moment occurs on the O4 sites. This is likely to be due to the fact that 50 % of the J3 exchange interactions are ferromagnetic, giving a large net moment at the mediating (O4) oxygen site.

We now look at the oxygen DOS for the two, non-magnetic Mn^{4+} ion and non-magnetic Mn^{3+} ion scenarios, shown in figures 4.7(a) and 4.7(b), respectively. The magnetic structure of $TbMn_2O_5$ is extremely complex, making it very difficult to accurately quantify the behaviour and properties of its components. However, this analysis does enable us to comment on the general contribution of the two manganese sub-lattices to the spin polarisation of the oxygen ions.

The moment at the O1 sites is approximately invariant upon switching on, and

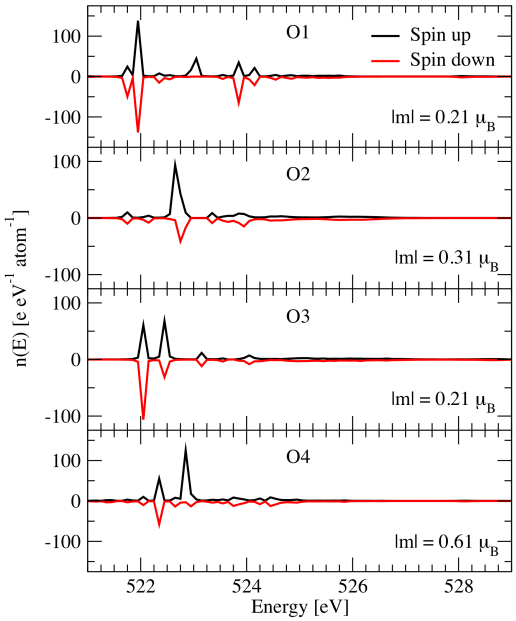

Figure 4.6: The average spin up (black) and spin down (red) DOS for oxygen sites O1, O2, O3 and O4. The magnetic moment magnitudes are shown in the respective panes.

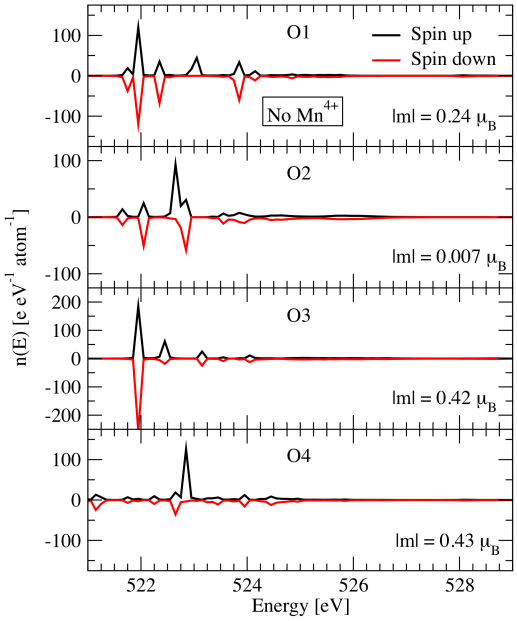

(a)

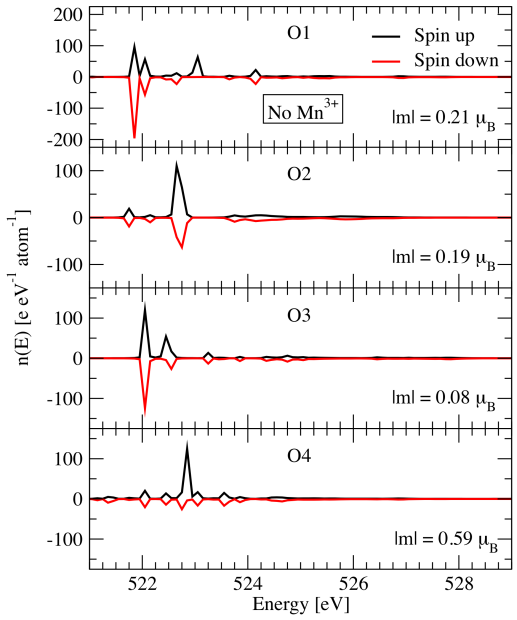

(b)

Figure 4.7: The average spin up (black) and spin down (red) DOS for oxygen sites O1, O2, O3 and O4 with (a) Mn^{4+} ions non-magnetic, and (b) Mn^{3+} ions non-magnetic. The magnetic moment magnitudes are shown in the respective panes.

off, the magnetism of the two manganese sub-lattices. The associated J5 interaction is strongly AFM, with the oxygen ion equidistant between the nearest neighbour (NN) Mn^{3+} ions. The net moment from the manganese spin polarisation will therefore be zero. We suggest that this moment is induced through interaction with the NN terbium ions, which remained magnetic and unchanged in all calculations. The moment on the O2 sites is almost extinguished when the Mn^{4+} sub-lattice magnetism is switched off. The O2 sites are therefore predominantly spin polarised by the NN Mn^{4+} ions in the *c*-axis chains and adopt a moment when J1 is ferromagnetic. We note that the calculated moments do show that Mn^{3+} magnetism also affects this site, but to a lesser degree. The O4 site is shown to remain highly spin polarised throughout the different magnetic configurations. Unfortunately, we do not have sufficient information to comment on its behaviour. Finally, it is apparent that the Mn^{3+} ions show a strong tendency to spin polarise the O3 site, which is then partially quenched by the Mn^{4+} ions that are antiferromagnetically coupled through J4. As the O3 site shows the most dramatic reduction in moment upon switching off the Mn^{3+} magnetism, it is possibly the key to the resonance extinction discussed in the previous section. Furthermore, O3 is the apical oxygen of the square-based pyramids, and so bonds with the Mn^{3+} ion in the direction of the anticipated ferroelectric displacement. The dependence of the oxygen *K*-edge signal on the displacement of the Mn^{3+} ion is discussed in the following section.

4.5 Mn^{3+} displacements

The intensity of the oxygen *K*-edge resonance reflects the magnitude of the Fourier component of the oxygen magnetic structure in the direction of the wave vector. We have calculated the **q** = (0.5, 0, 0.25) resonance, and as such the intensity reflects the degree of antiferromagnetic spin polarisation [148].

The calculation was systematically rerun with modified crystallographic param-

eters, artificially simulating the dependence of the oxygen *K*-edge resonance on the position of the Mn^{3+} ion, displaced along the axis of the surrounding square-based pyramid (shown in figure 4.8). The zero position on the *x*-axis is the empirically determined position from neutron diffraction [38], with the negative direction towards the basal plane. The intensities have been corrected for systematic changes in the structure factor. The figure shows that the scattered intensity, and hence the degree of antiferromagnetic spin polarisation, is highly dependent upon the position of the Mn^{3+} ion. It is possible that the artificial change in magnetic structure also modifies the magnetic anisotropy, hence giving a false dependence of the scattered intensity. However, the azimuthal dependence was calculated at the empirical position and when the ion is in the basal plane, shown in figure 4.9. It is clear that the anisotropy is invariant, and the reduced intensity at the azimuthal maxima simply reflects the intensity change evident in figure 4.8.

We note two important points. Firstly, the empirical position of the Mn^{3+} ion is close to the maximum in figure 4.8, suggesting that the ionic position is stabilised by maximum hybridisation. Secondly, although there is a large dependence on the position of the Mn^{3+} within the square-based pyramid on the sub-Ångström scale, the displacements along this axis predicted in the evolution of ferroelectricity are on the 10^{-3} Å scale. As such, the measurement of the oxygen *K*-edge is insensitive to the elusive ferroelectric displacement, which would not in turn change the oxygen spin polarisation.

4.6 Conclusions

By simulating the oxygen *K*-edge resonance using the *ab-initio* FDMNES code, we have confirmed the origin of the resonance. The magnetism on the oxygen sites giving rise to the resonance is due to antiferromagnetic spin polarisation, specifically through interaction with the Mn^{3+} ions. Furthermore, analysis of the oxygen DOS

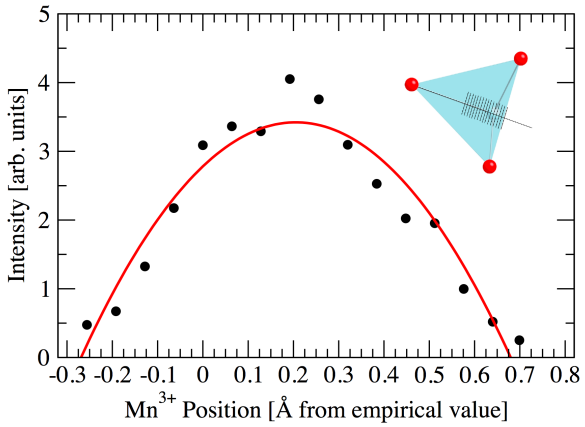

Figure 4.8: The dependence of the resonant intensity on the displacement of the Mn^{3+} ions along the axis of the square-based pyramids (illustrated in the inset, where the atomic positions corresponding to the data points are marked). The red line is a guide to the eye.

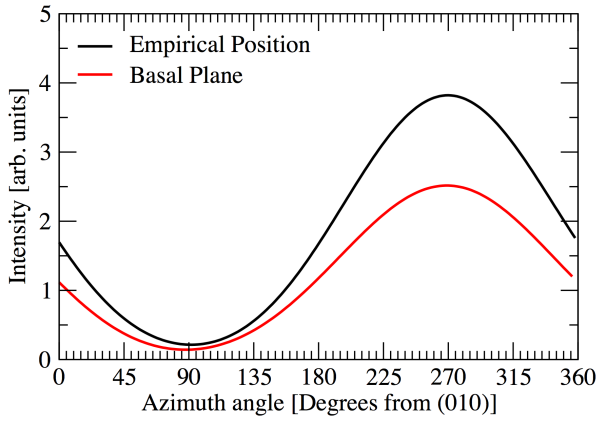

Figure 4.9: The calculated azimuthal dependence on the scattered intensity from the empirically determined magentic structure (black line), and that with the Mn^{3+} ions in the pyramid basal planes (red line).

suggests that the O3 oxygen ions located at the apex of the square-based pyramids display a dominant contribution to the diffraction intensity.

The fact that the resonance is primarily sensitive to the Mn^{3+} - oxygen interaction is of great significance. It is predicted that the electronic hybridisation specifically between these two ion species can give rise to a substantial electric polarisation opposite in direction to the ionic polarisation, and hence account for the small net polarisation experimentally measured in $TbMn_2O_5$. This study shows a large hybridisation between Mn^{3+} and oxygen ions, strongly supporting this argument. The spin dependence of the electric polarisation is parameterised in equation 4.1, in which the polarisation is proportional to the dot product of the Mn^{3+} and oxygen ion magnetic moments. The oxygen magnetism was shown to have the same magnetic anisotropy as the manganese sub-lattices, therefore maximising the dot product, and hence the electric polarisation.

Finally, we investigated the dependence of the resonant intensity on the displacement of the Mn^{3+} ions along the axis of the surrounding square-based pyramids. We showed that the resonance is insensitive to the ferroelectric displacements predicted to be of the order 10^{-3} Å, and so conversely, any such displacement will not affect the antiferromagnetic oxygen spin polarisation.

Chapter 5

Magneto-striction and electric polarisation in $TmMn_2O_5$

5.1 Introduction

In multiferroic, magneto-electric materials an external electric field can couple to the magnetic properties of the system. For example, in $CuCrO_2$ the coercive magnetic field that results in a reversal of the electric polarisation can be tuned by an applied electric field [171], and in $HoMnO_3$ an applied electric field suppresses the antiferromagnetic (AFM) ordering temperature from 72 K to 50 K through interaction with AFM domain walls [172]. An understanding of the magnetic and electric domain structure is important in such materials. In multiferroic $TbMnO_3$ (a cycloidal magnet), an electric field applied parallel to the *c*-axis results in the preferential occupation of either right-handed or left-handed cycloidal magnetic domains, dependent upon the polarity of the field [173, 174]. Not only are such results of great physical interest, their interpretation is key to understanding the magneto-electric coupling in these materials.

In the RMn_2O_5 series it has been hypothesised that magneto-striction causes

small structural displacements (specifically involving Mn^{3+} ions) that result in the electric polarisation [38, 121, 147, 175]. This magneto-electric coupling mechanism is known as the exchange-striction model. Such structural displacements are predicted to be of the order 10^{-3} Å in magnitude [150, 151, 166] and as such are not detectable by standard crystallographic techniques. However, a novel experimental method has been proposed, involving the comparison of the relative intensities of Friedel pairs, that was at least found to be qualitatively sensitive to the displacements [175].

In $DyMn_2O_5$ [176], $TbMn_2O_5$ [147], $HoMn_2O_5$ [127], and YMn_2O_5 [124], the magneto-striction was studied through the measurement of the non-resonant 2**q** x-ray diffraction reflection. This reflection originates in the periodic superstructure modulation due to the magneto-striction that lowers the magnetic energy, where **q** is the magnetic propagation vector. It was found that in $TbMn_2O_5$ the evolution of the commensurate (CM) 2**q** reflection, upon decreasing temperature, coincided with the electric polarisation squared; thus providing evidence that the electric polarisation in the CM phase is indeed generated by lattice modulations. Furthermore, the 2**q** magneto-striction reflection displayed similar behaviour to the magnetic (**q**) reflection, confirming it's origin. The 2**q** reflection was also observed in the ICM1 phase of $TbMn_2O_5$.

The same $TbMn_2O_5$ study [147] also investigated the loss of spontaneous electric polarisation at the CM/ICM1 phase transition; a transition peculiar to the RMn_2O_5 series, discussed in Chapter 3. It was suggested that at this transition, the discommensuration originates in phase slipping occuring between the different magnetic sub-lattices, resulting in anti-phase domain walls separating domains of opposite electric polarisation. In a spherically polarised neutron diffraction study of YMn_2O_5 it was shown that the electric polarisation was indeed associated with distinct antiferromagnetic domains [121]. In this scenario, four different antiferromagnetic

domains may exist in the CM phase, described in detail in section 3.2.3 of Chapter 3. In this scenario, the electric polarisation could be reversed by switching either the small *c*-axis S_z spin component or the large in-plane S_{xy} component, hence switching between domains with opposite electric polarisation. In YMn_2O_5, and indeed the RMn_2O_5 series in general, S_{xy} plays a key role, supporting the exchange-striction model [121]. In YMn_2O_5 it was shown that it was possible to switch 100 % occupation of magnetic domains by cooling into the CM phase in an applied electric field of $\pm$2.2 kV cm^{-1} [121]. Further, it was observed that once the domains had formed in the CM phase they were strongly pinned. Only at temperatures just below the CM phase boundary could the application of an electric field switch domains by a significant percentage.

5.2 $TmMn_2O_5$

In this Chapter we have investigated the behaviour of $TmMn_2O_5$ in applied electric fields, with particular focus on the magneto-striction accompanying the CM phase. In the paramagnetic / paraelectric phase $TmMn_2O_5$ adopts the orthorhombic space group *Pbam*. The lattice parameters determined at 50 K are *a* = 7.206(1) Å, *b* = 8.455(7) Å, and *c* = 5.646(1) Å [177]. The actual symmetry of the low temperature ferroelectric phases in the RMn_2O_5 series is currently unknown, however it is expected to be of lower symmetry, for example the non-centrosymmetric $Pb2_1m$ space group. The first published results on $TmMn_2O_5$ [178, 179] showed, from bulk electric and magnetic measurements, evidence of ferroelectricity parallel to the *b*-axis below 36 K. A further two transitions were observed in dielectric constant measurements at approximately 26 K and 6 K. The 6 K transition was also evident in the magnetic susceptibility data, presented in figure 5.1(a). Furthermore, isothermal magnetometry showed evidence of a metamagnetic transition below 6 K at approximately 0.5 T.

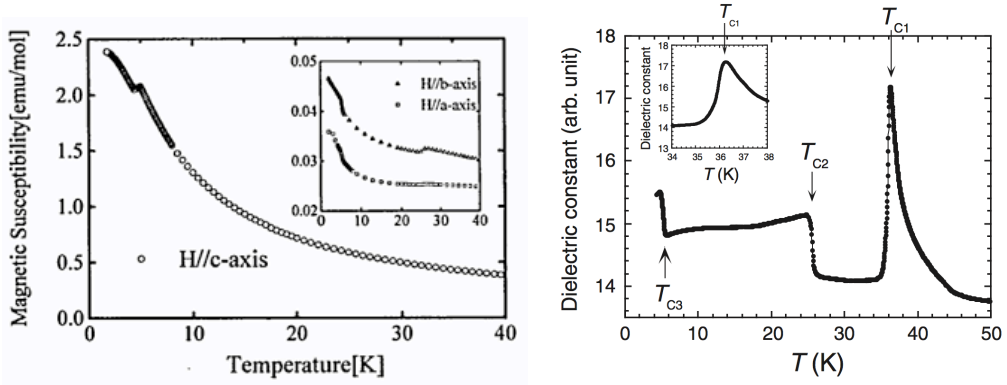

(a) (b)

Figure 5.1: (a) The magnetic susceptibility of $TmMn_2O_5$ measured as a function of temperature along the principal crystallographic directions (*c*-axis in main pane and *a* & *b* axes in inset), reproduced from reference 179. (b) The dielectric constant measured as a function of temperature, showing the electric phase transitions. The figure is reproduced from reference 177, published in the Journal of the Physical Society of Japan.

To investigate the magnetic phases, and hence the multiferroic nature of $TmMn_2O_5$, single crystal neutron experiments were performed [177] from which the low temperature phase diagram, reproduced in figure 5.2, was determined. In common with the *R*Mn_2O_5 series, $TmMn_2O_5$ undergoes a number of concomitant magnetic and electric phase transitions. Dielectric constant measurements, shown in figure 5.1(b), were used to determine the ferroelectric transitions (upper part of figure 5.2) [177]. Similar to YMn_2O_5, the sharp anomaly at $T_{C1} = 36.4$ K marks the onset of spontaneous ferroelectricity. The step at $T_{C2} = 24.9$ K then indicates the onset of a weak ferroelectric phase. Different to YMn_2O_5 (in which yttrium is non-magnetic) is the feature at 4.8 K at which temperature the electric polarisation along the *b*-axis disappears. This transition is unique to $TmMn_2O_5$ and is strongly coupled to the ordering of the thulium moments, as discussed later in this section. The neutron diffraction gave the following magnetic transitions. At $T_{ICM2} = 44$ K, 2-D incommensurate (ICM) magnetic order develops with propagation vector **q** = (0.474, 0, 0.252). Upon

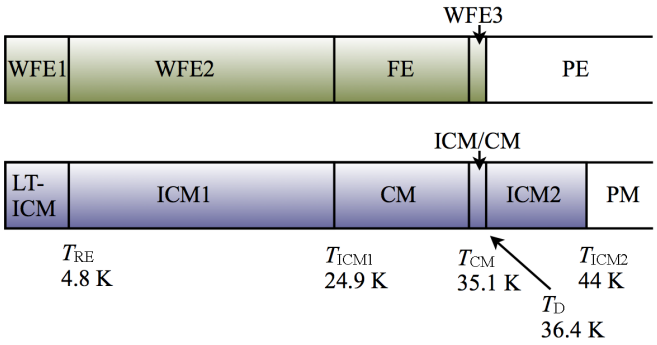

Figure 5.2: The low temperature phase diagram of $TmMn_2O_5$ based on that reported in references 177 and 136.

cooling, the *l* component of the magnetic propagation vector tends to $\frac{1}{4}$, where at $T_{\mathrm{D}} = 36.4$ K there coexists 1-D ICM, **q** = (*h*, 0, 0.25), and commensurate (CM), **q** = (0.5, 0, 0.25), magnetic orders. At $T_{\mathrm{CM}} = 35.1$ K, the CM phase locks in and the 1-D ICM phase disappears. Unusually the RMn_2O_5 series adopts an ICM ground state, which in $TmMn_2O_5$ occurs at $T_{\mathrm{ICM1}} = 24.9$ K with propagation vector **q** = (0.473, 0, 0.272). At $T_{\mathrm{RE}} = 4.8$ K, the rare-earth sub-lattice orders, resulting in a dramatic increase in the magnetic correlation along the *c*-axis and a significant rearrangement of the manganese magnetic structure. This low temperature incommensurate phase is labelled LT-ICM.

The simultaneous magnetic and ferroelectric transitions provide clear evidence of magneto-electric behaviour in this material. The magneto-electric coupling was investigated in detail in a second neutron diffraction study with *in-situ* electric polarisation measurements along both *b* and *a* axes [136]. Figure 5.3 summarises the results of the *in-situ* measurement. The remnant *b*-axis electric polarisation was determined by measuring $D(t)$ vs. $E(t)$ hysteresis loops with a Sawyer-Tower circuit with a driving 20 Hz sinusoidal waveform. The polarisation magnitude is artificially low as the hysteresis loops did not fully saturate. The behaviour of the electric polarisation is in agreement with the phase diagram described above, with the electric

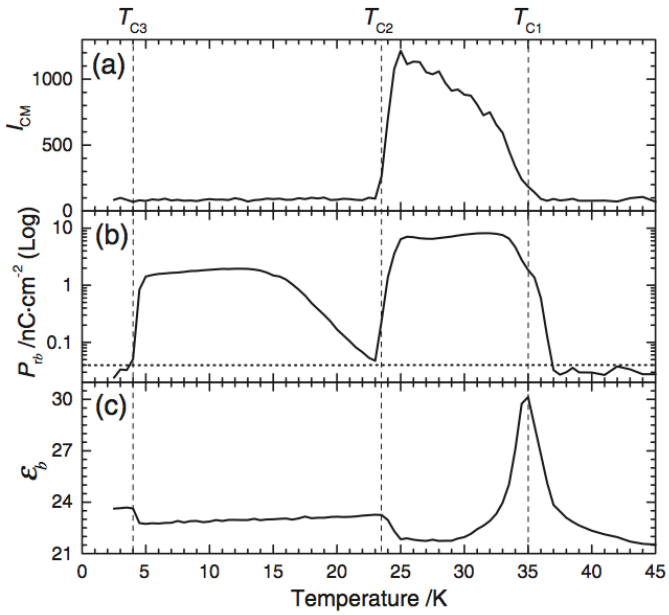

Figure 5.3: The results of an *in-situ*, simultaneous electric polarisation and neutron diffraction measurement. (a) The integrated intensity of the (0.5, 0, 0.25) CM magnetic neutron diffraction peak. (b) The remnant electric polarisation measured along the *b*-axis. (c) The dielectric constant, replicating the data shown in figure 5.1(b). The figure is reproduced from reference 136, published in the Journal of the Physical Society of Japan.

polarisation evolving at T_{D}, disappearing at T_{ICM1}, and then re-emerging in the weak ferroelectric phase (note the scale in figure 5.3b is logarithmic).

Pyroelectric measurements gave two interesting results [136]. Firstly, the data were found to be antisymmetric with respect to the polarity of the polling electric field, suggesting that the sample had a tendency to polarise in a given direction. Secondly, the polarisation induced by applying a static electric field in the CM phase does not remain upon field cooling into the ICM1 phase. However, the polarisation induced by an applied field in the ICM1 phase does remain when the sample is field warmed into the CM phase.

The major result of reference 136 was the discovery of a polarisation flop (rota-

tion of 90° from the *b*-axis to the *a*-axis) at T_{RE}. This is one of only two examples of an electric polarisation parallel to the *a*-axis in the *R*Mn_2O_5 series. Figure 5.4(a) shows the ICM1 / LT-ICM transition at 4.8 K and the simultaneous electric polarisation flop. It is interesting to note the equivalent $\mathbf{q}_{\mathrm{z}}$ values in both phases, except for the divergence during the 0.3 K phase coexistence at the transition. Analysis of magnetic neutron diffraction signals confirmed a substantial rearrangement of the magnetic structure at T_{RE}, despite maintaining equivalent propagation vectors. It was proposed that $TmMn_2O_5$ is in fact ferrielectric, with a ferroelectric coupling along the *b*-axis and an antiferroelectric coupling along the *a*-axis above T_{RE}. This scenario would then switch, becoming antiferroelectric along the *b*-axis and ferroelectric along the *a*-axis below T_{RE}.

The original magnetometry data of reference 179 showed a metamagnetic transition at an applied field of approximately 0.5 T, applied parallel to the *c*-axis in the LT-ICM phase. In $TbMnO_3$, the electric polarisation flops from P $\parallel$ *c*-axis to P $\parallel$ *a*-axis in an applied field $\parallel$ *b*-axis of approximately 5 T [106]. It was supposed, therefore, that a polarisation flop from P $\parallel$ *a*-axis, back to P $\parallel$ *b*-axis could be the origin of the metamagnetic transition in $TmMn_2O_5$. This was indeed shown to be the case, as summarised in figure 5.4(b) [137].

By comparison with the behaviour of other members of the *R*Mn_2O_5 series [135, 180], it is apparent that the most dramatic magneto-electric effects occur when the applied field is in the direction of the rare-earth sub-lattice easy axis of magnetisation. Further, the polarisation flop in $TmMn_2O_5$ occurs at comparatively low fields of 0.5 to 0.6 T. In $TbMn_2O_5$ the polarisation reversal occurs at 2 T [135], and the polarisation flops in $TbMnO_3$ and $MnWO_4$ occur at 5 T and 10 T, respectively [106, 108].

As discussed in Chapter 3, there are two main microscopic mechanisms proposed for the magneto-electric coupling in *R*MnO_3 and *R*Mn_2O_5 multiferroics. The

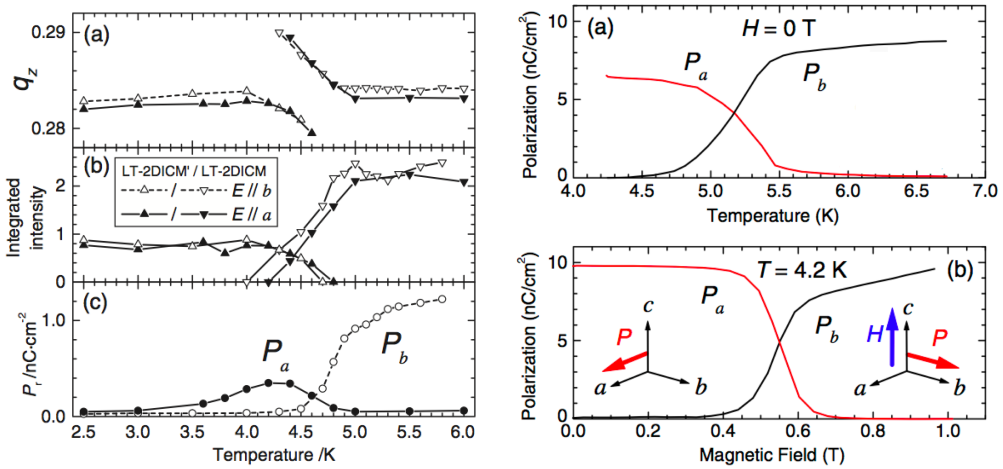

(a) (b)

Figure 5.4: (a) The magnetic wavevector, scattered magnetic intensity and electric polarisation temperature dependence through the spin flop transition at 4.8 K. The figure is reproduced from reference 136, published in the Journal of the Physical Society of Japan. (b) The magnetic field induced polarisation flop in the ICM1 phase of $TmMn_2O_5$. Reprinted figure with permission from reference 137. Copyright 2009 by the American Physical Society.

first, prominent in the *R*MnO_3 series, involves the antisymmetric Dzyaloshinsky-Moriya exchange interaction ($\mathbf{S}_i \times \mathbf{S}_j$) described in section 1.2. The second, exchange-striction mechanism, involves the more direct $\mathbf{S}_i \cdot \mathbf{S}_j$ type interaction. In $TmMn_2O_5$ it is impossible for the exchange-striction mechanism to be responsible for the polarisation flop as no change was observed in either the crystal structure or magnetic propagation vector. It was suggested that spiral chains of Mn^{4+} moments stack with anti-phase chirality in the *ac*-plane and with in-phase chirality in the *bc*-plane. Assuming $\mathbf{S}_i \times \mathbf{S}_j$ exchange, this would give rise to a ferrielectric order polarised along the *b*-axis. If the chirality of one Mn^{4+} chain was to reverse, the electric polarisation would flop from the *b*-axis to the *a*-axis [137]. The exchange-striction model would therefore only be valid in the commensurate phase, adding to the polarisation already present in the ICM1 phase, induced by the $\mathbf{S}_i \times \mathbf{S}_j$ interaction.

In this experiment we measured the CM (0, 0, 0.5) type, $2\mathbf{q}$ magneto-striction x-ray diffraction signals, simultaneously with the electric polarisation, as a function of temperature through the multiferroic phases of $TmMn_2O_5$. From the results, we discuss the onset of magneto-striction with respect to the development of the electric polarisation; important in the context of possible magneto-electric mechanisms in the *R*Mn_2O_5 series. We also investigated the effect of applied DC electric fields on the magneto-striction diffraction signals; the reverse coupling.

5.3 Experiment

5.3.1 Sample preparation

To determine the electric polarisation of the sample in the low temperature multiferroic phases it was necessary to apply electric fields, as described in section 5.3.2. Fine sample preparation is crucial in accurately quantifying, and ensuring uniformity of, the applied electric field. Furthermore, the sample had to be prepared for

simultaneous synchrotron x-ray diffraction measurements.

A high quality single crystal of $TmMn_2O_5$ was grown by the PbO-PbF_2 flux method [181] at the Institute of Multidisciplinary Research for Advanced Materials, Tohoku University, Sendai, Japan. A surface with the crystallographic *c*-axis surface normal was cut and polished for diffraction. As such, 2**q** magneto-striction satellite reflections about (0, 0, 1) type Bragg reflections were investigated in the synchrotron experiment. Two faces were then cut for the electrodes, such that the electric field was applied parallel to the *b*-axis; the direction of the electric polarisation in the CM phase. The sample was mounted on a sapphire disc to electrically insulate it from the copper cold finger of the cryostat, yet still maintain reasonable thermal conductivity. The sample and disc were masked with candle wax, exposing only the electrode surfaces upon which a 100 nm layer of gold was then evaporated. The evaporated gold contacts ensure a uniform charge density across the sample surface where silver paint contacts, for example, might not. Figure 5.5(a) shows the sample mounted on the sapphire disk, de-masked, with gold contacts. The dimensions of the sample are crucial in the electric polarisation calculations described in section 5.3.2. The two gold contacts had surface areas of 1.21 $\pm$0.02 mm^2 and 1.71 $\pm$0.02 mm^2. The width between the contacts, determining the magnitude of the electric field for a given voltage, was 1.26 $\pm$0.01 mm. Kapton insulated copper wires were bonded to the gold contacts using silver paint and anchored to the sapphire disc with epoxy glue, as shown in figure 5.5(b).

5.3.2 Electric polarisation measurements

The aim was to measure ferroelectric $P(t)$ vs. $E(t)$ hysteresis loops, from which the remnant electric polarisation of the sample could be directly read. The experimental setup is schematically illustrated in figure 5.6. An oscillating voltage of amplitude $\pm$ 10 V was generated by a TTi instruments TGA1240 signal generator, capable of

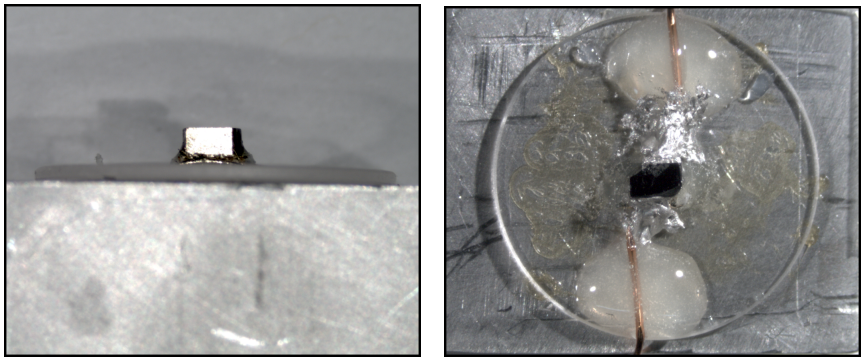

(a) (b)

Figure 5.5: The $TmMn_2O_5$ single crystal with (a) evaporated gold contact, mounted on a sapphire disk, and (b) the copper wires silver painted to the gold contacts and anchored with epoxy glue.

outputting either a square, triangular or sinusoidal waveform. The signal was then inputted into a TREK 610 E high voltage (HV) amplifier with a gain of 1000:1, the output of which was wired to one sample electrode. The time base and output voltage was monitored and logged by a high speed, MUSST data acquisition card. This card has been developed at the European Synchrotron Radiation Facility, and was used as a triggered analogue to digital converter that also records a time stamp for every data point. A Stanford SR570 current-voltage amplifier was used to measure the current at the other sample electrode. The amplifier has sensitivity settings from 1 $pA.V^{-1}$ to 1 $mA.V^{-1}$. In this experiment the sensitivity was set to 200 $\mu A.V^{-1}$. The voltage output of the current-voltage amplifier was then simultaneously logged by the data acquisition card.

The current may spike due to arcing across the sample surface or through the breakdown of otherwise insulating components. In order to protect the current-voltage amplifier from such a spike, two antiparallel Zener diodes were used between the current electrode and ground.

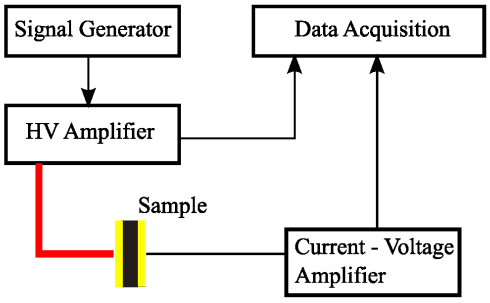

Figure 5.6: Experimental setup used to measure $P(t)$ vs. $E(t)$ hysteresis loops.

5.3.3 X-ray diffraction with *in-situ* electric field

The sample was mounted on the cold finger of a closed-cycle ^{4}He cryostat, fitted to the diffractometer at BM28 (XMaS) [182] at the European Synchrotron Radiation Facility. The diffractometer was set in 4-circle mode with a vertical scattering geometry. The cryostat provided stable sample temperatures down to 8 K. Furthermore, the cryostat had been wound with high voltage cables, rated up to 10 kV. Figure 5.7(a) shows the mounted sample and the high voltage connections. The sample was orientated such that when θ and $\phi = 0$, the a-axis was parallel to the x-ray beam and the b-axis was perpendicular to the scattering plane. This geometry is illustrated in figure 5.7(b).

Beam line BM28 is located on a bending magnet x-ray source, providing an incident x-ray energy range of 2.3 to 15 keV. Similar to ID20 (section 3.4.1), the energy is tuneable via a double bounce silicon (1, 1, 1) monochromator. Importantly, BM28 provides efficient harmonic rejection by employing a pair of palladium coated pyrex mirrors. The harmonic contamination originates in higher order reflections of the silicon monochromator, *i.e.* (2, 2, 2), (3, 3, 3) etc. In this experiment we studied (0, 0, 0.5) type reflections that would, without harmonic rejection, be obscured by the more intense (0, 0, 1) Bragg reflection scattering second harmonic energies.

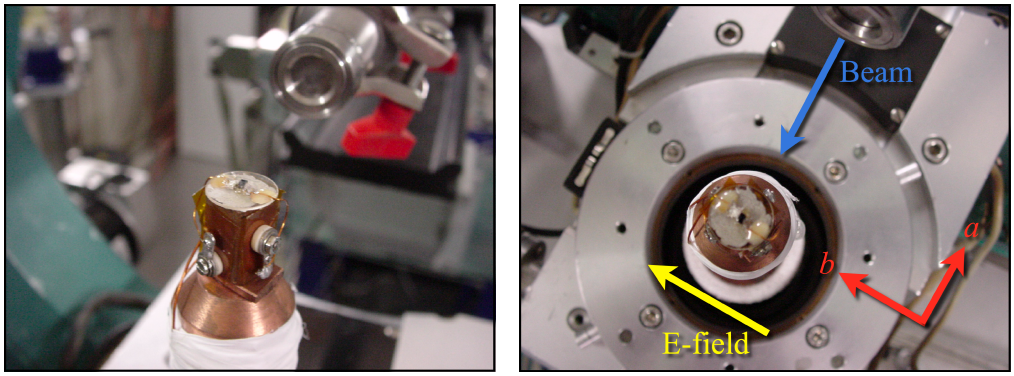

(a) (b)

Figure 5.7: (a) The $TmMn_2O_5$ sample mounted on the cryostat at BM28 with the incident beam tube in close proximity. (b) The crystallographic orientation of the sample (red) with respect to the x-ray beam (blue) and electric field (yellow).

The 2**q** magneto-striction reflection originates in a structural modulation of the crystal lattice. The diffraction peak is therefore essentially a weakly allowed Bragg reflection and as such the anomalous terms of the cross section do not contribute to the diffraction; *i.e.* no resonant enhancement is expected. We therefore require an incident x-ray energy well below the rare-earth absorption edge, in order to minimise the fluorescence background. The sample fluorescence was measured through the thulium L_{III}-edge at approximately 8.65 keV (figure 5.8), again to check that the x-ray beam was incident on the sample, and to choose a suitable energy (8.6 keV) for the following study. At this energy, a copper polarisation analyser crystal scattering at the (222) reflection was employed to further reduce the background.

5.4 Results and Discussion

5.4.1 Magnetometry

In order to characterise the $TmMn_2O_5$ sample used in this study and to enable comparison with those reported in the literature [136, 137, 177, 179], the magnetic sus-

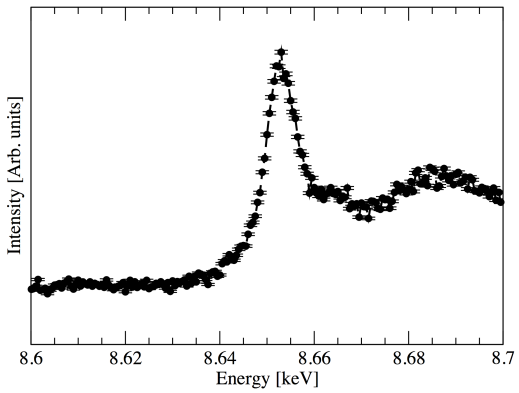

Figure 5.8: Fluorescence spectrum of $TmMn_2O_5$ measured through the thulium L_{III}-edge.

ceptibility was measured as a function of temperature. A Quantum Design MPMS was employed, as described in section 2.4. Measurements were made in the *c*-axis direction on warming, having zero field cooled the sample. Two data sets were collected in external magnetic fields of 100 Oe and 30000 Oe, respectively. The data is shown in figure 5.9.

As is the case with many rare-earth-transition-metal oxides, the magnetisation is dominated by the large magnetic moments of the relatively soft rare-earth sublattice. As a consequence it was not possible to observe the ordering of the manganese ion moments above T_{RE}. However, the rare-earth ordering transition at T_{RE} = 4.8 K was clear, particularly in the derivative of the susceptibility shown in the inset of figure 5.9. The value of T_{RE} observed agrees well with that reported in the literature. Furthermore, the trend of the magnetic susceptibility accurately reproduces the magnetisation measurement in reference 179, shown in figure 5.1(a).

5.4.2 *P*(*t*)-*E*(*t*) loop analysis

The high voltage (HV) was oscillated with a sinusoidal waveform between ± 2 kV at a frequency of 20 Hz. With a sample thickness of 1.26 mm, 2 kV gave an electric

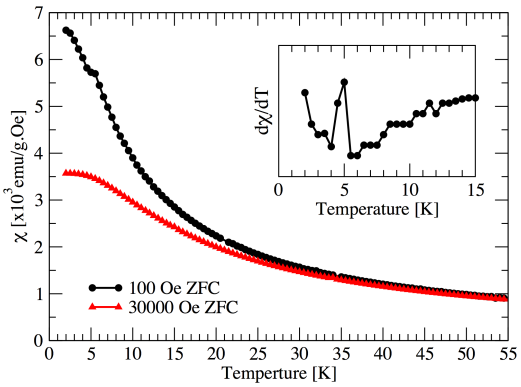

Figure 5.9: Magnetic susceptibility of $TmMn_2O_5$ measured, after zero field cooling (ZFC), along the *c*-axis in an external field of 100 Oe (black circles) and 30000 Oe (red triangles). The inset gives the derivative of the 100 Oe susceptibility data, clearly showing the rare-earth ordering at 4.8 K.

field across the sample of approximately 16 kV cm^{-1}. The results in reference 136 indicate that this should be sufficient to saturate the resultant $P(t)$ vs. $E(t)$ hysteresis loops. With a frequency of 20 Hz, a large number of $V(t)$ vs. $I(t)$ loops could be measured in a relatively short period of time. In this experiment 100 cycles were performed. These repeated loops were then binned, giving a statistical averaging, and hence an improvement in the quality of the $I(t)$ data. The virgin section of the hysteresis loop was omitted in the data binning. Figure 5.10(a) shows 4 of the 100 cycles. Both the driving voltage (black) and the measured current (red) are plotted as a function of time. Figure 5.10(b) then shows the data binned into a single cycle. The improvement in data quality is clear.

The charge stored by the sample was then found by cumulative numerical integration of the measured current as a function of time, *i.e.*

$$Q(t) = \int_{t_0}^{t} I dt \tag{5.1}$$

where Q is the charge and I is the current. The dielectric displacement was then

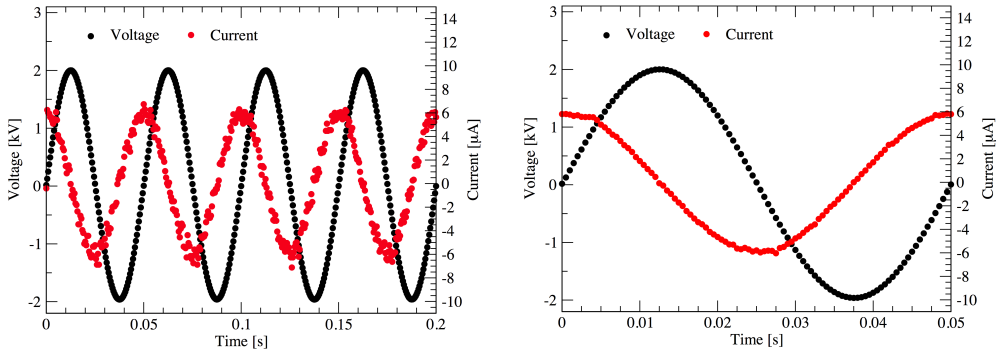

Figure 5.10: An example of (a) the raw (4 out of 100 cycles), and (b) the binned, $V(t)$ and $I(t)$ data, measured at 32 K in the centre of the ferroelectric phase.

found by dividing by the cross-sectional area over which the electric field was applied,

$$D(t) = \frac{Q(t)}{A} \tag{5.2}$$

where D is the dielectric displacement and A is the cross-sectional area. The sample had electrodes of similar, but unequal, surface areas. The surface areas were therefore averaged to approximate the cross-sectional area of the applied electric field. Figure 5.11(a) shows the resultant $D(t)$ vs. $E(t)$ hysteresis loop. It was found that the data was dominated by a clockwise inductance loop almost two orders of magnitude larger than the ferroelectric response. The inductance was likely to originate in the cryostat HV windings. This clockwise inductance signal was treated as a background. It was determined from $D(t)$ vs. $E(t)$ loops calculated in the paraelectric phase and then subtracted from the data. After subtraction of the background, the anticlockwise ferroelectric hysteresis loop was evident, as shown in figure 5.11(b).

The electric polarisation of the sample is related to the dielectric displacement by correcting for the applied electric field:

$$P(t) = D(t) - \epsilon_0 E(t) \tag{5.3}$$

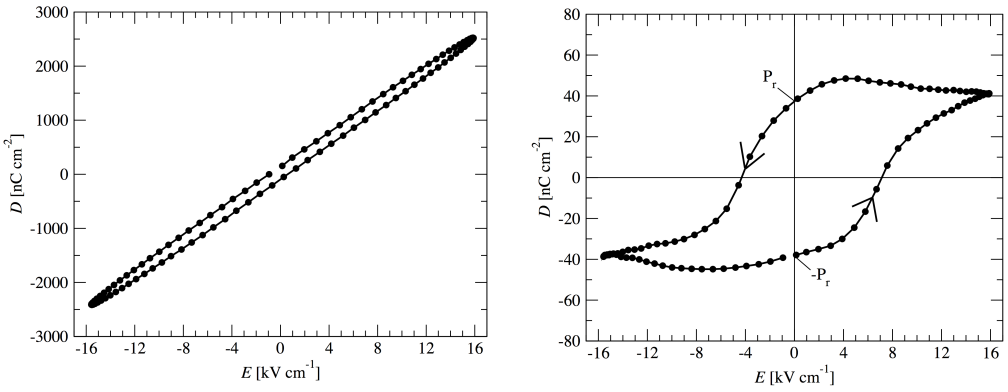

(a) (b)

Figure 5.11: (a) The $D(t)$ vs. $E(t)$ loop calculated from the 32 K data given in figure 5.10(b). The loop is dominated by an inductance background which has been subtracted in (b), showing the ferroelectric hysteresis loop.

where E is the applied field and ϵ_0 is the permittivity of free space. In general, we define the sample polarisation as the remnant polarisation of the hysteresis loop, following reference 136. For continuously measured loops it is not possible to define the D = 0 position and hence fix the y-axis. The remnant polarisation is therefore determined as half the hight of the loop at E = 0. The $\epsilon_0 E(t)$ term in equation 5.3 can be ignored (as E = 0) and we needed only treat $D(t)$ vs. $E(t)$ hysteresis loops in the final data analysis.

In the following section the electric polarisation measurements were performed as a function of temperature. Figure 5.12 shows initial off-line measurements of $D(t)$ vs. $E(t)$ loops as a function of temperature, through the ferroelectric phase. The evolution and extinction of the ferroelectric hysteresis and remnant polarisation is clear across the temperature range.

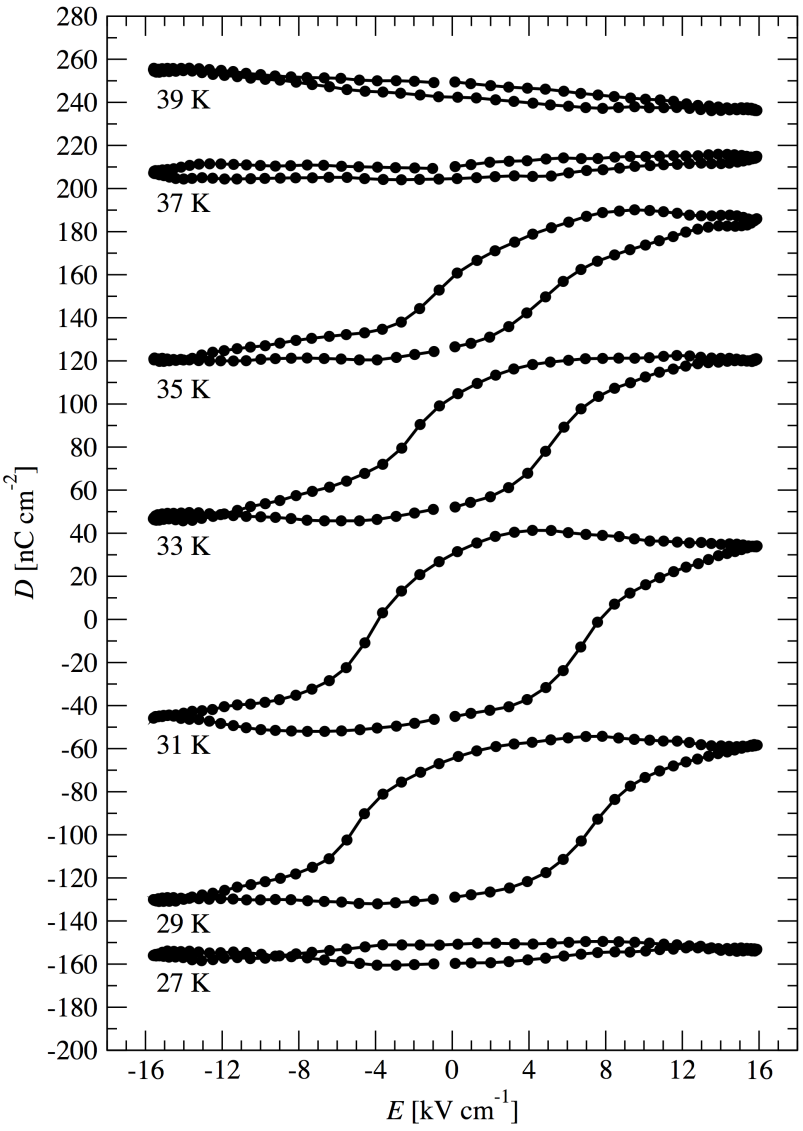

Figure 5.12: Initial off-line measurements of $D(t)$ vs. $E(t)$ loops as a function of temperature through the ferroelectric phase. The loops have been arbitrarily shifted along the *y*-axis for clarity.

5.4.3 X-ray diffraction

The sample was cooled to 29 K; well within the ferroelectric, CM phase. Having aligned the sample through locating structural Bragg reflections, a number of CM superlattice 2**q** satellite reflections (**q**=(0.5, 0, 0.25)) were located, namely the (0, 0, 2.5), (0, 0, 3.5), (0, 0, 4.5), and (0, 2, 4.5). As described in section 5.1, these reflections originate in the structural modulation due to magneto-striction, and their intensities reflect the respective Fourier component of the modulation. Due to strict time constraints, we continued to study only the (0, 0, 4.5) reflection, chosen for it's clean and intense signal.

It was not possible to find the (0, 0, 4.5) 2**q** magneto-striction reflections in the ICM1 phase; as according to extinction rules [118]. Furthermore, it was also not possible to observe any magnetic satellite reflections at **q** satellite positions in the CM or the ICM1 phase, at either the thulium L_{III} or at the manganese K, edges. It is not surprising that a magnetic diffraction signal at a transition metal K-edge be too weak to observe. Also, by comparison with other rare-earth magnetic RXS signals, the thulium resonance is expected to be weak [183].

Figure 5.13 shows a scan of the scattered intensity in the high resolution l reciprocal space direction. As in $TbMn_2O_5$ (section 3.5.1) the reflection has been fitted in order to gain an indication of the correlation within the sample, shown by the red line in figure 5.13. A Lorentzian squared profile best describes the diffraction peak broadening that originates in the limited extent of the electronic correlations within the sample. However, if the width of the reflection is limited by the instrumental resolution one expects a Gaussian peak profile. The peak is well reproduced in the former case through fitting a Lorentzian squared profile, suggesting that the peak width is determined by the sample correlation and not the instrument. The substantial background due to unwanted broad diffuse scattering has also been fitted with a Gaussian line shape. Using equations 3.4 and 3.5, a correlation length

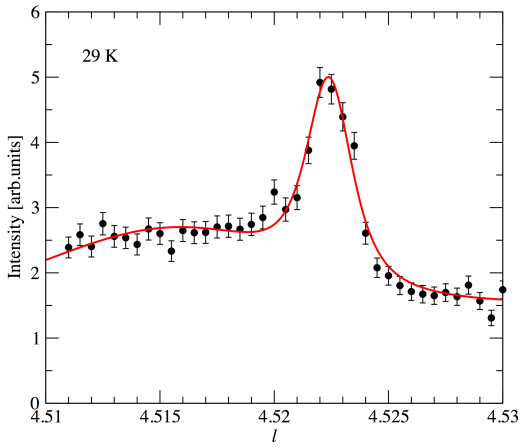

Figure 5.13: Scan of the scattered intensity of the (0, 0, 4.5) reflection measured in the l direction at 29 K. The reflection is fitted with a Lorentzian squared profile, and the background with a Gaussian and constant offset; both shown by the red line.

of 993 $\pm$112 Å was calculated, showing the sample to be strongly correlated. The large error is due to inaccuracies in the fit from the Gaussian background.

We note a substantial deviation in l from the expected value of 4.5. We believe this to be due to inaccuracies in the crystal alignment, however the reflection was investigated to confirm that it was indeed a 2**q** superlattice reflection, as opposed to a spurious artifact. Firstly, it was confirmed that the reflection only exists in the expected temperature range, shown clearly by the temperature dependence presented later in this Chapter (figure 5.15). Secondly, it was confirmed that the reflection only existed in the unrotated $\sigma - \sigma'$ polarisation channel; characteristic of a diffraction peak originating in a structural modulation. Finally, the energy dependence of the reflection was measured, shown in figure 5.14. With increased absorption at the thulium L_{III}-edge and the absence of a resonance, the energy dependence is comparable to that expected of structural Bragg reflections, showing that the reflection was indeed of isotropic structural origin.

In order to investigate the relationship between the magneto-striction and elec-

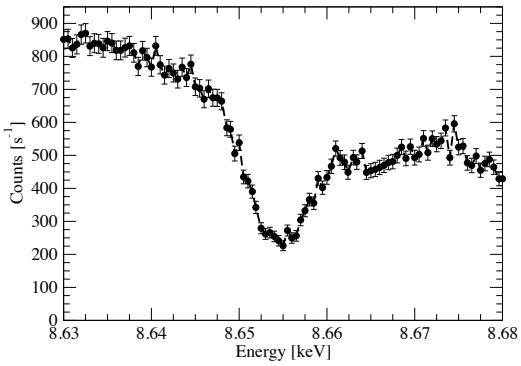

Figure 5.14: Scan of the scattered intensity of the (0, 0, 4.5) reflection measured as a function of energy. The 'Bragg like' line shape, showing greater absorption through the edge and no resonant component, confirms the reflection to be of isotropic structural origin.

tric polarisation, the (0, 0, 4.5) reflection intensity and $D(t)$ vs. $E(t)$ hysteresis loops were measured simultaneously as a function of temperature, (figure 5.15). The electric polarisation data measured *in-situ* was of lesser quality than that previously measured offline. However, the transitions of the electric polarisation were observable and equivalent. For this reason, we present the offline data in figure 5.15 to give greater clarity. The transition temperatures measured in this experiment were uniformly found to be approximately 2 K lower than those given in the literature [136, 177]. This is to be expected in a synchrotron experiment due to beam heating and the difficulties in locating the temperature sensor close to the sample. Indeed, in the $TbMn_2O_5$ experiment discussed in Chapter 3, the same 2 K difference was observed. For clarity, all the temperatures presented in this Chapter have been corrected accordingly.

The red data points in figure 5.15 show the integrated intensity of the CM magneto-striction reflection as a function of temperature. The intensity of the reflection, corrected for fluctuations in the incident beam intensity and normalised to unity, follows a similar trend to the magnetic signals measured by neutron diffrac-

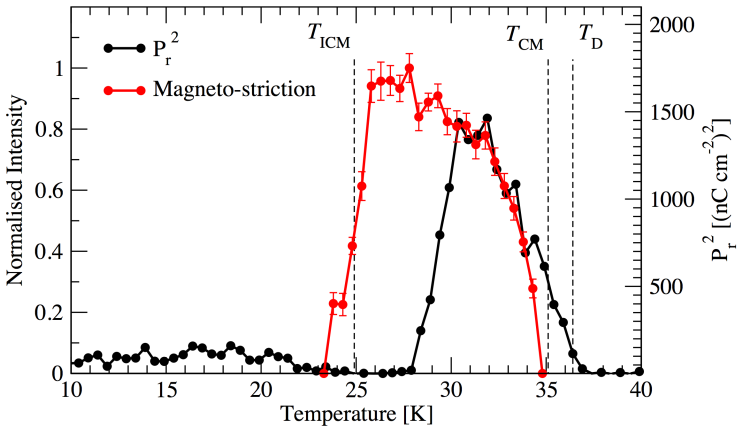

Figure 5.15: The intensity of the magneto-striction reflection (red) and the remnant electric polarisation (black), measured as a function of temperature through the low temperature phases (dashed lines) of $TmMn_2O_5$. The electric polarisation is squared for comparison with the intensity.

tion [136]. The correlation length and the peak position in reciprocal space (both not shown here) were also measured and found to be constant as a function of temperature.

On cooling, the remnant electric polarisation develops at T_{D}; the onset of the WFE3, CM/ICM phase transition. In figure 5.15 the remnant polarisation squared is plotted, as in general one would expect the scattered intensity to scale with the associated order parameter squared. The polarisation continues to increase upon the CM magnetic ordering, simulataneously with the magneto-striction at T_{CM}. The magnitude of the electric polarisation was found to be comparable to that reported in reference 136. In contrast to the behaviour reported in reference 136, the electric polarisation is observed to decrease down to zero at 28 K; 3 K above the T_{ICM1} transition. Upon further cooling the polarisation then increases, as expected, into the ICM, WFE2 phase. The magneto-striction in the 3 K region above T_{ICM1}, in which the electric polarisation is zero, exhibits an interesting DC electric field dependence discussed later in this section.

The electric polarisation data was found to be repeatable and equivalent on both cooling and warming, showing no thermal hysteresis. The effects of electric field cooling (FC) the sample on the magneto-striction was also investigated. Compared to the zero electric field cooled (ZFC) data, no change was observed in the 2**q** temperature dependence in either ± 16 kV cm^{-1} applied electric fields.

So far we have investigated the multiferroic existence of both magneto-striction and ferroelectric polarisation. We now look more closely at the magneto-electric coupling between the electric field and magneto-striction. The dependence of the magneto-striction reflection on static (DC) applied electric fields of ± 16 kV cm^{-1} was measured above and below T_{CM} (37 K, and 34 K), above and below T_{ICM1} (26 K and 23 K) and in the centre of the phase at 30 K. No effect was observed on the scattered intensity, position or correlation except at 26 K, where a dramatic two-fold increase in the scattered intensity was evident in an applied electric field, shown in figure 5.16. We also note that the structural Bragg reflections showed no change at any temperature in applied electric field. The effect observed is therefore solely related to the magneto-striction modulation of the structure. The increase in intensity suggests an increase in the modulation in the direction of the respective Fourier component, which in this case lies in the *c*-axis direction. This would occur due to an increase in the *c*-axis component of the magnetic structure. Indeed, it was shown that in $TbMn_2O_5$ the magnetic diffraction intensity (**q**) was directly proportional to the magneto-striction diffraction intensity (2**q**) [147]. However, in this measurement it is not possible to assign this increase in moment to any given magnetic sub-lattice (Mn^{3+}, Mn^{4+}, or Tm). It is interesting to note that this effect only occurs after having ZFC the sample and then applied the field. It might be expected that by cooling the sample in a ± 16 kV cm^{-1} applied electric field, the system would again display an enhance magneto-striction at 26 K. The FC temperature dependences showed no such increase in intensity. Furthermore, the diffraction

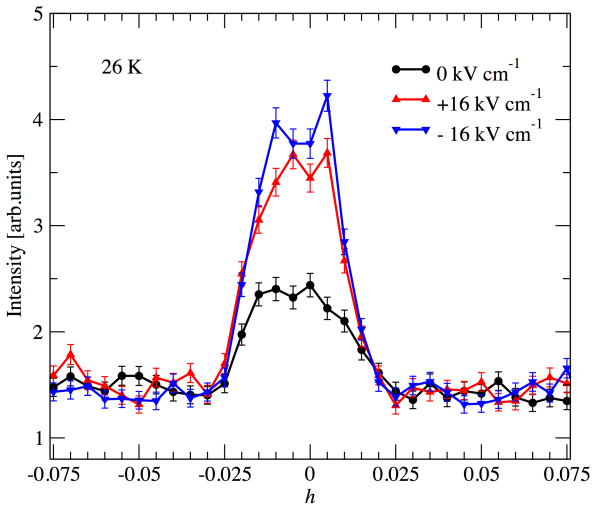

Figure 5.16: Static electric field dependence of the 2**q** reflection at 26 K. A two-fold increase in scattered intensity is observed in ± 16 kV cm^{-1}.

signal enhancement was only apparent within the 3 K region of the temperature dependence where, contrary to the literature, the electric polarisation was found to be zero; evidence that this region of the CM phase is of significance in understanding the electro-magnetic coupling of $TmMn_2O_5$.

As discussed in section 5.1 in the context of YMn_2O_5, domains are likely to play a key role in the $R Mn_2O_5$ series. We propose that the unexpected extinction of the electric polarisation at 28 K, 3 K above T_{ICM1}, could be due to the onset of a 50/50 occupation of domains with opposite electric polarisation, as proposed for YMn_2O_5 [121] and $TbMn_2O_5$ [38]. In this scenario the CM magnetic order, and hence magneto-striction, would remain despite the 50/50 domain occupation. However the *c*-axis magnetic moment component (S_z) could be reduced, and only recovered under an applied electric field as shown by the results in figure 5.16.

5.5 Conclusions

Our results confirm the onset of an electric polarisation at $T_{\mathrm{D}} = 36.4$ K, the ICM/CM, WFE3 phase transition. The electric polarisation then increases into the CM phase down to 30 K with the same temperature dependence as the magneto-striction; evidence that in the CM phase the exchange-striction model is significant. At 28 K the electric polarisation reduces to zero, 3 K higher than T_{ICM1}; the transition at which the polarisation extinction was expected. We tentatively assign this to the evolution of a 50/50 occupation of inversion related domains where the two domains have opposing electric polarisations, hence reducing the polarisation to zero whilst maintaining the CM magnetic order. In this 3 K region we measured a strong coupling between an applied static electric field and the magneto-striction, further evidence of the importance of the exchange-striction model of magneto-electric coupling in this phase of $TmMn_2O_5$.

Chapter 6

$TbMn_2O_5$ under high magnetic fields

6.1 Introduction

In this final experimental chapter we investigate the magneto-electric phenomena exhibited by $TbMn_2O_5$ at low temperatures. As described in section 3.2, a variety of magneto-electric effects have been observed in different members of the *R*Mn_2O_5 series. In general, a change in the ferroelectricity was observed in response to an applied magnetic field, probably mediated through a change in the magnetic structure or domain occupation. In $HoMn_2O_5$ a magnetic field applied parallel to the *b*-axis in the incommensurate (ICM) phase reinstated the electric polarisation evident in the commensurate (CM) phase [118, 133]. The opposite effect was observed in $ErMn_2O_5$ whereby an applied magnetic field suppressed the electric polarisation [118, 123]. In $TmMn_2O_5$ a magnetic field applied parallel to the *c*-axis induced a polarisation flop from the *a*-axis to the *b*-axis in the low temperature LT-ICM phase [137], and in $TbMn_2O_5$, a 2 T magnetic field applied parallel to the *a*-axis, also in the LT-ICM phase, resulted in a highly reproducible electric polarisation flip, parallel to the *b*-axis, shown in figure 3.10(a) [135].

It is likely that the dominant origin of the magneto-electric effects in the LT-ICM

phase of the RMn$_2$O$_5$ series is the behaviour of the rare-earth ion sub-lattice, despite the polarisation originating in the manganese magnetic structure. As such, the rare-earth ions are expected to provide a '*magnetic handle*' on the system. Their large response to the applied magnetic field may cause changes in the symmetry of the system and modifications in the manganese magnetic structure, possibly through an f-d interaction. With such a diverse range of phenomena across the series, the small differences in an otherwise common manganese magnetic structure are unlikely to result in the varied responses to applied magnetic fields. Indeed, in YMn_2O_5 the manganese magnetic structure was found to be invariant in magnetic fields up to 8 T [117], whilst magnetometry measurements of a number of RMn$_2$O$_5$ compounds showed the magnetic susceptibility to be dominated by the rare-earth magnetism [135, 144, 179]. Further evidence of the importance of the rare-earth ion behaviour is that the extreme magneto-electric effects are only evident at low temperatures, often below the spontaneous ordering temperature of the rare-earth sub-lattice. Also, the magneto-electric effects tend to occur when the magnetic field is applied parallel to the rare-earth easy axis of magnetisation. We refer the reader to the introductory sections of Chapter 3 for a comprehensive discussion of the RMn$_2$O$_5$ series.

From a technological standpoint, the repeatable polarisation switching evident in $TbMn_2O_5$ is arguably the most useful magneto-electric effect that the RMn$_2$O$_5$ series displays. A detailed understanding of the behaviour of the terbium sub-lattice under applied magnetic fields in the LT-ICM phase is therefore essential. Magnetometry indicated that at 2 T and 2 K, the terbium sub-lattice saturates with an average moment of 8.2 μ_B/Tb [135], close to the theoretical paramagnetic moment of 9.73 μ_B/Tb. Furthermore, neutron powder diffraction data suggested that the terbium sub-lattice is ferromagnetic above 2.5 T [38]. However, a detailed study of the behaviour of the terbium magnetic structure under applied magnetic fields has yet to be reported.

We have performed a resonant x-ray diffraction experiment with direct sensitivity to the terbium $5d$ and $4f$ electronic states, as in Chapter 3. The diffraction measurement was undertaken with an *in-situ* magnetic field of up to 10 T. This enabled us to detect changes in the terbium magnetic structure in response to the applied field. We investigated the 2 T polarisation reversal with the magnetic field applied parallel to the easy *a*-axis. The diffraction experiment was then repeated with the magnetic field applied parallel to the hard *c*-axis, in order to investigate any coupling to the small magnetic moment component expected in this direction.

6.2 Experiment

The experimental set up was identical to that described in Chapter 3, employing the six-circle, horizontal scattering diffractometer at beam line ID20 [153] at the European Synchrotron Radiation Facility. The diffractometer incorporates an Oxford Instruments 10 T superconducting split-coil cryomagnet sample environment, with a stable base sample temperature of 2 K, achieved by a helium flux cryostat. The instrument is shown in figure 3.16.

Two high quality single crystals of $TbMn_2O_5$ with dimensions approximately 1 x 1 x 0.2 mm and 2 x 2 x 0.5 mm were grown at the Department of Chemistry in the National Taiwan University by flux growth. The crystals had (0, 0, 1) and (4, 4, 0) Bragg reflections surface normal to their large facets, respectively, which were polished to a mirror-like finish. In the diffraction measurements with H$\|a$, the first sample was used, mounted with the (0, 0, 1) reflection in the horizontal scattering plane, perpendicular to the magnetic field. Similarly, the second sample was used for H$\|c$ measurements with the (4, 4, 0) reflection in the scattering plane. Constraints in the experimental geometry restricted the study to a limited number of magnetic satellites of surface normal Bragg reflections. The incident x-ray beam polarisation was unrotated, and was therefore polarised in the π channel for the

horizontal scattering geometry. A measurement of specific polarisation channels of the scattered light was performed through the use of an Au(222) polarisation analyser crystal at the terbium L_{III} edge.

6.3 Results and Discussion

6.3.1 Magnetic field $\parallel$ *a*-axis

In order to characterise the $TbMn_2O_5$ samples and check their response to applied magnetic fields at low temperatures, the isothermal magnetisation was measured using a Quantum Design MPMS [86]. Figure 6.1 shows the data collected on one of the samples, measured with the magnetic field applied parallel to the *a*-axis. In agreement with the literature [135] the magnetisation saturates at approximately 2 T, dominated by the rare-earth moments of 8.2 μ_{B}/Tb.

The sample with the (0, 0, 1) Bragg reflection surface normal was mounted within the 10 T cryomagnet such that the *c*-axis and *a*-axis were parallel and perpendicular to the scattering plane, respectively. The external magnetic field was then parallel to the *a*-axis. The sample was cooled to 4 K, well within the LT-ICM phase in which the polarisation reversal was reported. Magnetic satellites of the (0, 0, 4), (0, 0, 5) and (0, 0, 6) Bragg reflections were surveyed in both π' and σ' scattered polarisation channels. All magnetic reflections were found to be extremely weak, however the most intense were evident around the (0, 0, 5) reflection. For practicality, the following experiment was therefore constrained to the study of the (0+δ, 0, 5-τ) and (0+δ, 0, 5+τ) magnetic satellites, with $\delta \simeq 0.487$ and $\tau \simeq 0.316$. The other two (0, 0, 5) satellites could not be accessed.

Scans of scattered intensity as a function of incident x-ray energy through the terbium L_{III}-edge were performed on both reflections in the $\pi - \pi'$ and $\pi - \sigma'$ x-ray polarisation channels. The scans were then repeated in an applied field of 2.5 T,

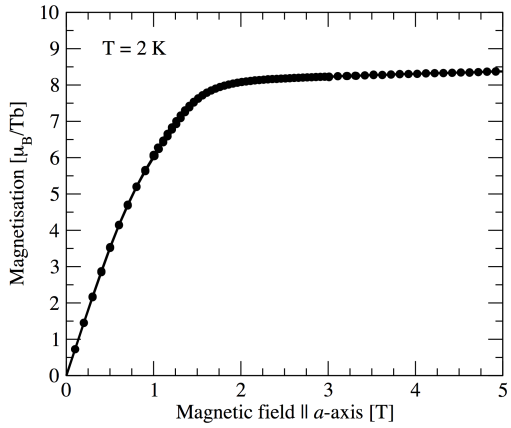

Figure 6.1: The isothermal magnetisation of $TbMn_2O_5$ measured at 2 K.

above the electric polarisation reversal transition. The data, corrected for fluctuations in the incident beam intensity, are presented in figure 6.2. In zero magnetic field, the E1-E1 resonance at 7.52 keV was clearly observed in all scans. In addition, the E2-E2 resonance, observed in $TbMn_2O_5$ in Chapter 3, was evident at 7.512 keV in both polarisation channels at the (0+δ, 0, 5+τ) reflection. In figure 6.2, the 2.5 T energy spectra have been scaled such that the E1-E1 resonance coincides with that of the zero applied field spectra. This allows for a clear comparison of the relative behaviour of the E2-E2 resonance. The E1-E1 resonance originates in the terbium $2p \rightarrow 5d$ electronic transition. In Chapter 3 we showed that, as the $5d$ states are delocalised, this resonance is primarily sensitive to the manganese magnetic structure and hence remains prominent throughout the application of an external magnetic field.

The important result of this study is the dramatic extinction and suppression of the E2-E2 resonance of the (0+δ, 0, 5+τ) reflection in the $\pi - \pi'$ and $\pi - \sigma'$ channels shown in figures 6.2(b) and 6.2(d), respectively, occurring at 2 T. We also note that there was a reduction in the scattered intensity at the E2-E2 energy at the (0+δ, 0, 5-τ) reflection, measured in the $\pi - \pi'$ channel, shown in figure 6.2(a). However,

the statistical errors are large making this result less clear. The E2-E2 resonance originates in the terbium $2p \rightarrow 4f$ transition, and as such the resonance is directly sensitive to the $4f$ magnetism. The changes in the relative intensity of the E2-E2 resonance induced by the applied magnetic field may occur for two reasons. Either the terbium magnetic structure could dramatically rearrange in response to the applied magnetic field, hence changing the atomic scattering factors, or the terbium incommensurate propagation vector could change with respect to that of the manganese. Later in this chapter, figure 6.3 presents the magnetic field dependence of the (0+δ, 0, 5+τ) reflection, measured at both E1-E1 and E2-E2 energies and in both polarisation channels. The data showed that both the E1-E1 and E2-E2 resonances have a common magnetic propagation vector. The changes observed in the E2-E2 resonance must therefore occur due to a rearrangement of the terbium sub-lattice magnetic structure.

Neutron diffraction data suggests that the terbium ions order ferromagnetically at 2.5 T [38]. This would explain the extinction of the E2-E2 resonance measured in the $\pi - \pi'$ channel, as for a ferromagnetic structure the magnetic unit cell coincides with the crystallographic unit cell giving zero intensity at all satellite positions. However, the resonance was only partially suppressed in the $\pi - \sigma'$ energy spectra. This indicates that the terbium magnetic structure maintains some degree of antiferromagnetic propagation, in common with the manganese magnetism. We suggest, therefore, that the terbium sub-lattice adopts a canted antiferromagnetic structure with a large ferromagnetic component in the *a*-axis direction. This scenario also explains the reduced terbium magnetic moment upon saturation, without invoking crystal electric field effects (discussed in Chapter 2). Structure factor calculations could provide clues about the actual magnetic structure, however many more reflections must be measured, which were not accessible in our experiment.

Figures 6.3(a) and 6.3(b) show the magnetic field dependence of both E1-E1 and

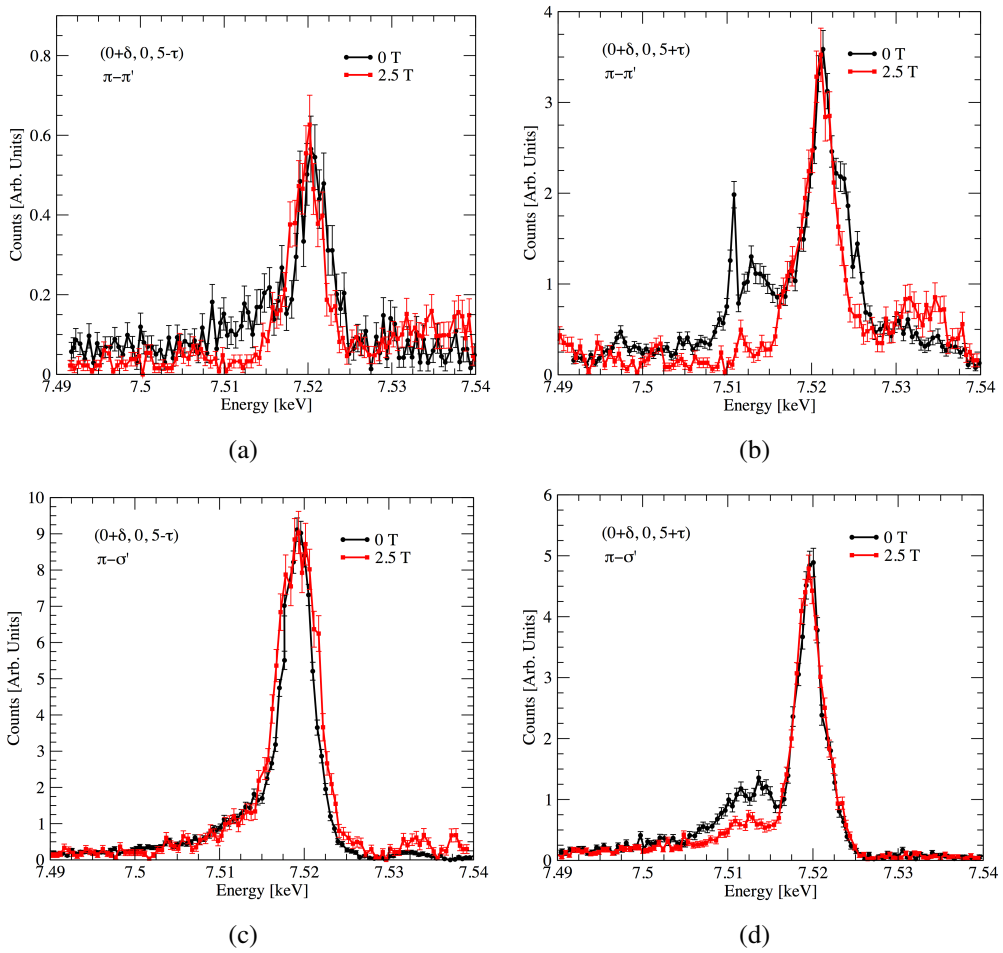

Figure 6.2: Scans of the scattered intensity as a function of incident x-ray energy through the Tb L_{III} edge of (a) & (c), the (0+δ, 0, 5-τ) and (b) & (d), the (0+δ, 0, 5+τ) reflections, measured in the $\pi - \pi'$ and $\pi - \sigma'$ polarisation channels, respectively. The scans were performed at 4 K, in zero applied magnetic field (black circles) and 2.5 T (red triangles). Note that the intensity units, albeit arbitrary, are scaled equivalently with respect to each other such that a relative comparison between the zero applied field spectra can be made. The 2.5 T spectra are scaled such that the E1-E1 resonance coincides with that of the zero applied field spectra allowing for a clear comparison of the E2-E2 resonance behaviour.

E2-E2, (0+δ, 0, 5+τ) energy resonances, measured in the $\pi - \pi'$ and $\pi - \sigma'$ polarisation channels, respectively. The magnetic field dependence of the (0+δ, 0, 5-τ) E1-E1 resonance is then shown in figure 6.4, also measured in both polarisation channels. The top three panes of figures 6.3(a), 6.3(b), 6.4(a), and 6.4(b) show that the magnetic propagation vector was approximately invariant in the *h* and *k* directions, with only a small monotonic decrease in the *h*-direction. By comparison a dramatic increase in the *l* component of the propagation vector occurred between 0 and 2.5 T, accurately mirrored in the $+\tau$ and $-\tau$ reflections. Above 2.5 T the propagation vector remained approximately constant up to 10 T. This suggests that the magnetic propagation along the *c*-axis is closely coupled to the magneto-electric polarisation flip. Furthermore, as both E1-E1 and E2-E2 dependences followed the same trend, one would predict a significant coupling between the two sub-lattices. This is contrary to the behaviour indicated through neutron diffraction measurements [38], however synchrotron x-ray diffraction provides far greater reciprocal space resolution and ionic and electronic band sensitivity, and so reveals such subtle effects. This result therefore provides new evidence of the terbium ions coupling to the manganese magnetic structure under applied magnetic fields.

Also included in figures 6.3(a), 6.3(b), 6.4(a), and 6.4(b) are the magnetic field dependencies of the correlation length and integrated intensity. The correlation length of all reflections was found to be invariant within the range 1000 to 1500 Å under applied magnetic field. The integrated intensity of the E1-E1 resonance decreased between 0 and 2.5 T, above which it remained approximately constant up to 10 T, following a similar trend to the magnetic propagation along the *c*-axis. The E2-E2 integrated intensity reflects the trend described in the above discussion of the energy spectra.

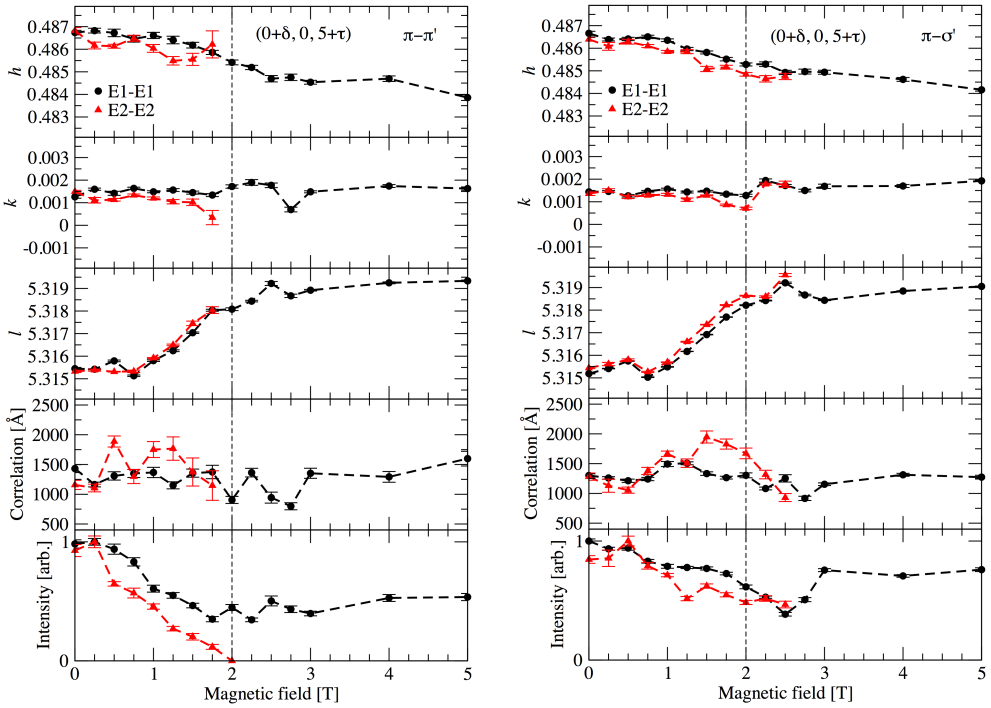

(a) (b)

Figure 6.3: The magnetic field dependence of the (0+δ, 0, 5+τ) wave vector, correlation length and integrated intensity, measured in (a) the $\pi - \pi'$ and (b) the $\pi - \sigma'$ polarisation channels. The E1-E1 and E2-E2 resonance dependencies are shown in black circles and red triangles, respectively. The 2 T polarisation flip transition is indicated by the vertical dashed line.

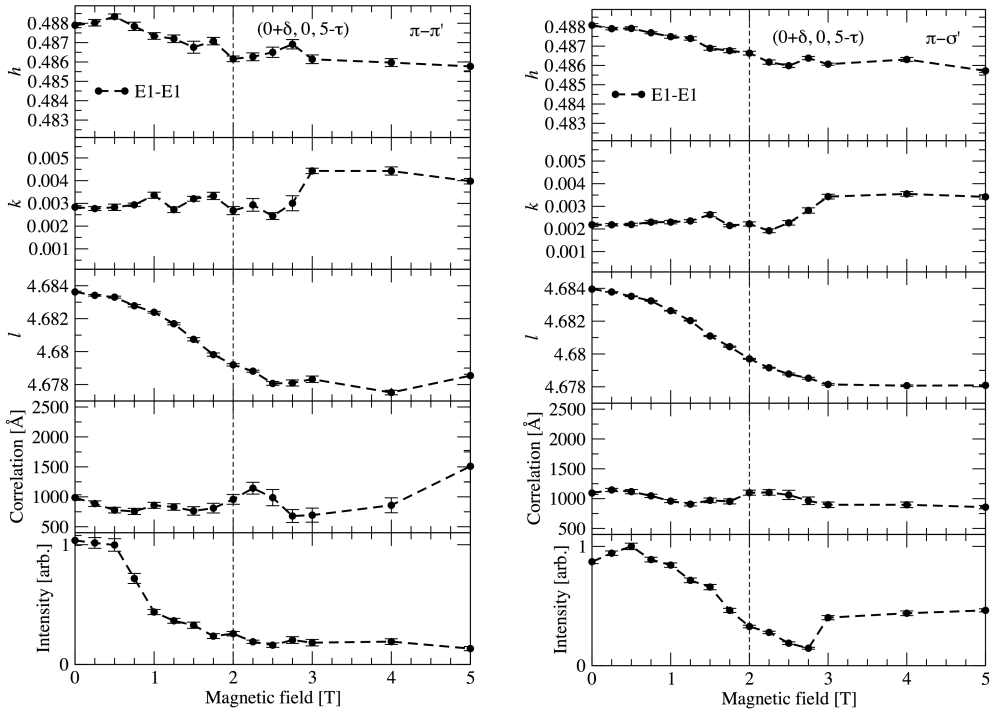

(a) (b)

Figure 6.4: The magnetic field dependence of the (0+δ, 0, 5-τ) wave vector, correlation length and integrated intensity, measured in (a) the $\pi - \pi'$ and (b) the $\pi - \sigma'$ polarisation channels. Only the E1-E1 resonance was observed, shown in black circles. The 2 T polarisation flip transition is indicated by the vertical dashed line.

6.3.2 Magnetic field $\parallel$ *c*-axis

The experiment was repeated on the second sample, with the (4, 4, 0) Bragg reflection in the scattering plane and the magnetic field parallel to the *c*-axis. The sample was cooled to 5 K and incommensurate magnetic satellites of the (4, 3, 0), (4, 4, 0), and (5, 2, 0) Bragg reflections were located. As is often the case in synchrotron experiments, time constraints forced us to study only the satellites of the (4, 4, 0) reflection. These magnetic diffraction signals were studied in detail in zero magnetic field, reported in Chapter 3. In this experiment we applied a 10 T magnetic field parallel to the *c*-axis and remeasured the magnetic satellite reflections. Figure 6.5 shows reciprocal space maps containing a surprising result. Under a 10 T applied magnetic field, additional incommensurate reflections exist with a slightly larger *h* component of the propagation vector. We label the normal and additional reflections $\mathbf{q}_{\mathrm{ICM}}$ and $\mathbf{q}_{\mathrm{ICM\_B}}$, respectively. The additional $\mathbf{q}_{\mathrm{ICM\_B}}$ reflections are believed to be of magnetic origin, as they exist in the rotated polarisation channel, close to the known magnetic propagation vector, and with a similar energy dependence to magnetic reflections measured with zero applied magnetic field. The energy spectra are shown and discussed later in this section. We also note that no change was observed in the structural Bragg reflections upon applying the magnetic field, showing that $\mathbf{q}_{\mathrm{ICM\_B}}$ was not of structural origin.

The data presented in figure 6.5 were measured under consistent external conditions. There were no $\mathbf{q}_{\mathrm{ICM\_B}}$ satellites evident at the (4+δ, 4, 0+τ) and (4-δ, 4, 0-τ) positions in this measurement, however they had been observed in other data sets. Furthermore, $\mathbf{q}_{\mathrm{ICM\_B}}$ satellites were also observed at (4+δ, 3, 0-τ), (4+δ, 3, 0+τ), and (5+δ, 2, 0-τ) positions, also induced by a 10 T magnetic field. The two $\mathbf{q}_{\mathrm{ICM}}$ and $\mathbf{q}_{\mathrm{ICM\_B}}$ reflections are clearly separated in the *h* direction. However, we note that the magnitude of the separation is almost within the peak width in the low resolution *l* direction, and so we cannot be certain that there isn't also an additional

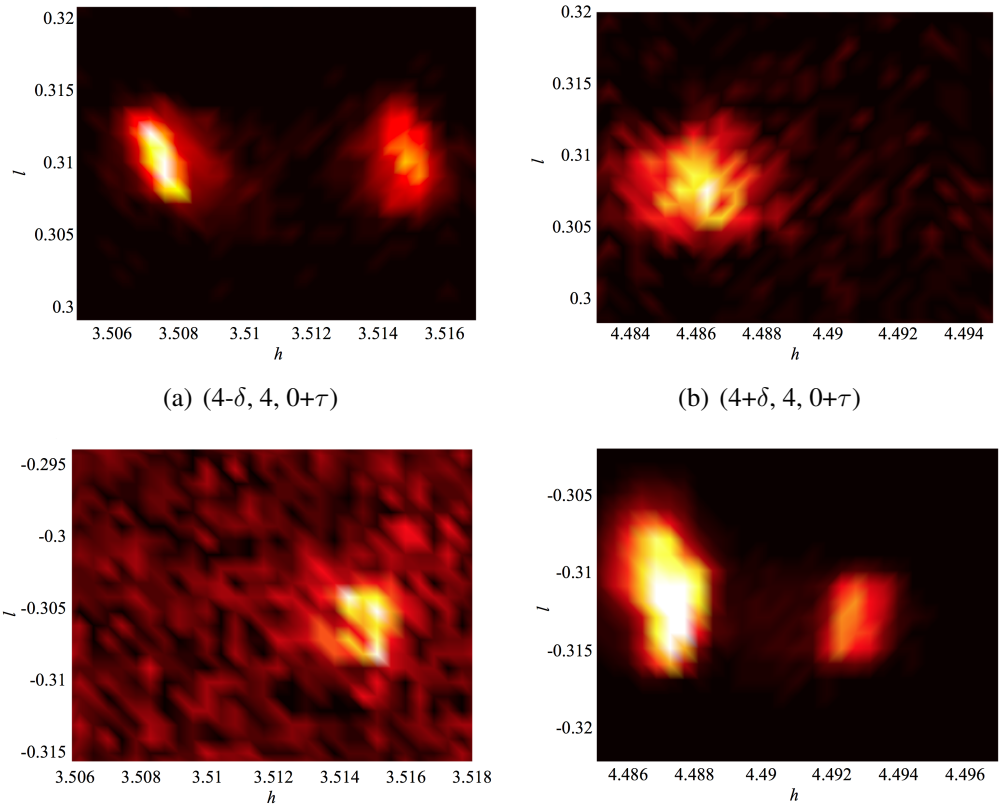

(a) (4-δ, 4, 0+τ) (b) (4+δ, 4, 0+τ)

(c) (4-δ, 4, 0-τ) (d) (4+δ, 4, 0-τ)

Figure 6.5: Reciprocal space maps of the (4, 4, 0) Bragg reflection incommensurate magnetic satellites, measured under a 10 T magnetic field applied parallel to the *c*-axis at 5 K. Panes (a) and (c) show the additional $\mathbf{q}_{\mathrm{ICM\_B}}$ reflections, induced by the magnetic field. The intensity scale was arbitrarily chosen to display the satellites.

reflection, separated in *l*.

We then investigated the behaviour of the $\mathbf{q}_{\mathrm{ICM}}$ and $\mathbf{q}_{\mathrm{ICM\_B}}$ reflections under varied temperature and magnetic field in order to understand how they fit into the phase diagram of $TbMn_2O_5$. The magnetic field dependence was repeatedly measured, showing inconsistency in the magnetic field magnitude required to induce $\mathbf{q}_{\mathrm{ICM\_B}}$, which varied from 6 to 8 T. This would suggest that the evolution of the $\mathbf{q}_{\mathrm{ICM\_B}}$ reflection is to some extent metastable, however, the magnetic reflections

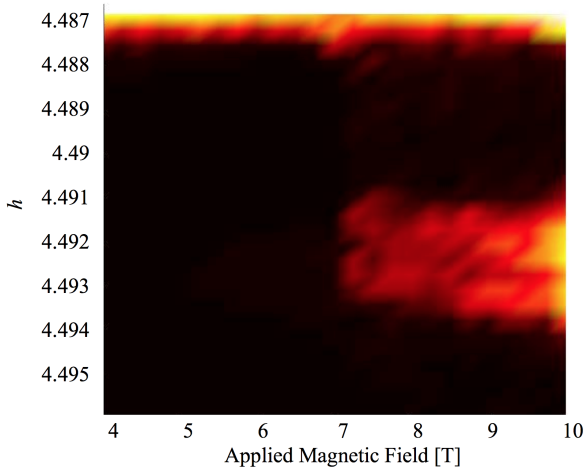

Figure 6.6: Magnetic field dependence of the $\mathbf{q}_{\mathrm{ICM\_B}}$ reflection, shown here to evolve in fields greater than 7 T at h = 4.493. The edge of the $\mathbf{q}_{\mathrm{ICM}}$ reflection is evident at the top of the figure. The intensity scale is arbitrary.

are extremely weak, and so are prone to being obscured by background x-ray intensity. Figure 6.6 shows a typical magnetic field dependence of the $\mathbf{q}_{\mathrm{ICM\_B}}$ reflection. The edge of $\mathbf{q}_{\mathrm{ICM}}$ is evident at the top of the figure.

Figure 6.7 shows the temperature dependence of the $\mathbf{q}_{\mathrm{ICM}}$ and $\mathbf{q}_{\mathrm{ICM\_B}}$ reflections in an applied magnetic field of 10 T. The inset shows the peak profiles in the h direction. Throughout the figure the $\mathbf{q}_{\mathrm{ICM}}$ and $\mathbf{q}_{\mathrm{ICM\_B}}$ data are coloured blue and red, respectively. In figure 6.7(a), the data show the evolution of $\mathbf{q}_{\mathrm{ICM\_B}}$ on cooling below 7 K whilst the $\mathbf{q}_{\mathrm{ICM}}$ scattered intensity remains constant. On a number of measurements the exact transition temperature was found to be unrepeatable. We explain this through the same reasoning described above in the case of the magnetic field induced transition. It is interesting to note that the transition occurs in the temperature region in which the terbium ions spontaneously order, indicating that the behaviour of the rare-earth ions could be key to the evolution of $\mathbf{q}_{\mathrm{ICM\_B}}$. Figure 6.7(b) shows that the correlation lengths of the magnetic orders probed by $\mathbf{q}_{\mathrm{ICM}}$ and $\mathbf{q}_{\mathrm{ICM\_B}}$ are equal and invariant throughout the measured temperature range.

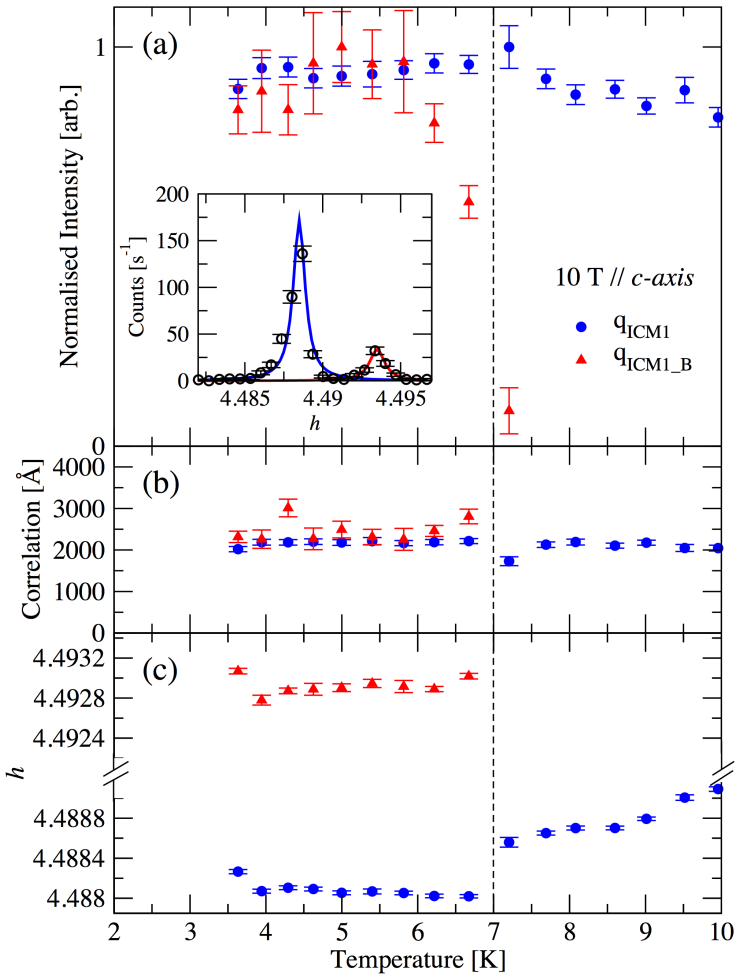

Figure 6.7: The temperature dependence at an applied magnetic field of 10 T of (a) the normalised integrated intensity, (b) the correlation length, and (c) the h position, of the $\mathbf{q}_{\mathrm{ICM}}$ (blue) and $\mathbf{q}_{\mathrm{ICM\_B}}$ (red) reflections. The inset shows the two reflections measured in the h direction.

Figure 6.7(c) shows the position in *h* of $\mathbf{q}_{\mathrm{ICM}}$ and $\mathbf{q}_{\mathrm{ICM\_B}}$ as a function of temperature. There is a pronounced step in the position of $\mathbf{q}_{\mathrm{ICM}}$ that occurs concomitantly with the development of the $\mathbf{q}_{\mathrm{ICM\_B}}$ reflection. This is a significant result, indicating that the two reflections are closely coupled. Figure 6.8 shows this step in detail, measured at both the (4+δ, 4, 0-τ) and (4-δ, 4, 0+τ) reflections. The step was repeatable, and mirrored in opposite δ. We note that the step occurs 1 K higher in this measurement, showing the uncertainty in the transition temperature. Assuming that the step in the $\mathbf{q}_{\mathrm{ICM}}$ position is a direct consequence of the existence of $\mathbf{q}_{\mathrm{ICM\_B}}$, the unrepeatable nature of the transition is more likely due to metastability, as opposed to difficulties in observing the weak $\mathbf{q}_{\mathrm{ICM\_B}}$ reflection above background.

Scans of the scattered intensity as a function of incident x-ray energy through the terbium L_{III} edge were measured at the (4-δ, 4, 0+τ) and (4+δ, 4, 0-τ), $\mathbf{q}_{\mathrm{ICM}}$ and $\mathbf{q}_{\mathrm{ICM\_B}}$ reflections, shown in figure 6.9. Again, both E1-E1 and E2-E2 excitation channels were evident, as was the case in our previous studies of $TbMn_2O_5$. The reciprocal space maps presented in figure 6.5 were measured with an incident x-ray energy corresponding to the E2-E2 excitation, probing the terbium $4f$ states. The relative intensity of the E2-E2 excitations correspond well with the relative $\mathbf{q}_{\mathrm{ICM}}$ and $\mathbf{q}_{\mathrm{ICM\_B}}$ diffraction intensities evident in the maps. Through a survey of a greater number of magnetic satellites not presented here, it was apparent that the energy spectra line shape of a set of satellites is invariant for opposite τ, but is different for opposite δ. This analysis yields an important result. The line shape of the $\mathbf{q}_{\mathrm{ICM\_B}}$ reflection is similar to that of the $\mathbf{q}_{\mathrm{ICM}}$ reflection opposite in δ, as shown in figure 6.9. This could suggest a symmetry relation between the two, discussed later in this section. We note that the energy spectra of all measured reflections are invariant upon applied magnetic field.

All the above measurements were made having systematically zero field cooled (ZFC) the sample from the paramagnetic phase above $T_{\mathrm{N}} = 43$ K. Finally, we inves-

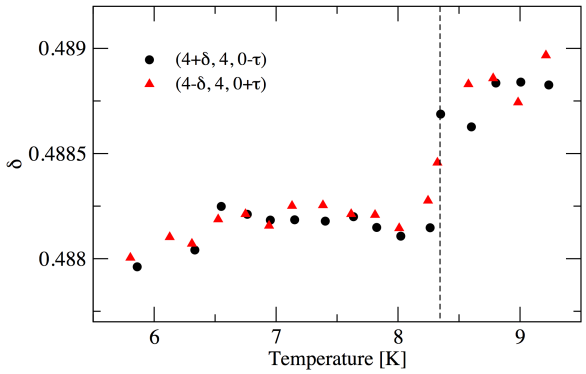

Figure 6.8: The step in position of the $\mathbf{q}_{\mathrm{ICM}}$ reflection in the h direction occuring concomitantly with the evolution of $\mathbf{q}_{\mathrm{ICM\_B}}$. Data measured at both (4+δ, 4, 0-τ) and (4-δ, 4, 0+τ) reflections are shown, coloured black and red, respectively.

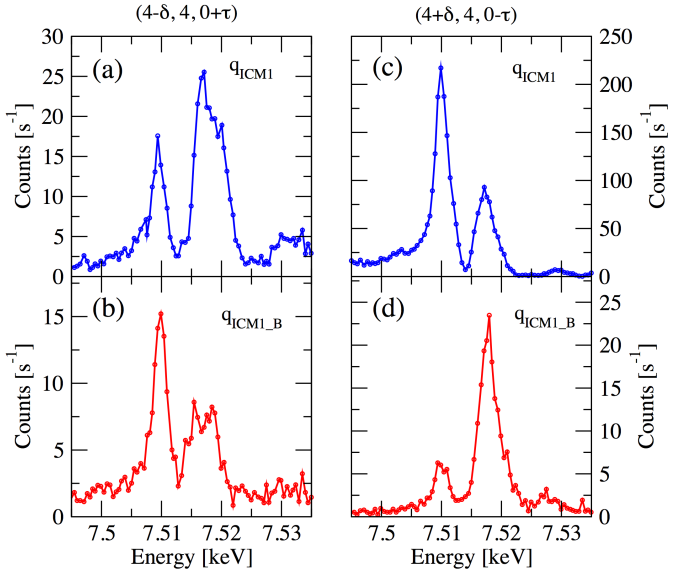

Figure 6.9: Scans of the scattered intensity measured as a function of incident x-ray energy through the Tb L_{III} edge at constant wave vector at the (a) & (b) (4-δ, 4, 0+τ) and (c) & (d) (4+δ, 4, 0-τ), $\mathbf{q}_{\mathrm{ICM}}$ (blue) and $\mathbf{q}_{\mathrm{ICM\_B}}$ (red) reflections.

tigated the effect of field cooling (FC) the sample in 10 T from the CM, ICM2 and PM phases (see the phase diagram of $TbMn_2O_5$ shown in figure 3.12). Both $\mathbf{q}_{\mathrm{ICM}}$ and $\mathbf{q}_{\mathrm{ICM\_B}}$ were found to be invariant upon FC from both CM and ICM2 phases, however upon FC from the paramagnetic (PM) phase the intensity of the $\mathbf{q}_{\mathrm{ICM\_B}}$ reflection was suppressed. Figure 6.10 shows both $\mathbf{q}_{\mathrm{ICM}}$ and $\mathbf{q}_{\mathrm{ICM\_B}}$ measured at (a) the (4-δ, 4, 0+τ) and (b) (4+δ, 4, 0-τ) positions, having ZFC (black) and FC (red) from the PM phase. The (4-δ, 4, 0+τ), $\mathbf{q}_{\mathrm{ICM\_B}}$ satellite was reduced to $\sim 30\%$ of the ZFC intensity, and the (4-δ, 4, 0+τ), $\mathbf{q}_{\mathrm{ICM\_B}}$ satellite was suppressed below the background. We also note a significant shift to higher *h* in the peak positions, comparable to that shown in figure 6.8.

We now discuss the possible origin of the $\mathbf{q}_{\mathrm{ICM\_B}}$ magnetic reflection. The magnetic field applied parallel to the *a*-axis causes a substantial rearrangement of the terbium sub-lattice magnetic structure that we have shown to be weakly coupled to the manganese magnetism. This magnetic rearrangement was evident in the isothermal magnetisation measurements and the relative behaviour of the E1-E1 and E2-E2 resonances at the terbium L_{III} edge. We have shown that the energy spectra line shapes are invariant when the magnetic field is applied parallel to the *c*-axis. Also, there was no evidence in isothermal *c*-axis magnetisation measurements up to 8 T of a substantial change in the terbium magnetic structure (figure 6.11). In comparison to the *a*-axis magnetometry shown in figure 6.1, the *c*-axis is clearly the hard axis of magnetisation, as expected [135]. This suggests that the evolution of $\mathbf{q}_{\mathrm{ICM\_B}}$ is due to small changes in the magnetic structure. These changes could then result in either the coexistence of two magnetic orders with slightly different propagation vectors, or the removal of the inversion symmetry relation that once made different magnetic domains indistinguishable by diffraction.

We tentatively suggest that our results are indicative of the latter case. We return to the possible magnetic domains described in section 3.2.3, where there preferen-

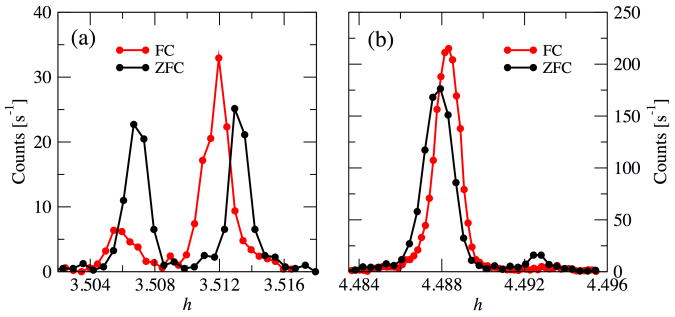

Figure 6.10: Scans in the h reciprocal space direction showing both $\mathbf{q}_{\mathrm{ICM}}$ and $\mathbf{q}_{\mathrm{ICM\_B}}$ reflections measured at (a) the (4-δ, 4, 0+τ) and (b) (4+δ, 4, 0-τ) positions, having zero field cooled (ZFC) (black) and field cooled (FC) (red) from the paramagnetic phase.

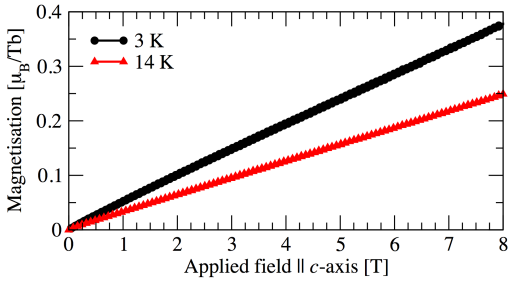

Figure 6.11: The magnetisation of $TbMn_2O_5$ measured with the field applied parallel to the c-axis at 3 K (black) and 14 K (red), below and above the spontaneous ordering temperature of the terbium sub-lattice.

tially exists two domains with magnetic structure combinations I+III and II+IV, respectively. Structures I & II describe the *ab*-plane, and III & IV, the *bc*-plane. Both pairs are related by inversion symmetry, hence imposing the same inversion relation between domains I+III and II+IV. We anticipate that the magnetic field applied parallel to the *c*-axis removes the inversion relation between magnetic structures III and IV due to a differing response of the *c*-axis magnetic moment components. The difference in the *c*-axis magnetism between the two domains is associated with the two antiferromagnetic zig-zag chains running parallel to the *a*-axis, as describe in section 3.2.3. Furthermore, the de-phasing of these zig-zag chains is believed to be closely related to the discommensuration. We anticipate, therefore, that in response to the *c*-axis magnetic field the two domains become distinguishable by diffraction, with the associated wave vectors being slightly different due to shifts in the de-phasing of the zig-zag chains. In this scenario the *ab*-plane structures I and II may remain the inverse of each other, as indicated by the comparison of the $\mathbf{q}_{\mathrm{ICM}}$ and $\mathbf{q}_{\mathrm{ICM\_B}}$ energy spectra.

Finally, we extend this argument to describe the field cooling (FC) behaviour. Key to the evolution of the $\mathbf{q}_{\mathrm{ICM\_B}}$ reflection is the formation of the two magnetic domains that may occur, with varying respective occupation, below T_{N}. Once the domains are formed, the *c*-axis FC does not then modify the domain occupation. However, it may be possible that FC through T_{N} promotes the formation of a single domain, hence reducing the possible occupation of the two domains that give rise to the two reflections, $\mathbf{q}_{\mathrm{ICM}}$ and $\mathbf{q}_{\mathrm{ICM\_B}}$.

6.4 Conclusions

Upon applying an external magnetic field parallel to the *a*-axis of $TbMn_2O_5$ in the LT-ICM phase, we observed a significant change in the relative intensities of the E1-E1 and E2-E2 resonances. The two directly probe the terbium $5d$ and $4f$ electronic

states, respectively. The E2-E2 resonance was shown to become suppressed at 2 T, coinciding with the electric polarisation reversal. It has been reported that at 2 T the terbium sub-lattice magnetic structure saturates with a ferromagnetic ordering. Our data show that a degree of antiferromagnetic propagation, common with the manganese magnetic structure, remains. As such, the terbium sub-lattice adopts a canted antiferromagnetic structure with a large ferromagnetic component along the *a*-axis. This scenario explains the reduced saturation magnetic moment of the terbium ions, evident in magnetisation measurements. Furthermore, due to the extremely high reciprocal space resolution of synchrotron x-ray diffraction, we were able to show a weak coupling between the manganese and terbium sub-lattices, which are thought to be completely decoupled.

With an external magnetic field applied parallel to the *c*-axis we have made the discovery of additional incommensurate magnetic reflections, close in reciprocal space to those evident in zero applied magnetic field. The two reflections, labelled $\mathbf{q}_{\mathrm{ICM}}$ and $\mathbf{q}_{\mathrm{ICM\_B}}$, share a common *l* component of the propagation vector, and are slightly separated in the *h* direction. We show that the evolution of $\mathbf{q}_{\mathrm{ICM\_B}}$ is closely coupled to the $\mathbf{q}_{\mathrm{ICM}}$ reflection, and occurs above applied magnetic fields of 6 to 8 T, below 7 to 8 K. The behaviour of the additional $\mathbf{q}_{\mathrm{ICM\_B}}$ reflection has been well characterised, and we suggest that the two reflections originate in different magnetic domains. These domains are related by inversion symmetry in zero applied field, and so are indistinguishable by diffraction. At higher fields, the inversion symmetry between the *c*-axis magnetic structures is broken, changing the de-phasing of the *a*-axis zig-zag chains, resulting in two diffraction peaks at slightly different positions in *h*.

Chapter 7

Conclusions

7.1 Summary

In this thesis we have studied a number of crystalline materials that exhibit fascinating physical phenomena due to the behaviour of rare-earth ions. A microscopic understanding of these materials has the potential to further our fundamental knowledge of solid-state physics, and pave the way for great advances in technology. The following conclusions summarise the findings of our experiments that were based upon diffraction techniques; some of the most lucid methods for investigating electronic order within crystalline materials.

We began by investigating the R_2CoGa_8 series of intermetallics, specifically the Er_2CoGa_8 and Tm_2CoGa_8 members. This newly synthesised series exhibits a variety of bulk magnetic and transport properties dependent upon the choice of rare-earth ion. Previous to this study, very little was known regarding the magnetic structures of these compounds, however, due to the relatively simple crystallographic topology, the magnetic structures were also thought likely to be simple. Furthermore, only one ion species, the rare-earth ions, are magnetic. These two compounds therefore provided an excellent starting point in our study of crystalline

rare-earth compounds. For both materials, we have solved the magnetic structures through the refinement of neutron powder diffraction data. Despite having common easy axes of magnetisation (in the *ab*-plane) the magnetic propagation vectors were found to be different due to a competition between crystal electric field effects and the RKKY exchange interaction. We showed that the magnetic order parameter adopts either the 3D-Ising or 3D-XY universality class, with transition temperatures of 3.0 K and 2.0 K, for the erbium and thulium compounds, respectively. Further, by comparison of the R_2CoGa_8 and RGa_3 magnetic structures we suggest that the $CoGa_2$ layers play an important role in the 3D magnetism in this series, as opposed to inducing a quasi-2D magnetic structure that is evident, for example, in iso-structural superconductors.

Following our study of rare-earth intermetallic systems we turned to investigate rare-earth manganese oxide multiferroics, in particular $TbMn_2O_5$ and $TmMn_2O_5$. These systems exhibit two of the most extreme magneto-electric effects observed in a single phase, solid-state compound. In $TbMn_2O_5$ an applied magnetic field flips the electric polarisation, and in $TmMn_2O_5$, an electric polarisation flop occurs on cooling through the rare-earth spontaneous magnetic ordering temperature. The polarisation flop can then be reversed by applying a magnetic field. A comprehensive understanding of this phenomena would have an immediate impact on the development of future technology. The exact microscopic mechanism behind the magnetically induced electric polarisation and the magneto-electric coupling that results in the macroscopic phenomena remains the subject of intense debate. Two models are currently outstanding candidates, they are the symmetric exchange-striction model, and the antisymmetric inverse Dzyaloshinsky-Moriya, spin-orbit model. Following the belief that the rare-earth ions play an important role in the magneto-electric properties of these materials, we have performed resonant x-ray diffraction (RXD) experiments to make an element and electronic state specific measurement, pro-

viding us with information specifically about the terbium sub-lattice that neutron diffraction or bulk magnetometry or transport property measurements cannot.

Two energy resonances were observed at magnetic satellite reflections, one just above the terbium L_{III} edge while the other at 8 eV lower, in both the low-temperature incommensurate (ICM1) and commensurate (CM) phases of $TbMn_2O_5$. The higher energy resonance originates from the E1-E1 dipolar transition, which probes the terbium $5d$ band, and the lower energy resonance originates from the E2-E2 quadrupolar transition, which probes the terbium $4f$ band. The temperature dependence and wave vector measurements confirmed the reflections to be of magnetic origin. Full linear polarisation analysis showed that the $5d$ band of the terbium ions is spin polarised predominantly by the Mn^{4+} spin density in the CM phase, with an additional interaction with the terbium $4f$ magnetic structure. Tuning to the E2-E2 excitation at 2 K (LT-ICM) and fitting to the full linear polarisation analysis data enabled the refinement of directions of the ordered terbium $4f$ electron spins. The measurement and refinement were repeated in the CM phase at 25 K. We therefore solved the terbium sub-lattice magnetic structures in these two phases of $TbMn_2O_5$ through RXD.

We then studied the possible magneto-electric mechanisms at play in the CM phase in both $TbMn_2O_5$ and $TmMn_2O_5$. In $TbMn_2O_5$ we investigated the existence of a magnetic resonance measured at the oxygen *K* absorption edge. Our study was based upon *ab-initio* calculations performed using the FDMNES code, through which we were able to comment on the magnetic hybridisation between the manganese and oxygen ions; an effect that is key to the exchange-striction model. By simulating the oxygen *K*-edge resonance, we have shown that the magnetism on the oxygen sites giving rise to the resonance is due to antiferromagnetic spin polarisation, specifically through interaction with the Mn^{3+} ions. Further analysis of the oxygen DOS suggests that the O3 oxygen ions located at the apex of the square-

based pyramids give a dominant contribution to the resonant diffraction intensity. This supports the argument that the electronic hybridisation between these two ion species gives rise to a substantial electric polarisation. The dependence of the resonant intensity on the displacement of the Mn^{3+} ion along the axis of the surrounding square-based pyramid was investigated. We showed that the resonance is insensitive to the ferroelectric displacements predicted to be of the order 10^{-3} Å, and so conversely, any such displacement will not affect the antiferromagnetic oxygen spin polarisation. Our calculations strongly indicated that the exchange-striction model not only exists, but is likely to play a significant role in the magnetically induced ferroelectricity present in the commensurate phase of $TbMn_2O_5$.

A more direct measurement of the magneto-electric coupling in the commensurate phase of $TmMn_2O_5$ was reported in Chapter 5. *In-situ* electric polarisation measurements were performed simultaneously with x-ray diffraction measurements of reflections that originate in the structural modulations due to magneto-striction. As such, the simultaneous measurement monitors the behaviour of the exchange-striction mechanism. Through determining the temperature dependences of the two order parameters (magneto-striction and ferroelectric), we provided strong evidence that in the CM phase the exchange-striction model is dominant. In a 3 K region above T_{ICM1} in which we measured zero net electric polarisation, we discovered a strong interaction between an applied static electric field and the magneto-striction, *i.e.*, the reverse coupling.

The work presented in Chapters 4 and 5 clearly show that the exchange-striction model is predominantly responsible for the magnetically induced ferroelectricity in the commensurate phase. Finally, we investigated the behaviour of the rare-earth magnetism in the LT-ICM phase of $TbMn_2O_5$, in which the extreme magneto-electric phenomena have been observed. The E2-E2 resonance, directly probing the terbium $4f$ electronic states, was shown to become suppressed under a 2 T applied

magnetic field applied parallel to the *a*-axis, coinciding with the electric polarisation reversal. A reported analysis of neutron diffraction data indicated that the terbium moments ferromagnetically order at this magnetic field. However, our measurement, which was directly sensitive to the electronic states in question, showed that a degree of antiferromagnetic propagation exists in common with the manganese sub-lattice magnetic structure. The terbium sub-lattice therefore adopts a canted antiferromagnetic structure with a large ferromagnetic component along the *a*-axis, elegantly explaining the reduced saturation magnetic moment evident in the magnetometry data. We also showed that there is a weak coupling between the manganese and terbium sub-lattices, which were previously thought to be completely decoupled. This result was only evident due to the extremely high reciprocal space resolution inherent to synchrotron diffraction experiments and the use of resonant diffraction techniques that are both ionic and electronic state specific.

With an external magnetic field > 7 T applied parallel to the *c*-axis we have made the discovery of additional incommensurate magnetic reflections in $TbMn_2O_5$. The additional reflections, labelled $\mathbf{q}_{\mathrm{ICM\_B}}$, shared a common *l* component and a slightly higher *h* component of the propagation vector, compared to the expected incommensurate reflections, labelled $\mathbf{q}_{\mathrm{ICM}}$. The behaviour of the additional reflections has been well characterised, and we suggest that $\mathbf{q}_{\mathrm{ICM}}$ and $\mathbf{q}_{\mathrm{ICM\_B}}$ originate in two different magnetic domains. In this scenario, we surmise that at high magnetic fields, the inversion symmetry between the two respective *c*-axis magnetic structures is broken. This makes the scattering from the two distinguishable by diffraction, and possibly changes the de-phasing of the *a*-axis zig-zag chains; resulting in two diffraction peaks at slightly different positions in *h*.

7.2 Future work

The continuation of the work presented within this thesis and it's impact in solid-state research splits in two parts; the development of physical ideas and the advancement of experimental techniques. The study of the R_2CoGa_8 intermetallics has resulted in the first conclusively determined magnetic structures of the series to be reported in the literature. This will pave the way for investigating the structures of the other R_2CoGa_8 compounds, and similar intermetallic systems. Indeed, as a direct result of this study, we are now embarking on a synchrotron resonant x-ray diffraction study of Er_2CoGa_8 and Tm_2CoGa_8, to investigate the intricacies of the RKKY and crystal electric field competition in intermetallics. In the RMn_2O_5 series of multiferroics, the significance of the exchange-striction model in the commensurate phase has been made clear. However, the exact mechanism behind the low temperature magneto-electric phenomena remains the subject of debate. In particular, we have made the first observation of diffraction signals that arise in response to a magnetic field applied parallel to the *c*-axis. These signals are directly sensitive to the behaviour of the rare-earth ions, an understanding of which is believed to be of great importance in finally identifying the mechanisms at play. This, therefore, must be investigated further, as a theoretical prediction of the addition diffraction signals could provide a substantial leap in our physical interpretation of these complex rare-earth oxides.

Finally, we have developed the technique of full linear polarisation analysis for the determination of ion, and electronic state specific magnetic structures. Also, we have provided a comprehensive theoretical investigation of magnetic diffraction signals measured at the oxygen *K*-edge. We believe that both these techniques will be exploited in the future, and prove to be essential in novel diffraction studies that unravel the most complex crystalline magnetic materials.

Bibliography

[1] J. B. Goodenough. *Phys. Rev.*, 100:564, 1955.

[2] J. Kanamori. *J. Phys. Chem. Solids*, 10:87, 1959.

[3] C. Ederer and N. Spaldin. *Nature Materials*, 3:849, 2004.

[4] N. A. Spaldin and M. Fiebig. *Science*, 309:391, 2005.

[5] R. Ramesh. *Nature*, 461:1218, 2009.

[6] R. Kajimoto, T. Kakeshita, H. Yoshizawa, T. Tanabe, T. Katsufuji, and Y. Tokura. *Phys. Rev. B*, 64:144432, 2001.

[7] S-H. Lee and S-W. Cheong. *Phys. Rev. Lett.*, 79:2514, 1997.

[8] Y. Murakami, H. Kawada, H. Kawata, M. Tanaka, T. Arima, Y. Moritomo, and Y. Tokura. *Phys. Rev. Lett.*, 80:1932, 1998.

[9] S. B. Wilkins, P. D. Spencer, P. D. Hatton, S. P. Collins, M. D. Roper, D. Prabhakaran, and A. T. Boothroyd. *Phys. Rev. Lett.*, 91:167205, 2003.

[10] S. B. Wilkins, N. Stojic, T. A. W. Beale, N. Binggeli, C. W. M. Castleton, P. Bencok, D. Prabhakaran, A. T. Boothroyd, P. D. Hatton, and M. Altarelli. *Phys. Rev. B*, 71:245102, 2005.

[11] C. Kittel. *Introduction to Solid State Physics*. Wiley, 1996.

[12] E. O. Wollan and W. C. Koehler. *Phys. Rev.*, 100:545, 1955.

[13] E. Dagotto and T. M. Rice. *Science*, 271:618, 1996.

[14] V. Kiryukhin, Y. J. Kim, K. J. Thomas, F. C. Chou, R. W. Erwin, Q. Huang, M. A. Kastner, and R. J. Birgeneau. *Phys. Rev. B*, 63:144418, 2001.

[15] N. Aliouane, O. Prokhnenko, R. Feyerherm, M. Mostovoy, J. Strempfer, K. Habicht, K. C. Rule, E. Dudzik, A. U. B. Wolter, A. Maljuk, and D. N. Argyriou. *J. Phys.: Condens. Matter*, 20:434215, 2008.

[16] S. Rössler, S. Harikrishman, U. K. Pössler, S. Elizabeth, H. L. Bhat, F. Steglich, and S. Wirth. *J. Phys.: Conf. Series*, 200:012168, 2010.

[17] K. N. R. Taylor and M. I. Darby. *Physics of Rare Earth Solids*. Chapman and Hall, 1972.

[18] W. C. Koehler, J. W. Cable, M. K. Wilkinson, and E. O. Wollan. *Phys. Rev.*, 151:414, 1966.

[19] D. Gibbs, D. R. Harshman, E. D. Isaacs, D. B. McWhan, D. Mills, and C. Vettier. *Phys. Rev. Lett.*, 61:1241, 1966.

[20] D. A. Joshi, R. Nagalakshmi, S. K. Dhar, and A. Thamizhavel. *Phys. Rev. B*, 77:174420, 2008.

[21] D. A. Joshi, A. K. Nigam, S. K. Dhar, and A. Thamizhavel. *Phys. Rev. B*, 80:054414, 2009.

[22] M. T. Hutchings. *Solid State Physics: Advances in Research and Applications*, 16:227, 1964.

[23] M. Tachibana, K. Akiyama, H. Kawaji, and T. Atake. *Phys. Rev. B*, 72:224425, 2005.

[24] J. Rodríguez-Carvajal. *Physica B*, 192:55, 1993.

[25] Y. Joly. *Phys. Rev. B*, 63:125120, 2001.

[26] A. J. Freeman and R. E. Watson. *Phys. Rev.*, 124:1439, 1961.

[27] P. W. Anderson. *Phys. Rev.*, 79:350, 1950.

[28] C. Zener. *Phys. Rev.*, 82:403, 1951.

[29] P. W. Anderson and H. Hasegawa. *Phys. Rev.*, 100:675, 1955.

[30] M. A. Ruderman and C. Kittel. *Phys. Rev.*, 96:99, 1954.

[31] T. Kasuya. *Prog. Theor. Phys.*, 16:45, 1956.

[32] K. Yosida. *Phys. Rev.*, 106:893, 1957.

[33] I. E. Dzyaloshinskii. *J. Phys. Chem. Solids*, 4:241, 1958.

[34] T. Moriya. *Phys. Rev.*, 120:91, 1960.

[35] I. E. Dzyaloshinskii. *Sov. Phys. JETP*, 19:960, 1964.

[36] D. Jiles. *Introduction to Magnetism and Magnetic Materials*. Chapman and Hall/CRC, 1998.

[37] S. Blundell. *Magnetism in Condensed Matter*. Oxford University Press, 2001.

[38] L. C. Chapon, G. R. Blake, M. J. Gutmann, S. Park, N. Hur, P. G. Radaelli, and S-W. Cheong. *Phys. Rev. Lett.*, 93:177402, 2004.

[39] I. A. Sergienko and E. Dagotto. *Phys. Rev. B*, 73:094434, 2006.

[40] S-W. Cheong and M. Mostovoy. *Nature Materials*, 6:13, 2007.

[41] N. W. Ashcroft and N. D. Mermin. *Solid State Physics*. Saunders College, 1976.

[42] S. W. Lovesey. *Theory of neutron scattering from condensed matter*, volume 1. Clarendon Press, 1984.

[43] G. L. Squires. *Introduction to the Theory of Thermal Neutron Scattering*. Cambridge University Press, 1978.

[44] S. W. Lovesey. *Theory of neutron scattering from condensed matter*, volume 2. Clarendon Press, 1984.

[45] P. A. Egelstaff, editor. *Thermal Neutron Scattering*. Academic Press, 1965.

[46] J. Als-Nielsen and D. McMorrow. *Elements of Modern X-ray Physics*. Wiley, 2001.

[47] W. H. Zachariasen. *Theory of X-ray Diffraction in Crystals*. Dover, 1945.

[48] J. P. Hannon, G. T. Trammell, M. Blume, and D. Gibbs. *Phys. Rev. Lett.*, 61:1245, 1988.

[49] J. P. Hill and D. F. McMorrow. *Acta Cryst.*, 52:236, 1996.

[50] M. Blume and D. Gibbs. *Phys. Rev. B*, 37:1779, 1988.

[51] M. Altarelli. *Magnetism: a synchrotron radiation approach*. Springer, 2006.

[52] M. Blume. *J. Appl. Phys.*, 57:3615, 1985.

[53] J. Voigt, J. Persson, J. W. Kim, G. Bihlmayer, and T. Bruckel. *Phys. Rev. B*, 76:104431, 2007.

[54] W. R. Busing and H. A. Levy. *Acta Cryst.*, 22:457, 1967.

[55] M. Lohmeier and E. Vlieg. *J. Appl. Cryst.*, 26:706, 1993.

[56] E. Hecht. *Optics*. Addison-Wesley, 2002.

[57] M. Bass, J. M. Enoch, E. W. Van Stryland, and W. L. Wolfe, editors. *Handbook of Optics*, volume 3. McGraw-Hill, 2001.

[58] C. Giles, C. Vettier, F. de Bergevin, C. Malgrange, G. Griibel, and F. Grossi. *Rev. Sci. Instrum.*, 88:1518, 1995.

[59] L. Bouchenoire, S. D. Brown, P. Thompson, J. A. Duffy, J. W. Taylor, and M. J. Cooper. *J. Sync. Rad.*, 10:172, 2003.

[60] C. Mazzoli, S. B. Wilkins, S. DiMatteo, B. Detlefs, C. Detlefs, V. Scagnoli, L. Paolasini, and P. Ghigna. *Phys. Rev. B*, 76:195118, 2007.

[61] H. M. Rietveld. *J. Appl. Cryst.*, 2:65, 1969.

[62] R. A. Young, editor. *The Rietveld Method*. Oxford University Press, 1993.

[63] S. Di Matteo, T. Chatterji, Y. Joly, A. Stunault, J. A. Paixao, R. Suryanarayanan, G. Dhalenne, and A. Revcolevschi. *Phys. Rev. B*, 68:024414, 2003.

[64] Y. Joly, S. Grenier, and J. E. Lorenzo. *Phys. Rev. B*, 68:104412, 2003.

[65] E. Nazarenko, J. E. Lorenzo, Y. Joly, J. L. Hodeau, D. Mannix, and C. Marin. *Phys. Rev. Lett.*, 97:056403, 2006.

[66] S. R. Bland, B. Detlefs, S. B. Wilkins, T. A. W. Beale, C. Mazzoli, Y. Joly, P. D. Hatton, J. E. Lorenzo, and V. A. M. Brabers. *J. Phys.: Condens. Matter*, 21:485601, 2009.

[67] F. Steglich, J. Aarts, C. D. Bredl, W. Lieke, D. Meschede, W. Franz, and H. Schafer. *Phys. Rev. Lett.*, 43:1892, 1979.

[68] D. A. Brawner and H. R. Ott. *Phys. Rev. B*, 50:6530, 1994.

[69] W. Bao, P. G. Pagliuso, J. L. Sarrao, J. D. Thompson, Z. Fisk, and J. W. Lynn. *Phys. Rev. B*, 64:020401(R), 2001.

[70] M. Nicklas, V. A. Sidorov, H. A. Borges, P. G. Pagliuso, C. Petrovic, Z. Fisk, J. L. Sarrao, and J. D. Thompson. *Phys. Rev. B*, 67:020506(R), 2003.

[71] D. A. Joshi, C. V. Tomy, and S. K. Malik. *J. Phys.: Condens. Matter*, 19:136216, 2007.

[72] P. Gegenwart, Q. Si, and F. Steglich. *Nature Physics*, 4:186, 2008.

[73] N. Kimura, Y. Muro, and H. Aoki. *J. Phys. Soc. Jpn.*, 76:051010, 2007.

[74] I. Sugitani, Y. Okuda, H. Shishido, T. Yamada, A. Thamizhavel, E. Yamamoto, T. D. Matsuda, Y. Haga, T. Takeuchi, R. Settai, and Y. Onuki. *J. Phys. Soc. Jpn.*, 75:043703, 2006.

[75] P. G. Pagliuso, D. J. Garcia, E. Miranda, E. Granado, R. Lora Serrano, C. Giles, J. G. S. Duque, R. R. Urbano, C. Rettori, J. D. Thompson, M. F. Hundley, and J. L. Sarrao. *J. Appl. Phys.*, 99:08P703, 2006.

[76] R. Settai, T. Takeuchi, and Y. Onuki. *J. Phys. Soc. Jpn.*, 76:051003, 2007.

[77] C. Adriano, L. Mendonca-Ferreira, E. M. Bittar, and P. G. Pagliuso. *J. Appl. Phys.*, 103:07B712, 2008.

[78] P. Morin, M. Giraud, P. L. Regnault, E. Roudaut, and A. Czopnik. *J. Mag. Mag. Mat.*, 66:345, 1987.

[79] C. Adriano, C. Giles, L. N. Coelho, and P. G. Pagliuso. *Physica B*, 404:3289, 2009.

[80] W. E. Wallace. *Rare Earth Intermetallics*. Academic Press, 1973.

[81] A. Szytula and J. Leciejewicz. *Handbook of Crystal Structures and Magnetic Properties of Rare Earth Intermetallics*. CRC Press, 1994.

[82] K. W. Stevens. *Proc. Phys. Soc., London, Sect. A*, 65:209, 1952.

[83] G. van der Laan and B. T. Thole. *Phys. Rev. B*, 53:53, 1996.

[84] J. Jensen and A. R. Mackintosh. *Rare Earth Magnetim Structures and Excitations*. Calrendon, Oxford, 1991.

[85] Z. Fisk and J. P. Remeika. *Handbook on the Physics and Chemistry of Rare Earths*, volume 12. Elsevier, 1989.

[86] http://www.qdusa.com/products/mpms.html. October 2010.

[87] B. D. Josephson. *Phys. Lett.*, 1:251, 1962.

[88] B. B. Schwartz and S. Foner. *Superconducting Applications: SQUIDs and Machines*. Plenum Press, New York, 1977.

[89] http://www.isis.stfc.ac.uk/instruments/wish/. October 2010.

[90] http://www.isis.stfc.ac.uk/index.html. October 2010.

[91] A. Le Bail. *Powder Diffraction*, 20:316, 2005.

[92] V. L. Ginzburg and L. D. Landau. *Zh. Eksp. Teor. Fiz.*, 20:1064, 1950.

[93] M. F. Collins. *Magnetic Critical Scattering*. Oxford University Press, 1989.

[94] R. B. Griffiths. *Phys. Rev. Lett.*, 24:1479, 1970.

[95] R. B. Griffiths and J. C. Wheeler. *Phys. Rev. A*, 20:1047, 1970.

[96] http://www.mcphase.de. October 2010.

[97] Ch. D. Routsi, J. K. Yakinthos, and E. Gamari-Seale. *J. Mag. Mag. Mat.*, 116:397, 1992.

[98] E. A. Goremychkin, R. Osborn, B. D. Rainford, R. T. Macaluso, D. T. Adroja, and M. Koza. *Nature Physics*, 4:766, 2008.

[99] M. Fiebig. *J. Phys. D: Appl. Phys.*, 38:R123, 2005.

[100] J. van den Brink and D. I. Khomskii. *J. Phys.: Condens. Matter*, 20:434217, 2008.

[101] L. W. Martin, S. P. Crane, Y-H Chu, M. B. Holcomb, M. Gajek, M. Huijben, C-H. Yang, N. Balke, and R. Ramesh. *J. Phys.: Condens. Matter*, 20:434220, 2008.

[102] D. I. Khomskii. *Physics*, 2:20, 2009.

[103] N. A. Hill. *Annu. Rev. Mater. Res.*, 32:1, 2002.

[104] B. B. van Aken, T. T. M. Palstra, A. Filippetti, and N. A. Spaldin. *Nature Materials*, 3:164, 2004.

[105] A. Daoud-Aladine, J. Rodríguez-Carvajal, L. Pinsard-Gaudart, M. T. Fernández-Díaz, and A. Revcolevschi. *Phys. Rev. Lett.*, 89:097205, 2002.

[106] T. Kimura, T. Goto, H. Shintani, K. Ishizaka, T. Arima, and Y. Tokura. *Nature*, 426:55, 2003.

[107] G. Lawes, A. B. Harris, T. Kimura, N. Rogado, R. J. Cava, A. Aharony, O. Entin-Wohlman, T. Yildirim, M. Kenzelmann, C. Broholm, and A. P. Ramirez. *Phys. Rev. Lett.*, 95:087205, 2005.

[108] K. Taniguchi, N. Abe, T. Takenobu, Y. Iwasa, and T. Arima. *Phys. Rev. Lett.*, 97:097203, 2006.

[109] H. Schmid. *Ferroelectrics*, 162:317, 1994.

[110] H. Schmid. *J. Phys.: Condens. Matter*, 20:434201, 2008.

[111] A. B. Harris, A. Aharony, and O. Entin-Wohlman. *J. Phys.: Condens. Matter*, 20:434202, 2008.

[112] M. Mostovoy. *Phys. Rev. Lett.*, 96:067601, 2006.

[113] M. Kenzelmann, A. B. Harris, S. Jonas, C. Broholm, J. Schefer, S. B. Kim, C. L. Zhang, S-W. Cheong, O. P. Vajk, and J. W. Lynn. *Phys. Rev. Lett.*, 95:087206, 2005.

[114] S. Dong, R. Yu, S. Yunoki, J-M. Liu, and E. Dagotto. *Phys. Rev. B*, 78:155121, 2008.

[115] M. Mochizuki and N. Furukawa. *Phys. Rev. B*, 80:134416, 2009.

[116] M. Mochizuki, N. Furukawa, and N. Nagaosa. *Phys. Rev. Lett.*, 105:037205, 2010.

[117] P. G. Radaelli and L. C. Chapon. *J. Phys.: Condens. Matter*, 20:434213, 2008.

[118] Y. Noda, H. Kimura, M. Fukunaga, S. Kobayashi, I. Kagomiya, and K. Kohn. *J. Phys.: Condens. Matter*, 20:434206, 2008.

[119] L. C. Chapon, P. G. Radaelli, G. R. Blake, S. Park, and S-W. Cheong. *Phys. Rev. Lett.*, 96:097601, 2006.

[120] J-H. Kim, S-H. Lee, S. I. Park, M. Kenzelmann, A. B. Harris, J. Schefer, J-H. Chung, C. F. Majkrzak, M. Takeda, S. Wakimoto, S. Y. Park, S-W. Cheong, M. Matsuda, H. Kimura, Y. Noda, and K. Kakurai. *Phys. Rev. B*, 78:245115, 2008.

[121] P. G. Radaelli, L. C. Chapon, A. Daoud-Aladine, C. Vecchini, P. J. Brown, T. Chatterji, S. Park, and S-W. Cheong. *Phys. Rev. Lett.*, 101:067205, 2008.

[122] A. B. Sushkov, M. Mostovoy, R. Valdes Aguilar, S-W. Cheong, and H. D. Drew. *J. Phys.: Condens. Matter*, 20:434210, 2008.

[123] H. Kimura, S. Kobayashi, Y. Fukuda, T. Osawa, Y. Kamada, Y. Noda, I Kagomiya, and K. Kohn. *J. Phys. Soc. Jpn.*, 76:074706, 2007.

[124] Y. Noda, H. Kimura, Y. Kamada, T. Osawa, Y. Fukuda, Y. Ishikawa, S. Kobayashi, Y. Wakabayashi, H. Sawa, N. Ikeda, and K. Kohn. *Physica B*, 385:119, 2006.

[125] K. Cao, G-C. Guo, D. Vanderbilt, and L. He. *Phys. Rev. Lett.*, 103:257201, 2009.

[126] R. D. Johnson, S. R. Bland, C. Mazzoli, T. A. W. Beale, C-H. Du, C. Detlefs, S. B. Wilkins, and P. D. Hatton. *Phys. Rev. B*, 78:104407, 2008.

[127] G. Beutier, A. Bombardi, C. Vecchini, P. G. Radaelli, S. Park, S.-W. Cheong, and L. C. Chapon. *Phys. Rev. B*, 77:172408, 2008.

[128] R. A. Ewings, A. T. Boothroyd, D. F. McMorrow, D. Mannix, H. C. Walker, and B. M. Wanklyn. *Phys. Rev. B*, 77:104415, 2008.

[129] A. Munoz, J. A. Alonso, M. T. Casais, M. J. Martínez-Lope, J. L. Martínez, and M. T. Fernández-Díaz. *Phys. Rev. B*, 65:144423, 2002.

[130] C. Vecchini, L. C. Chapon, P. J. Brown, T. Chatterji, S. Park, S-W. Cheong, and P. G. Radaelli. *Phys. Rev. B*, 77:134434, 2008.

[131] R. P. Chaudhury, C. R. dela Cruz, B. Lorenz, Y. Sun, C-W. Chu, S. Park, and S-W. Cheong. *Phys. Rev. B*, 77:220104(R), 2008.

[132] S. Kobayashi, T. Osawa, H. Kimura, Y. Noda, I. Kagomiya, and K. Kohn. *J. Phys. Soc. Jpn.*, 73:1593, 2004.

[133] H. Kimura, Y. Kamada, Y. Noda, K. Kaneko, N. Metoki, and K. Kohn. *J. Phys. Soc. Jpn.*, 75:113701, 2006.

[134] M. Fukunaga and Y. Noda. *J. Phys. Soc. Jpn.*, 79:054705, 2010.

[135] N. Hur, S. Park, P. A. Sharma, J. S. Ahn, S. Guha, and S-W. Cheong. *Nature*, 429:392, 2004.

[136] M. Fukunaga, K. Nishihata, H. Kimura, Y. Noda, and K. Kohn. *J. Phys. Soc. Jpn.*, 77:094711, 2008.

[137] M. Fukunaga, Y. Sakamoto, H. Kimura, Y. Noda, N. Abe, K. Taniguchi, T. Arima, S. Wakimoto, M. Takeda, K. Kakurai, and K. Kohn. *Phys. Rev. Lett.*, 103:077204, 2009.

[138] Y. F. Popov, A. M. Kadomtseva, S. S. Krotov, G. P. Vorob'ev, K. I. Kamilov, M. M. Lukina, and M. M. Tegranchi. *J. Exp. Theor. Phys.*, 96:961, 2003.

[139] G. R. Blake, L. C. Chapon, P. G. Radaelli, S. Park, N. Hur, S-W. Cheong, and J. Rodríguez-Carvajal. *Phys. Rev. B*, 71:214402, 2005.

[140] A. B. Sushkov, R. Valdes Aguilar, S. Park, S-W. Cheong, and H. D. Drew. *Phys. Rev. Lett.*, 98:027202, 2007.

[141] K. Saito and K. Kohn. *J. Phys.: Condens. Matter*, 7:2855, 1995.

[142] Th. Lottermoser, D. Meier, P. V. Pisarev, and M. Fiebig. *Phys. Rev. B*, 80:100101(R), 2009.

[143] J. Okamoto, D. J. Huang, C. Y. Mou, K. S. Chao, H. J. Lin, S. Park, S-W. Cheong, and C. T. Chen. *Phys. Rev. Lett.*, 98:157202, 2007.

[144] A Alonso, M T Casais, M J Martinez-Lope, J L Martinez, and M T Fernandez-Diaz. *J. Phys.: Condens. Matter*, 9:8515, 1997.

[145] S. Kobayashi, T. Osawa, H. Kimura, Y. Noda, N. Kasahara, S. Mitsuda, and K. Kohn. *J. Phys. Soc. Jpn.*, 73:3439, 2004.

[146] P. Toledano, W. Schranz, and G. Krexner. *Phys. Rev. B*, 79:144103, 2009.

[147] J. Koo, C. Song, S. Ji, J.-S. Lee, J. Park, T.-H. Jang, C.-H. Yang, J.-H. Park, Y. H. Jeong, K.-B. Lee, T. Y. Koo, Y. J. Park, J.-Y. Kim, D. Wermeille, A. I. Goldman, G. Srajer, S. Park, and S.-W. Cheong. *Phys. Rev. Lett.*, 99:197601, 2007.

[148] T. A. W. Beale, S. B. Wilkins, R. D. Johnson, S. R. Bland, Y. Joly, T. R. Forrest, D. F. McMorrow, F. Yakhou, D. Prabhakaran, A. T. Boothroyd, and P. D. Hatton. *Phys. Rev. Lett.*, 105:087203, 2010.

[149] J. Koo, S. JI, T-H. Jang, Y. H. Jeong, K-B. Lee, T. Y. Koo, S. A. Kim, and C-H Lee. *J. Kor. Phys. Soc.*, 51:562, 2007.

[150] C. Wang, G-C. Guo, and L. He. *Phys. Rev. Lett.*, 99:177202, 2007.

[151] C. Wang, G-C. Guo, and L. He. *Phys. Rev. B*, 77:134113, 2008.

[152] B. Detlefs, S. B. Wilkins, R. Caciuffo, J. A. Paixao, K. Kaneko, F. Honda, N. Metoki, N. Bernhoeft, J. Rebizant, and G. H. Lander. *Phys. Rev. B*, 77:024425, 2008.

[153] L. Paolasini, C. Detlefs, C. Mazzoli, S. B. Wilkins, P. P. Dean, A. Bombardi, N. Kernavanois, F. de Bergevin, F. Yakhou, J. P. Nalade, I. Breslavetz, A. Fondacaro, G. Pepellin, and P. Bernard. *J. Sync. Rad.*, 14:301, 2007.

[154] Lonny E. Berman, Qun Shen, Ken D. Finkelstein, Park Doing, Zhijian Yin, and Guoqiang Pan. *Rev. Sci. Instrum.*, 73:1502, 2002.

[155] F. Bartolomé, J. M. Tonnerre, L. Sève, D. Raoux, J. Chaboy, L. M. García, M. Krisch, and C. C. Kao. *Phys. Rev. Lett.*, 79:3775, 1997.

[156] C. Dallera, M. H. Krisch, A. Rogalev, C. Gauthier, J. Goulon, F. Sette, and A. Sole. *Phys. Rev. B*, 62:7093, 2000.

[157] H. Wende, Z. Li, A. Scherz, G. Ceballos, K. Baberschke, A. Ankudinov, J. J. Rehr, F. Wilhelm, A. Rogalev, D. L. Schlagel, and T. A. Lograsso. *J. Appl. Phys.*, 91:7361, 2002.

[158] C. Detlefs, A. H. M. Z. Islam, A. I. Goldman, C. Stassis, P. C. Canfield, J. P. Hill, and D. Gibbs. *Phys. Rev. B*, 55:R680, 1997.

[159] S. B. Wilkins. *Charge and spin correlations in transition metal oxides*. PhD thesis, University of Durham, 2002.

[160] H. C. Walker, K. A. McEwen, D. F. McMorrow, S. B. Wilkins, F. Wastin, E. Colineau, and D. Fort. *Phys. Rev. Lett.*, 97:137203, 2006.

[161] P. Abbamonte, L. Venema, A. Rusydi, G. A. Sawatzky, G. Logvenov, and I. Bozovic. *Science*, 297:581, 2002.

[162] P. Abbamonte, G. Blumberg, A. Rusydi, A. Gozar, P. G. Evans, T. Siegrist, L. Venema, H. Eisaki, E. D. Isaacs, and G. A. Sawatzky. *Nature*, 431:1078, 2004.

[163] D. J. Huang, H-J. Lin, J. Okamoto, K. S. Chao, H-T. Jeng, G. Y. Guo, C-H. Hsu, C-M. Huang, D. C. Ling, W. B. Wu, C. S. Yang, and C. T. Chen. *Phys. Rev. Lett.*, 96:096401, 2006.

[164] S. B. Wilkins, S. Di Matteo, T. A. W. Beale, Y. Joly, C. Mazzoli, P. D. Hatton, P. Bencok, F. Yakhou, and V. A. M. Brabers. *Phys. Rev. B*, 79:201102(R), 2009.

[165] M. García-Fernández, U. Staub, Y. Bodenthin, V. Scagnoli, V. Pomjakushin, S. W. Lovesey, A. Mirone, J. Herrero-Martín, C. Piamonteze, and E. Pomjakushina. *Phys. Rev. Lett.*, 103:097205, 2009.

[166] G. Giovannetti and J. van den Brink. *Phys. Rev. Lett.*, 100:227603, 2008.

[167] A. S. Moskvin and R. V. Pisarev. *Phys. Rev. B*, 77:060102(R), 2008.

[168] F. M. F. de Groot, M. Grioni, J. C. Fuggle, J. Ghijsen, G. A. Sawatzky, and H. Petersen. *Phys. Rev. B*, 40:5715, 1989.

[169] M. Cyrot and M. Lavagna. *Le Journal de Physique*, 40:763, 1979.

[170] S-Y. Yan, Y. Xie, T. Liu, and H-T. Yu. *J. Phys.: Condens. Matter*, 22:125501, 2010.

[171] K. Kimura, H. Nakamura, S. Kimura, M. Hagiwara, and T. Kimura. *Phys. Rev. Lett.*, 103:107201, 2009.

[172] B. G. Ueland, J. W. Lynn, M. Laver, Y. J. Choi, and S-W. Cheong. *Phys. Rev. Lett.*, 104:147204, 2010.

[173] Y. Yamasaki, H. Sagayama, T. Goto, M. Matsuura, K. Hirota, T. Arima, and Y. Tokura. *Phys. Rev. Lett.*, 98:147204, 2007.

[174] F. Fabrizi, H. C. Walker, L. Paolasini, F. de Bergevin, A. T. Boothroyd, D. Prabhakaran, and D. F. McMorrow. *Phys. Rev. Lett.*, 102:237205, 2009.

[175] C. Azimonte, E. Granado, H. Terashita, S. Park, and S-W. Cheong. *Phys. Rev. B*, 81:012103, 2010.

[176] D. Higashiyama, S. Miyasaka, N. Kida, T. Arima, and Y. Tokura. *Phys. Rev. B*, 70:174405, 2004.

[177] S. Kobayashi, H. Kimura, Y. Noda, and K. Kohn. *J. Phys. Soc. Jpn.*, 74:468, 2005.

[178] N. Iwata, M. Uga, and K. Kohn. *Ferroelectrics*, 204:97, 19097.

[179] M. Uga, N. Iwata, and K. Kohn. *Ferroelectrics*, 219:55, 1998.

[180] D. Higashiyama, S. Miyasaka, and Y. Tokura. *Phys. Rev. B*, 72:064421, 2005.

[181] B. M. Wanklyn. *J. Mater. Sci.*, 7:813, 1972.

[182] S. D. Brown, L. Bouchenoire, D. Bowyer, J. Kervin, D. Laundy, M. J. Longfield, D. Mannix, D. F. Paul, A. Stunault, P.Thompson, M. J. Cooper, C. A. Lucas, and W. G. Stirling. *J. Sync. Rad.*, 8:1172, 2001.

[183] S. D. Brown, P. Strange, L. Bouchenoire, B. Zarychta, P. B. J. Thompson, D. Mannix, S. J. Stockton, M. Horne, E. Arola, H. Ebert, Z. Szotek, W. M. Temmerman, and D. Fort. *Phys. Rev. Lett.*, 99:247401, 2007.